Model-based Optimization, Control and Assessment of Electric Aircraft Taxi Systems

Vom Fachbereich Maschinenbau
an der Technischen Universität Darmstadt
zur Erlangung des Grades eines Doktor-Ingenieurs (Dr.-Ing.)
genehmigte

DISSERTATION

vorgelegt von
Dipl.-Ing. Fabrizio Re
aus Genua

Berichterstatter	Prof. Dr.-Ing. Uwe Klingauf
Mitberichterstatter	Prof. Dr.-Ing. Stephan Rinderknecht

Tag der Einreichung	20.12.2016
Tag der mündlichen Prüfung	2.5.2017

Darmstadt 2017
D17

Typeset by the author using the LaTeX Documentation System.

Abstract

Aircraft ground operations are one important source of emissions in airports as taxi is conventionally performed by exploiting the inefficient idle thrust of the main jet engines. On-board Electric Taxi Systems (ETS) have been proposed featuring electric motors fitted in the landing gears in order to perform ground movements electrically while the main engines are off. While benefits can be expected on the ground due to the use of the Auxiliary Power Unit (APU) as power source which is more efficient in the required power range, the new system brings additional weight to the aircraft, resulting in a lower efficiency in flight and possibly even worsening the overall fuel consumption in a whole gate-to-gate mission. However, trade-offs and concrete figures regarding the expected benefits are difficult to identify in the state of the art because assessing methods for the taxi phase are often too coarse and based on too generic data and assumptions such as Thrust Specific Fuel Consumption tables, constant thrust settings and estimated taxi times.

This thesis contributes to the state of the art by presenting an integrated, model-based methodology to the assessment of aircraft systems at aircraft level in the conceptual design phase and its application to ETS. The proposed model-based process is shown to be necessary for answering key questions regarding the design of innovative aircraft subsystems in general, for performing solid comparisons and for determining suitable trade-offs while keeping the aircraft type and the specificities of the observed missions into account.

A substantial methodological contribution in the framework of the proposed approach is given by the automatic generation of energetically optimal ground path following profiles for electric taxiing based on convex optimization. Because an optimal path following profile exists for each given system architecture and variant, a sound performance comparison of different system variants is only possible if each of them can be operated according to its own optimal profile. Convex optimization permits to find a global optimum for each given problem in short computational time thanks to dedicated solving toolboxes. Convex formulations of path following problems studied in robotics and vehicle dynamics were adapted to the aircraft taxi problem. Moreover, convex formulations of relevant constraints in this problem, such as time constraints on passing predefined waypoints, were determined. The result of the convex optimization is used as input in the simulation of the mission ground phases with the integrated aircraft model.

The proposed system design methodology based on integrated simulation was instrumental for the following findings in connection with ETS. Firstly, a small system

— which is lighter, but also less powerful — does not necessarily result in a further improvement of the benefits compared to larger, heavier systems because ground performance would be affected negatively. Secondly, the physical (e.g. thermal) behavior of the system during a given mission is a key factor as it has an immediate impact on the associated benefit. The optimal system architecture specifically depends on the aircraft and the missions flown; both must be taken into account in the early design phase. Thirdly, the prevailing interest for the ETS technology may be an economic one rather than an environmental one, as electric taxi may be economically viable even in case of increased mission block fuel.

Kurzfassung

Der Bodenbetrieb der Flugzeuge ist der Hauptverursacher von Emissionen in Flughafengebieten. Hierzu tragen insbesondere die Rollbewegungen im Leerlaufschub bei, da die Triebwerke in diesem Arbeitspunkt eine niedrige Effizienz aufweisen. Mehrere Akteure haben unter Anderem den Einsatz elektrischer Fahrwerksantriebe vorgeschlagen, die ein triebwerkloses Rollen ermöglichen. Die Meisten dieser Konzepte sehen das Hilfstriebwerk als elektrischen Energieerzeuger vor. Da diese im benötigten Leistungsniveau deutlich effizienter arbeitet als die Haupttriebwerke, ist ein Vorteil bezüglich Treibstoffverbrauch und Emissionen in der Bodenphase zu erwarten. Nachteilig wirkt sich jedoch das Zusatzgewicht des elektrischen Fahrwerkssystems in den Flugphasen aus. Die Bilanz über die ganze Flugmission muss somit ermittelt werden. Bisher wurden solche Untersuchungen nur anhand gemittelter Parameter und vereinfachter Annahmen insbesondere bei der Betrachtung der Bodenphase durchgeführt, was eine zuverlässige Abschätzung der Einsparungen und deren Sensitivität auf systemparametrische und fahrdynamische Änderungen verhindert.

Die vorliegende Arbeit stellt eine modellbasierte integrierte Methodik zur Bewertung elektrischer Fahrwerkssysteme in der frühen Entwurfsphase vor. Diese Methodik lässt sich zudem auf die Bewertung und Optimierung neuartiger Flugzeugsystemtechnologien verallgemeinern. Sie ermöglicht somit die Beantwortung zentraler Fragen bezüglich der Adoption neuer Technologien, den Vergleich unterschiedlicher Systemarchitekturen und die Ermittlung der zu erwartenden Vorteile unter Beachtung der spezifischen Flugzeug-, System- und Missionseigenschaften.

Die wesentlichen Schritte der Methodik für die betrachteten Fahrwerkssysteme beinhalten die Feststellung qualitativer Anforderungen an die elektrischen Komponenten, die Erstellung parametrischer Flugzeug- und Antriebsmodelle, die dynamische Simulation ganzer Flugmissionen (Gate-to-Gate), und die Anwendung relevanter Metriken an die ausgewerteten Simulationsdaten zur ganzheitlichen Bewertung.

Ein wesentlicher Beitrag zum Stand der Technik ist durch die Generierung optimaler Fahrprofile für eine vorgegebene, zu simulierende Rollstrecke anhand eines konvexen Optimierungsverfahrens gegeben. Dank dieses Verfahrens kann die wirtschaftlichste Fahrweise für jede betrachtete Systemvariante mit geringem Rechenaufwand berechnet und als Fahrvorgabe bei der jeweiligen dynamischen Rollsimulation verwendet werden, was einen fundierten Vergleich der Vorteile unterschiedlicher Systeme unter jeweils besten Betriebsbedingungen ermöglicht.

Die Anwendung der vorgestellten Methodik hat folgende Erkenntnisse zum Thema „elektrische Fahrwerksantriebe“ geliefert:

- Ist die Reduktion des Systemgewichts mit einer Verschlechterung der Systemeigenschaften (Leistung, Drehmoment) verbunden, kann die Gesamteffizienz der Bodenphase überproportional sinken. In der Folge muss die Gewichtsreduktion nicht zwingend eine weitere Senkung des Treibstoffverbrauchs auf Missionsebene hervorrufen.
- Das physikalische (z.B. thermische) Systemverhalten ist entscheidend für die Ermittlung des erwarteten Vorteils. Die optimale Systemarchitektur hängt stark von der Mission ab. Dies muss in frühen Entwurfsphasen berücksichtigt werden.
- Der gesamte wirtschaftliche Vorteil durch die Benutzung elektrischer Fahrwerksantriebe kann deutlicher ausfallen, wenn weitere Aspekte zusätzlich zur Treibstoffersparnis berücksichtigt werden. Das Interesse der Akteure an elektrischen Fahrwerkssystemen kann primär wirtschaftlich sein.

Acknowledgements

I realized this work during my time at the DLR German Aerospace Center, Institute of System Dynamics and Control in Oberpfaffenhofen, Germany. I would like to sincerely thank my former colleagues there. I would especially like to express my appreciation to the Director of the Institute Dr.-Ing. Johann Bals, the Head of the Department of Aircraft Systems Dynamics Dr.ir. Gertjan Looye, and the Head of the Aircraft Energy Systems Team Dr. Dirk Zimmer for their trust and support. I am furthermore indebted to Dr.-Ing. Daniel Schlabe for the countless discussions and comments over the years, and to Dr. Ricardo Pinto de Castro for his feedback on the topic of trajectory optimization.

At the Technische Universität Darmstadt, I would like to sincerely thank Prof. Dr.-Ing. Uwe Klingauf for accepting me as an external Ph.D. student at the Institute of Flight Systems and Automatic Control as well as for his role as first reviewer, and Prof. Dr.-Ing. Stephan Rinderknecht for accepting to be the second reviewer. Among the staff at the Institute, I shall mention Mr. Torben Bernatzky, M.Sc., for sharing useful technical and practical information, and Mrs. Beate Schneider-Kalden for her precious organizational support.

I partly gained my experience on the topic of this thesis in the *Smart Operation on Ground* project within the Clean Sky Joint Technology Initiative. Among all the project partners, I would especially like to thank Dr. David Lemay and Mr. Julien Marques at Safran Messier-Bugatti (now Safran MBD) as well as Mikiel Galea, Ph.D. and Tahar Hamiti, Ph.D. at the University of Nottingham for the data exchange and the fruitful discussions about the architecture of taxi systems as well as suitable electric drives for this application.

Contents

List of Abbreviations

APU	Auxiliary Power Unit
ATC	Air Traffic Control
CoG	Center of Gravity
ECEF	Earth-Centered Earth-Fixed reference frame
ECI	Earth-Centered Inertial reference frame
ECS	Environmental Control System
EGM96	Earth Gravitational Model 1996
EGT	Exhaust Gas Temperature
EMF	Electromotive Force
ETS	Electric Taxi System
FAA	US Federal Aviation Administration
FEP	Fixed Electrical Power
GPU	Ground Power Unit
IFR	Instrument Flight Rules
ICAO	International Civil Aviation Organization
ISA	International Standard Atmosphere
MMC	Engine Material Maintenance Costs
MTOW	Maximum Take-Off Weight
NOTAM	Notice To Airmen
OEW	Operational Empty Weight
PMSM	Permanent Magnet Synchronous Machine
RVDT	Rotary Variable Differential Transformer
SMC	Surface Movement Control
WGS84	World Geodetic System 1984

List of Symbols

Symbol	Unit	Definition
A_{cab}	m^2	Wire cross-sectional area of ETS cabling
AW	kg	Additional weight
$a(s)$	m/s^2	Acceleration along the trajectory (substituted variable)
a_{max}	m/s^2	Maximum acceleration
a_r	m	Lateral distance between vehicle center of gravity and each main gear
b_0	m^2/s^2	Square of the initial speed of the taxi trajectory
$b(s)$	m^2/s^2	Square of the speed along the trajectory (substituted variable)
b_f	m	Longitudinal distance between vehicle center of gravity and nose gear
b_P		Parameter of approximated motor power limitation
b_r	m	Longitudinal distance between vehicle center of gravity and main gear axis
$b_{\bar{s}}$	m^2/s^2	Square of the final speed of the taxi trajectory
C_s		Stefan-Boltzmann constant
c_n	N/m^2	Tire stiffness coefficient in vertical direction
c_0	kg/s	APU idle fuel consumption
c_1	kg/ (kW · s)	APU fuel consumption per unit of power generated
$c_{p,air}$	J/ (kg · K)	Specific heat of air at constant pressure
d_k	m	Distance of k-th trajectory waypoint from start measured along the path
d_n	N · s/m	Tire damping coefficient in vertical direction
$\mathbf{d}$	m	Vector of distances of each trajectory waypoint from start measured along the path
$E_{h,max}$		Maximum allowed heating energy level for each motor over the whole trajectory

Symbol	Unit	Definition
e_{lat}	m	Trajectory tracking error in direction perpendicular to trajectory
e_{long}	m	Trajectory tracking error in direction tangent to trajectory
e_{ψ}	rad	Trajectory tracking course error
F_{cf}	N	Nose gear cornering force (in axial direction of wheel)
F_{yf}	N	Nose gear lateral force (in lateral direction of aircraft)
F_d	N	Net driving force
F_{max}	N	Maximum force
F_{res}	N	Motion resistance
F_{roll}	N	Rolling resistance
F_{slope}	N	Resistance due to ground slope
F_x	N	Longitudinal force in body-fixed frame
F_y	N	Lateral force
F_y	N	Lateral force in body-fixed frame
$F_{yf,max}$	N	Maximum nose gear lateral force
$F_{yi,max}$	N	Tire lateral force at saturation
F_{yl}	N	Lateral force of the left main gear wheel tire
$F_{yl,max}$	N	Maximum lateral force of left main gear tire
F_{yr}	N	Lateral force of the right main gear wheel tire
$F_{yr,max}$	N	Maximum lateral force of right main gear tire
F_z	N	Vertical force
$\mathbf{F}$	N	Generalized forces acting on the vehicle
FL	NM	Flight length
$f(\mathbf{x})$		Objective function in optimization problem
$f_k(\mathbf{x})$		Partial objective function in optimization problem
f_{Lat}	N	Tire lateral force
f_{Long}	N	Tire longitudinal force
f_n	N	Tire vertical force
G_{cs}	W/K	Thermal conductance between ETS motor windings and stator
G_{sa}	W/K	Thermal conductance of ETS motor airgap convection
$g_i(\mathbf{x})$		Inequality constraint in optimization problem

Symbol	Unit	Definition
h_{sa}	$\mathrm{W}/\left(\mathrm{m}^2 \cdot \mathrm{K}\right)$	Convective heat transfer coefficient of the ETS motor airgap
I_{RMS}	A	Rated root-mean-square current of ETS power supply
$\hat{I}$	A	Rated peak current per motor phase
$\hat{I}_0$	A	Rated peak current per motor phase for reference machine
i_d	A	Current component in direct axis
i_q	A	Current component in quadrature axis
J_z	$\mathrm{kg} \cdot \mathrm{m}^2$	Aircraft moment of inertia around the vertical axis of local (body-fixed) reference frame
k_{aero}	$\mathrm{N} \cdot \mathrm{s}^2/\mathrm{m}^2)$	Coefficient of aerodynamic resistance
k_{air}	$\mathrm{W}/\left(\mathrm{m} \cdot \mathrm{K}\right)$	Thermal conductivity of air
k_d		Gain of derivative part of PID longitudinal controller
k_{eng}		Gain of engine throttle control signal
k_i		Gain of integral part of PID longitudinal controller
k_P		Parameter of approximated motor power limitation
k_p		Gain of proportional part of PID longitudinal controller
k_w		Gain of back-calculation anti-windup loop
k_x		Skidding coefficient in anti-lock system
L_s	H	Inductance of one stator phase
L_s	H	Inductance of one stator phase of the reference machine
$L_x(s)$		Trajectory-dependent component of local longitudinal speed v_x
$L_y(s)$		Trajectory-dependent component of local lateral speed v_y
$L_{\dot{\psi}}$	rad/m	Trajectory-dependent component of yaw rate $\dot{\psi}$
l	m	Length of trajectory portion
l_A	m	Axial length of scaled electric motor
l_{A0}	m	Axial length of reference electric motor
l_{cab}	m	Total wire length of ETS cabling
M_z	Nm	Yawing moment

Symbol	Unit	Definition
$\mathbf{M}$	kg	Generalized mass matrix of the vehicle
MF	kg	Mission block fuel
$MF_0\,(FL)$	kg	Fuel consumption of standard flight without additional weight
m	kg	Aircraft mass
m_{cab}	kg	Mass of ETS cabling
m_{mot}	kg	Mass of ETS motor
m_{mot0}	kg	Mass of reference ETS motor
$\mathbf{m}(s)$		Equivalent mass matrix in convex formulation of dynamic equations
$\dot{m}_{airgap}$	kg/s	airgap mass flow
n		number of discretized waypoints along the taxi trajectory
Nu		Nusselt number
P	W	Power
P_{APU}	W	Overall power generated by the APU
P_e	W	Electrical motor power
$\hat{P}_e$	W	Rated electrical motor power
P_{ETS}	W	ETS system power
P_{loss}	W	ETS system power losses
$P_{loss,0}$	W	ETS system constant power losses
P_m	W	Mechanical motor power
$\hat{P}_m$	W	Rated mechanical motor power
P_{max}	W	Maximum motor power
p		Number of motor magnetic pole pairs
$p_X(t)$	m	Vehicle X coordinate along taxi trajectory as function of time
$p_Y(t)$	m	Vehicle Y coordinate along taxi trajectory as function of time
$p_\psi(t)$	rad	Vehicle course along taxi trajectory as function of time
$\mathbf{p}$		Matrix of global coordinates and course angles of each trajectory waypoint
$\mathbf{p}\,(t)$		Vector describing the vehicle trajectory in global coordinates as continuous functions of the time

Symbol	Unit	Definition
Pr		Prantl number
$\dot{Q}$	W	Heat power due to resistive losses in ETS motor
$\dot{Q}_{cs}$	W	Heat transfer rate between ETS motor coil and stator
$\dot{Q}_{sa}$	W	Heat transfer rate between ETS motor stator and the environment through the airgap flow
$\dot{Q}_{se}$	W	Heat transfer rate between ETS motor stator and the environment through the external surface
q		Anti-skid coefficient
R	m	Curve radius
R	m	Wheel radius
R_E	m	Earth radius
R_R	m	Effective wheel radius
R_s	Ω	Resistance of one stator phase
R_s	Ω	Resistance of one stator phase of the reference machine
$\mathbf{R}$		Generalized resistances acting on the vehicle
r_{so}	m	Stator outer radius of ETS motor
r_{si}	m	Stator inner radius of ETS motor
$\mathbf{r}(s)$		Equivalent damping matrix in convex formulation of dynamic equations
Re		Reynolds number
S_{mica}	m^2	ETS motor winding insulation surface
S_{si}	m^2	Stator inner surface of ETS motor
S_{so}	m^2	Stator outer surface of ETS motor
s	m	Path position along the trajectory
s_n	m	Distance between ground and outer wheel profile along the contact line
s_t		Trajectory waypoint where a minimum-time contraint is defined
$\hat{T}$	Nm	Rated motor torque
T	Nm	Motor torque
$T(p)$		Transformation matrix from local (body-fixed) to global reference
T_0	Nm	Motor torque of the reference machine

Symbol	Unit	Definition
T_{avg}	Nm	Average motor torque
T_{diff}	Nm	Differential motor torque
T_{fb}	Nm	Feedback driving torque
T_l	Nm	Driving torque applied on left wheel
$T_{l,ff}$	Nm	Feed-forward driving torque applied on left wheel
T_{max}	Nm	Maximum motor torque
T_r	Nm	Driving torque applied on right wheel
$T_{r,ff}$	Nm	Feed-forward driving torque applied on right wheel
T_{roll}	Nm	Tire rolling resistance torque
t	s	Time
t_{airgap}	m	ETS motor airgap thickness
t_{bc}	Nm	Braking torque commanded by the pilot
t_{mica}	m	ETS motor winding insulation thickness
$\tilde{t}_t$	s	Minimum travel time over a trajectory section from start to the waypoint s_t
$\tilde{t}_t^*$		Parameter used for constraining the minimum travel time over a trajectory section from start to the waypoint s_t
$\tilde{\mathbf{t}}^*$		Vector of parameters used for constraining the minimum travel time in convex trajectory optimization
Ta		Taylor number
$\hat{V}$	V	Rated peak voltage per motor phase
v_{airgap}	m/s	ETS motor airgap flow speed
v_d	V	Voltage component in direct axis
$\hat{v}_d$	V	Rated voltage component in direct axis
v_G	m/s	Ground speed in the aircraft body longitudinal direction
v_q	V	Voltage component in quadrature axis
$\hat{v}_q$	V	Rated voltage component in quadrature axis
v_x	m/s	Longitudinal speed in local (body-fixed) reference frame
$\mathbf{v}_x$	m/s	Vector of longitudinal speeds at each trajectory waypoint

Symbol	Unit	Definition
v_y	m/s	Lateral speed in local (body-fixed) reference frame
v_{slip}	m/s	Tire total slip velocity
$v_{slip,Lat}$	m/s	Tire lateral slip velocity
$v_{slip,Long}$	m/s	Tire longitudinal slip velocity
$\tilde{\mathbf{v}}_{\mathbf{x}}$	m/s	Vector of speed limits along the discretized trajectory
w		Number of waypoints in a trajectory portion
X	m	Longitudinal coordinate in global reference system
Y	m	Lateral coordinate in global reference system
α	rad	Tire slip angle
$\underline{\Gamma}$	1/m	Curvature at start of a trajectory portion
$\bar{\Gamma}$	1/m	Curvature at end of a trajectory portion
γ_n	rad	Angle between initial and current ground normal vector
γ_1		ETS system linear power losses coefficient
γ_2	1/W	ETS system quadratic power losses coefficient
ΔSMF	kg/NM	Increase in specific fuel consumption per flight length unit
Δs	m	Trajectory discretization step
$\mathbf{\Delta s}$	m	Vector of trajectory discretization steps
Δs_k	m	Discretization step between the k-th point and the next point of discrete taxi trajectory
δ	rad	Nose gear steering angle
δ_{fb}	rad	Feedback nose gear steering angle
δ_{ff}	rad	Feed-forward nose gear steering angle
$\delta_{max,k}$		Limit on average relative deviation of tire lateral force between simulation results and measurements for each vertical load
$\delta_{s,k}$		Relative deviation of tire lateral force between simulation results and measurements for a specific slip angle and vertical load
ϵ_{stator}		Emissivity of stator outer surface of ETS motor
ϵ		Weighting factor for the cost functions of path-following optimization
θ_{airgap}	°C	ETS motor airgap temperature

Symbol	Unit	Definition
θ_{amb}	°C	Ambient temperature
θ_{coil}	°C	Copper winding temperature
θ_l	°C	Temperature of the critical point in the left motor
θ_r	°C	Temperature of the critical point in the right motor
θ_{stator}	°C	Stator temperature
λ_A	m	Axial sizing parameter for electric motors
μ		Friction coefficient
μ_{air}	m^2/s	Kinematic viscosity of air
μ_b		Breakaway resistance coefficient
μ_r		Rolling friction coefficient
ρ_{air}	kg/m^3	Density of air
ρ_{Cu}	kg/m^3	Density of copper
Ψ	rad	Course angle
Ψ_0	rad	Initial course angle
$\mathbf{\Psi}$	rad	Vector of course angles at each trajectory waypoint
ψ	rad	Yaw angle
ψ_{PM}	Wb	Magnetic flux of PMSM permanent magnets
ψ_{PM0}	Wb	Magnetic flux of PMSM permanent magnets of the reference machine
$\dot{\psi}$	rad/s	Yaw rate
ω	rad/s	Wheel rotational speed
ω	rad/s	PMSM rotor speed
$\hat{\omega}$	rad/s	Rated PMSM rotor speed
ω_l	rad/s	Rotational speed of left main gear wheel
ω_r	rad/s	Rotational speed of right main gear wheel

1 Introduction

Large airports are generators of noise and pollution that affect the surrounding environment and the local communities. Aircraft ground operations are one important source of emissions, as taxiing is conventionally performed by exploiting the idle thrust of the main jet engines. Idling is a condition in which the engine efficiency is very poor and fuel is also wasted when no driving thrust is needed, as is the case when the aircraft is decelerating or stopped. In addition, jet engines produce a large amount of noise.

Airbus estimates that European flights spend up to 30% of the gate-to-gate travel time and consume 5% to 10% of the entire mission fuel on average for ground operations and taxi [29]. Regarding the main pollutants, aircraft ground traffic especially contributes to CO production significantly due to incomplete combustion in idling jet engines [71]. Also, it has been calculated that aircraft ground traffic contributed to 56% of the overall NO_x production in the London Heathrow airport area in 2002 [37]. These issues are even more concerning considering that air traffic is expected to expand consistently in the future. The demanded Revenue Passenger Kilometers are predicted to grow by 137% in Europe, by 130% in North America, and by more than 200% in the rest of the world over the period 2005-2025, while at the same time, the overall rise in number of Instrument Flight Rules (IFR) based flights in Europe might be as high as 150% under best assumptions [26]. More traffic leads to an increased use of airport capacities, which results in a growing trend for taxi times too. Taxi-out times of US domestic flights increased by 21% between 1995 and 2007; considering only the period 2003-2007, taxi-out times increased by about 11% while taxi-in times also grew by approximately 9% [82].

The issues mentioned above have only been addressed very recently. Traditionally, the interests of aircraft research have understandably focused on flight, whereas the aerospace community has tended to see ground operations as an unavoidable ancillary phase where any technological improvement would not justify the effort. This view is changing as ever-growing environmental awareness and the quest for cost efficiency make it necessary to push optimization to its limits. The potential of improving ground propulsion technologies and procedures has been recognized and the related efficiency increase has become an attractive perspective.

As a first step, optimization of ground procedures has been proposed such as taxi with only a subset of the main engines running [29]. For two-engine aircraft, this is referred to as *single engine taxi*. One jet engine has sufficient thrust to drive the aircraft at constant speed, while accelerating thrust can be provided by increasing the thrust

more than in all-engine operation. Since efficiency rises with the thrust per engine, this results in better overall efficiency. While recognizing the related benefit, airframers like Airbus also point out a number of concerns [14]. Most notably:

- the reduced system redundancy may result in an increased risk of loss of the braking or steering system;
- the asymmetric thrust worsens the maneuverability by making it harder to corner in the direction of the running engine;
- the additional thrust needed for acceleration and cornering increases the risk of debris ingestion and subsequent Foreign Object Damage.

The responsibility of adopting such a procedure is ultimately left to the pilots and the airlines. As a matter of fact, taxi-out is performed with all engines running in most flight missions, while this method is sometimes adopted during either the whole taxi-in or its final portion.

Using a different propulsion system than the main jet engines for ground operations is increasingly being considered as a promising solution. Two different methods are conceivable: towing a conventional aircraft with a ground vehicle similar to the towing tractors currently used for pushback, or equipping the aircraft with a driving system operating on the landing gear wheels to propel the aircraft on ground. While a comparison of the different technologies falls outside the scope of this work, it is obvious that the former technology mainly impacts on the airport infrastructure and ground traffic, whereas the latter strongly influences the aircraft architecture, thus requiring thorough re-engineering in order to integrate the systems.

The focus of this thesis lies on on-board driving systems; throughout this work, these will be referred to as *Electric Taxi Systems* (ETS). Such a system features electric motors fitted in the landing gears in order to perform ground movements electrically while the main engines are off, with the Auxiliary Power Unit (APU) as power source. Being designed for a maximum power of some hundred kilowatts on a narrow-body aircraft, the efficiency of the APU is sensibly higher than the main engines in this power range. Moreover, in an engine-free taxi scenario, the APU needs to be active anyway to generate secondary power for the aircraft systems. Additional power for the green taxi system can thus be generated at a very small extra cost. This solution seems especially promising for narrow-body commercial aircraft.

Designing such an electric taxi system is challenging in many ways. Firstly, integration in the landing gear assembly is an issue, as there is very limited available room in current landing gear designs and the environmental conditions are very harsh. Secondly, a new system brings additional weight to the aircraft, resulting in a lower efficiency in flight and possibly even worsening the overall fuel consumption in a whole gate-to-gate mission. Trade-offs are needed on the ETS design. The system must be as lightweight as possible to minimize the drawbacks in flight, while being still powerful enough to offer sufficient performance for taxi operation. Therefore, the best design for a given aircraft architecture will strongly depend on the profile and length

of the missions typically flown with that aircraft. Eligible designs may require to push the electric system to its operational limits to maximize the benefit and may even force to make concessions on the performance requirements, such as accepting lower taxi speeds.

1.1 Objective of the Work

1.1.1 Problem statement

In the current state of the art, innovative concepts for ground operations have mostly been realized by means of demonstrators and prototypes fitted to existing aircraft types. In particular, this approach has been adopted for the design and investigation of the first on-board electric taxi systems. The interest in this technology derives from the expected fuel savings as well as reduced operating costs and increased efficiency of ground operations. However, concrete figures regarding the expected benefits are difficult to quantify because models and simulation methods for the taxi phase are often too coarse. For instance, while the potential fuel saving over an entire mission has been estimated in [30] for a mid-size aircraft equipped with a generic electric taxi system, the data used for assessing the fuel consumption during taxi are simply based on averaged values such as Thrust Specific Fuel Consumption tables and estimated taxi times. Yet aspects such as the aircraft type, the nature and length of the mission — notably, the relative duration of taxi with respect to the whole mission — and ground traffic largely impact on the requirements and performances of an electric taxi system.

As a matter of fact, while airframers and aerospace professionals generally acknowledge that there is a potential for improvement in ground operations, the lack of detailed studies makes it difficult to identify the conditions in which the benefits outweigh the drawbacks and ultimately puts the adoption of the innovative technology at risk. Specifically for on-board electric taxi systems, while its only direct impact on the aircraft performance while in flight will be caused by its weight, a number of aspects and circumstances will determine the real benefit in ground operations, including the profile of the taxi mission and the system availability due to thermal and electrical aspects. Moreover, an additional indirect impact at aircraft level may be established through the interactions between systems. For instance, when designing new aircraft architectures, the power requirements of the taxi system may be considered during the optimized design of the electrical network, the generators and the APU supplying the taxi system.

On a more general level, the traditional approach to the design of aircraft systems is facing similar issues. Although significant mutual influences exist between aircraft level and system level that would largely impact the conceptual design phase, these complex interactions have often been dealt with in a simplified way in industrial practice so far. A common method features the decomposition of the global design

problem into local design tasks in a single physical domain [70]. System architectures — such as electrical network, cooling system, and Environmental Control System — are defined following the system decomposition dictated by standardizing institutions such as the Air Transport Association (ATA). Local requirements on aircraft systems are then derived from the aircraft level. The local designs of the different systems are then assessed globally by means of *trade factors*, i.e. aircraft-level metrics such as specific performance sensitivities as a function of the local system parameters [73]. Commonly used trade factors include specific fuel consumption increases with respect to design parameters of the subsystem, such as system mass, induced additional drag, or secondary power offtake. The local optimization of the subsystem design is thus driven by the mutual interaction between the trade factors.

These metrics are normally derived at aircraft level, thus before and outside of the local system design process, and their value is not influenced by the local subsystem design process. Beside requiring a relatively low effort concerning modeling and analysis, traditional industrial practice has supported this approach as airframers and subsystem suppliers can limit mutual interaction loops which may otherwise delay development times and pose non-technical issues such as exchange of confidential information. However, this approach only allows to consider system-to-aircraft interactions approximately, whereas it cannot include either aircraft-to-system interactions or mutual interactions between different systems. Considering these aspects has become key for reaching the efficiency improvements pursued in research and development of future aircraft, as conflicting requirements between systems and physical limits at local level impede further improvements if limited to the local system domain [56].

In addition, constant metrics do not take properly into account that performance sensitivities may vary during a mission depending on the flight phase and the momentary conditions. This may prevent a better optimization of subsystem design at aircraft level. To illustrate this issue, consider the design of the cooling system as a basic example. Beside other devices, the cooling system management regulates the ram air intake to control the amount of fresh air entering the system. Ram air usage induces additional drag and is therefore associated with penalizing trade factors. However, drag impacts the global performance differently during the flight. It is negative during cruise and especially undesirable in climb where maximum power is needed, but conversely, it may be less detrimental or even desirable during descent as a means to reduce aircraft speed. The optimization of the cooling system management could be improved for global efficiency if this information were available during system design.

1.1.2 Objectives and contributions

The subsystem design issues mentioned above have recently spurred the development of model-based aircraft system design methodologies. This has been especially boosted by the interest in unconventional aircraft architectures such as the More Electric Air-

craft [51, p. 381 ff.]. A literature review of these initial trends in the conceptual design of aircraft architecture can be found in [73, p. 3-4]. Furthermore, new methodologies and software for integrated system design have been proposed which particularly rely on model-based approaches and integrated simulation of global and local systems for optimization of system parameters. An example is given by the integrated simulation tool prototype developed by Liscouët-Hanke [45], which however relied on strong structural assumptions and fixed operational levels rather than dynamic simulation of system states; also, the tool lacked in modularity. In [70], methods and tools for integrated modeling, model exchange between partners, and co-simulation were presented as a key step towards the development of an integrated simulating platform. Especially, the Modelica [35] modeling language was suggested as a powerful tool for integrated simulation thanks to its object-oriented, equation-based nature making it suitable for modular, physical modeling of complex systems.

Embracing this new paradigm in aircraft subsystem design, this work contributes to the state of the art by presenting an **integrated, model-based methodology to the assessment of aircraft systems at aircraft level in the conceptual design phase and its application to Electric Taxi Systems (ETS)**. The fundamental principle of integrated model-based design features a dynamic physical model of the aircraft and models of the relevant systems. This enables dynamic simulation of several scenarios such as whole flight missions. A more precise performance assessment and parameter optimization at aircraft level is then possible.

The main element is given by the Modelica *Flight Dynamics* Library [46] developed and maintained at the Institute of System Dynamics and Control at the DLR German Aerospace Center. This library enables the realization of multi-disciplinary dynamic models for a variety of aircraft architectures. Flight missions can be simulated dynamically and performances such as fuel consumption and emissions can be evaluated under realistic conditions. Taking advantage of the capabilities offered by Modelica, the aircraft models built with the *Flight Dynamics* Library can be extended with aircraft system models, thus simulating their operation continuously during flight. The models correspond to physical entities and are linked with each other through given interfaces and exchange tools. This modularity allows the realization of separate specific models that are maintained by the respective authors, thus efficiently linking the different fields of expertise into one single, integrated model platform (Figure 1.1).

Using the design of an Electric Taxi System as an example, it will be shown that the proposed model-based process is necessary for answering the following questions regarding the design of innovative aircraft systems while keeping the aircraft type and the specificities of the observed missions into account:

- in which conditions new technologies applied to aircraft systems are beneficial in the overall energetic and environmental balance;
- what sensitivity the overall balance shows with regard to design parameters

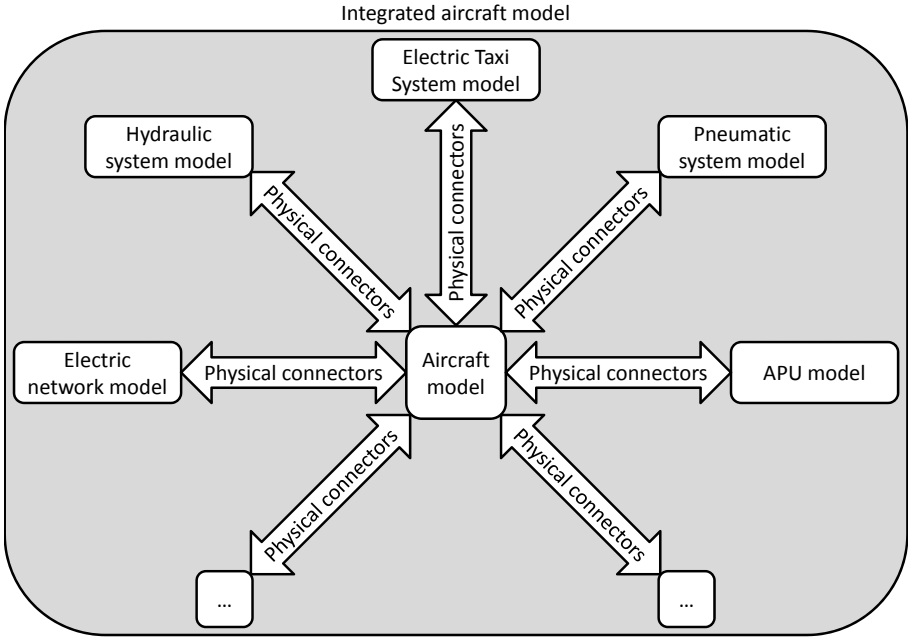

Figure 1.1: **Integrated aircraft model featuring a dynamic aircraft model and various subsystem models linked by interfaces exchanging physical quantities**

and constraints;

- how different subsystem operation modes affect the overall balance;
- what trade-offs are possible between different objectives.

This knowledge is key for concurrent design and optimization of innovative aircraft systems at global level.

By simulating benchmark gate-to-gate missions, the overall benefits of the technology can be quantified, trade-off configurations can be determined for the given flight missions or mission schedules, different subsystem architectures can be investigated separately and their outcomes can be compared. Both airframers and airlines may benefit from the result of this analysis. The former can use the information by integrating trade factors for ETS in the early design phase at aircraft level, whereas the latter may translate the estimated benefits into economic quantities and determine whether an ETS — and which system type and size — is an interesting option even for each single aircraft in the fleet depending on its service schedule. Moreover, the proposed model-based approach can be incorporated to higher-level models, enabling an integrated assessment and optimization of the aircraft and the systems involved (e.g. APU, electrical network) which is a key feature for optimal design of future aircraft. While the proposed approach is applicable to generic aircraft types, the focus

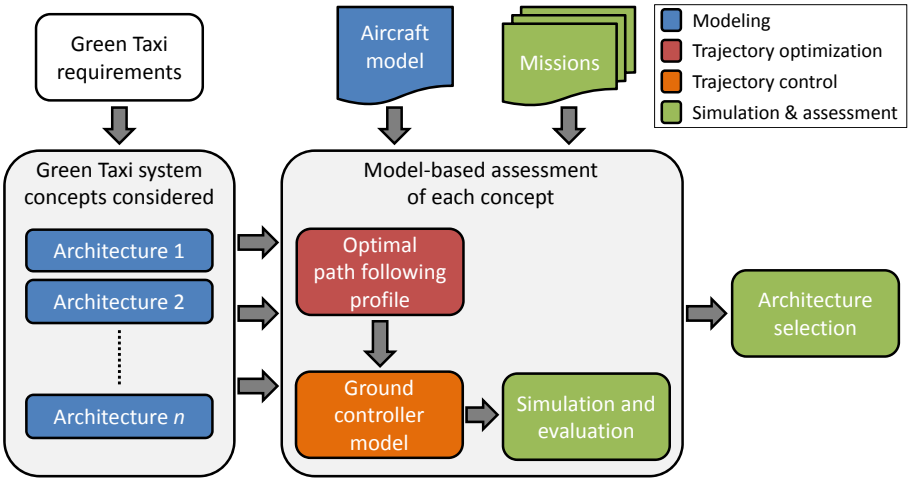

Figure 1.2: **Proposed approach for the assessment of Green Taxi system architectures**

will lie on narrow-body commercial aircraft throughout this thesis. Also, the system assessment will be demonstrated on specific examples for better clarity and for a more transparent interpretation of the results.

Figure 1.2 illustrates the proposed approach highlighting the contributions of the present thesis. Based on the considered aircraft type and on the current state of the art with regard to innovative taxi systems, **generic high-level requirements on ETS** are derived. **Parametric models of the aircraft and of ETS architectures** are then built.

In the simulation phase, the integrated model comprising the aircraft and the ETS model is evaluated for each system architecture by simulating benchmark gate-to-gate missions and using relevant metrics to select the best suitable architecture.

A substantial methodological contribution in the framework of the proposed approach is given by the **automatic generation of energetically optimal ground path following profiles for electric taxiing based on convex optimization.** For the purpose of the work, it is essential to ensure that the ETS is used at the best of its capabilities to guarantee maximum performance within the operational envelope of a given system architecture. Furthermore, a well-funded, more meaningful comparison between different architectures and designs is possible if each system is used in its own optimal operation profile. While the taxi trajectory — i.e. the spatial definition of the motion during the taxi phase — is fixed as part of a given flight mission, the optimal *taxi path following* — i.e. how the trajectory has to be traveled on in terms of speeds and allocation of actuator efforts for over-actuated degrees of freedom — is in generally different for each system architecture considered. Convex optimization is particularly attractive within the proposed methodology because a global optimum can be found for each given problem in short computational time thanks to dedicated

solving toolboxes, thus speeding up the virtual design process.

In this part of the work, an optimization strategy is developed for the path following of assigned taxi trajectories with an aircraft equipped with an ETS. The convex optimization theory is applied to ensure that a globally optimal path-following profile is found for a given taxi system, trajectory and aircraft type. For this purpose, convex formulations of path following problems studied in robotics and vehicle dynamics have been adapted to the aircraft taxi problem. Moreover, convex formulations of relevant constraints in this problem have been derived. On the whole, the presented optimization method is capable of:

- pursuing taxi time minimization or fuel consumption minimization through the formulation of appropriate cost functions;
- considering constraints on the heat generation in the motors as proxy for the motor temperature, thus keeping thermal aspects into account;
- including time constraints that must be observed for clearing given waypoints along the route.

The result of the convex optimization is used as input in the ground phases of the object-oriented mission simulation with the integrated aircraft model. Due to the approximations and uncertainties introduced through the convex transformation of the problem, a **path-following ground controller** is necessary to suppress the taxi tracking error and guarantee precise guidance for each architecture simulated.

In the final step of **model-based Electric Taxi System assessment**, metrics are presented and applied to case studies in order to compare different system architectures and enabling the choice of the best suited one for each case. Moreover, the sensitivity of the results to parameters such as the taxi system sizing, its thermal limitations and the aircraft payload will be determined.

1.2 Structure of the Thesis

This thesis is structured as shown in Figure 1.3 to illustrate the steps of the proposed approach applied to the assessment of an Electric Taxi System.

Chapter 2 gives an overview on the topic of electric taxi. Conventional ground operations are discussed, the state of the art in the current development of electric taxi systems is presented, and high-level requirements on a taxi system are derived.

A dynamic aircraft model is then built that is able to simulate kinematics and dynamics of complete flight missions. The modeling activity is described in Chapter 3: the Modelica aircraft model is presented with particular focus on the landing gear modeling.

The scalable model of Electric Taxi System used throughout the work is presented

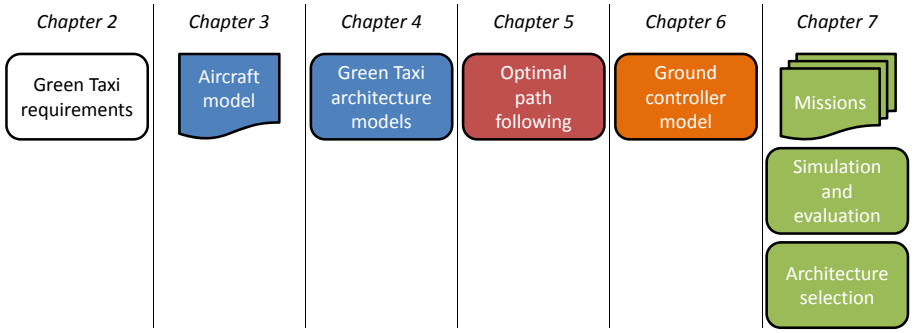

Figure 1.3: **Structure of the present thesis**

in Chapter 4. A specific system architecture is chosen and its Modelica parametric model is realized. The ETS model will be connected to the aircraft model to build the integrated model used for simulation and assessment.

Chapter 5 presents the theoretical background of the convex path-following optimization used to assign the ground trajectories for each specific system type investigated as well as the procedure followed to adapt a generic taxi path-following problem to the convex formulation.

Chapter 6 deals with the design and implementation in the integrated aircraft model of the feedback controller used to drive the aircraft on the ground in order to track the trajectory inputs calculated through convex optimization.

The overall assessment method is demonstrated in Chapter 7: benchmark missions are defined and simulated with the integrated aircraft-ETS model, and different taxi system architectures are evaluated. The sensitivity of those evaluations with regard to various parameters and conditions is also investigated.

Finally, Chapter 8 will give a summary of the methodology and the results as well as an outlook of future developments of the work.

2 Aircraft Taxi: Requirements and State of the Art

In this chapter, the nature and the practices of the taxiing phase will be discussed and basic requirements for non-conventional ground propulsion systems will be derived. This produces the necessary inputs for designing the Electric Taxi System model for the technology assessment example. For this purpose, it is useful to examine first how taxi is performed with a conventional aircraft and identify requirements and critical aspects. Furthermore, the eligible novel ground propulsion technologies will be presented and compared qualitatively. Finally, the current state of the art of such systems will be illustrated by mentioning some currently on-going projects in industry and research.

Parts of the work presented in this chapter were previously published in [61] and appear here in a revised and extended form.

2.1 The Taxiing Phase

Taxiing is conventionally defined as the movement of an aircraft on the ground under its own power [21]. This specifically refers to driving the aircraft from the parking and loading area (terminal gate or apron) to the assigned runway for takeoff, or vice-versa, from the landing runway to the parking or loading area. Taxiing is classified as a phase of flight.

2.1.1 Infrastructure for taxiing

Taxiing is performed on dedicated *taxiways* connecting all airport facilities relevant to aircraft operation. Taxiways are mostly paved with concrete or asphalt in commercial airports and are identified by a unique alphanumeric code (normally a letter or a letter and a number). A number of markings, signs and lights are present on taxiways for orientation, traffic regulation and safety [40]. The layout of airports, including runway and taxiway identifiers, is shown in airport diagrams that are available to the general public. Pilots can use them to plan the ground path between the parking area [1] and

[1] Here, the phrase *parking area* includes any facility intended for aircraft parking, passenger and cargo loading/unloading, refueling, and servicing between different flight missions,

the assigned runway.

At non-towered airports, the pilot makes his own decisions about the ground path based on airport diagrams, experience, observation of traffic patterns, and considering any Notices To Airmen (NOTAMs) about changes at the airport. In towered airports, however, it is mostly the case that pilots are assigned ground routes by Air Traffic Control (ATC) or by a Ground Control authority (also called Surface Movement Control or SMC). Ground Control is responsible for all ground operations and dispatches movements so as to maintain smooth operation within the airport and optimize the efficiency. Nevertheless, it is recommended good practice that pilots still check the airport layout and try to anticipate the path between parking area and runway [32], as this increases awareness on the airport environment, on safety-critical points (known as *hot spots* [33]), and on particular layout situations.

2.1.2 Conventional aircraft devices for taxiing

The following devices allow to control the motion of a conventional commercial aircraft while taxiing.

Main engines

Main engines are used to provide forward thrust. While turboprop engines can produce reverse thrust in a wide range of ground speeds by adjusting the propeller pitch appropriately, turbofan engines that are normally used on commercial mid-range and long-range aircraft — on which this work is focused — can only provide forward thrust at usual taxi speeds. Some models feature thrust reversers that redirect the gas flow backwards causing a reverse thrust, but they are intended only as an aid to slow the aircraft down at landing. In general, thrust reversers should not be used at higher thrust settings and low speeds because of the increased risk of Foreign Object Damage. Also, the efficiency of the engine itself decreases greatly as hot exhaust gases are recirculated into the fan, lowering the fraction of fresh oxygen that can enter the engine and possibly leading to temperature-related problems.

Engines are kept at idle speed most of the time while taxiing, as they usually develop enough thrust to sustain constant speed without slopes or head wind. The engines can be spooled up shortly to produce a thrust impulse, thus accelerating the aircraft from a stop more quickly. When traveling, idle thrust can even be excessive for a desired constant speed, so that the pilot may need to slow down periodically using the brakes. This causes unnecessary brake wear; also, the increase in brake temperature may be critical both before takeoff, where brakes need to be at full efficiency in case of a rejected takeoff, and after landing, when brakes are already hot.

such as passenger gates, aprons, and ramps.

Engine thrust can be regulated separately for each engine. The resulting *differential thrust* generates a yaw moment influencing the lateral motion. This technique is almost only used when negotiating tight curves such as U turns.

Landing gear

The landing gear (also known as undercarriage) sustains the aircraft while on ground and allows it to move along the ground surface. For commercial aircraft used in paved airports, it normally consists of multiple groups of wheels fitted with tires; these assemblies are called *bogies*. The bogies are connected to the aircraft body through *oleo struts* that dampen vertical oscillations while taxiing as well as the touchdown impact at landing.

The most common gear configuration on modern aircraft is the *tricycle gear*, featuring one *nose gear* in the front of the aircraft and at least two *main gears* slightly aft of the aircraft center of gravity, symmetrically placed with respect to the aircraft longitudinal axis. The nose gear normally has two wheels and is steerable. The size of the main gear strongly depends on the aircraft mass, as it supports most of the weight due to its vicinity to the center of gravity. Mid-range, narrow-body aircraft like the Airbus A320 or the Boeing 737 feature two main gears with two wheels each. Wide-body aircraft feature a higher number of main gears with 4-wheel or 6-wheel bogies. The largest and heaviest airplane in service, the Antonov An-225, features a four-wheel nose gear bogie and a total of 28 main gear wheels.

Steering system

The steering system controls the turning angle of the nose gear around its strut, thus allowing lateral control of the aircraft on ground. On commercial aircraft, the pilot commands a desired steering angle through a hand wheel called *tiller*. Rudder pedals, too, control the steering angle; however, the angle range is much smaller as steering by rudder pedals is intended for keeping the aircraft aligned during the takeoff or landing roll. The steering actuation system is normally a hydraulic one. The actuator turns the nose gear according to the command; RVDT sensors feed back the current position.

On certain wide-body aircraft (e.g. the Boeing 747), some of the main gears are also steerable and are turned in a specific relationship to the nose gear steering angle to follow the desired kinematic path with less tire slip and improved maneuverability.

Brakes

Brakes decrease the longitudinal speed while on ground by dissipating kinematic energy. Brakes are normally mounted in the main gears since these offer the most grip

because of the carried aircraft weight; brakes on the nose gear would add significant complexity with little added benefit. On modern commercial aircraft, brakes consist of a series of alternate stator and rotor discs pressed together by a hydraulic actuation system to generate heat by friction. The material used is normally carbon, which has a number of advantages over steel for this application: lower density, higher thermal conductivity, higher specific heat, lower thermal expansion coefficient, higher thermal shock resistance and higher temperature limit [23].

As mentioned previously, brakes are often used for controlling the speed while taxiing when the engine idle thrust exceeds the rolling resistances. This ultimately results in brake wear and an increase in temperature in a critical phase before takeoff or after landing. Experience has especially shown that the number of brake applications is a more important driver for carbon brake wear rather than the braking force exerted, and wear is especially high when carbon brakes are relatively cold, such as during taxi-out [77, 65]. As a consequence, conventional ground operations induce significant brake wear.

Differential braking may be used to generate additional yaw moment, thus aiding the steering system in tight turns.

2.1.3 Taxi-out

Taxi-out is the taxiing phase from the parking position to the assigned runway prior to takeoff. Taxi-out typically starts after the preflight activities and the pre-departure briefing are complete. The contents of these activities and briefings depend on the aircraft model, airline directives and law regulations. At first, all ground equipment is disconnected, including the Ground Power Unit (GPU) or the Fixed Electrical Power (FEP). This implies that the aircraft must have its own power source, thus either the main engines or the Auxiliary Power Unit (APU) must be running at this time.

When the aircraft starts from a passenger gate or a ramp close to the terminal, it usually needs to maneuver backwards to reach a taxiway. Since turbojet aircraft cannot normally do this on their own power, a *towing tractor* (also known as *tug*) attached to the aircraft nose gear must be used to push the aircraft backwards. This phase is called *pushback* and formally precedes the taxi-out phase [21]. When pushback is needed, the main engines are normally started up at its end; the power for the aircraft systems is generated by the APU.

The main engines are normally started up at the beginning of the proper taxiing phase through either bleed air power or electrical power produced by the APU. After the engines have reached the idle speed, the APU is normally switched off as soon as possible to save fuel and APU running hours, as well as to comply with airport regulations about APU usage. Some airlines foresee that the APU still runs until take-off —- provided airport regulations allow to do so — in order to have a backup generator available in case of emergency.

In some airports, the bleed air needed for the engine start is supplied from the ground. In this case, the APU is not needed and the main engines are started before the ground supply is disconnected and the aircraft starts moving.

After starting the main engines and disconnecting the tug, the aircraft taxis along the taxiway path determined by the pilot or assigned by SMC until the assigned takeoff runway. Speeds traveled depend on airframers' guidelines for the aircraft type, airport regulations, weather and ground conditions. Maximum speeds are usually between 15 and 25 KTS (between 28 and 46 km/h) on straight sections and much lower in corners, at about 10 KTS (19 km/h).

2.1.4 Taxi-in

During the landing roll, the aircraft is braked to taxi speed and taxis to its assigned parking position. Speeds traveled are similar to those for taxi-out. All engines are normally running at idle in this phase and may be spooled up shortly to re-accelerate from a stop. Some airlines may have procedures for taxiing in with only one subset of the engines running to save fuel, although this is not common. If the crew is aware that a ground power supply will be missing or not available immediately at the parking position, the APU may be switched on during taxi-in to allow for the prescribed warm-up time before connecting the electrical loads. Upon reaching the parking position, the main engines are switched off.

2.2 Scenarios with a Novel Taxi Propulsion System

In this section, the possibility of using ground propulsion systems other than the main engines will be discussed.

2.2.1 Key issues and limitations

A number of critical aspects need to be considered when evaluating novel taxi procedures. A key one involves the main engine startup and cut-off. Jet engines must be warmed up for some minutes after start before applying take-off power [14]. In conventional taxi, this requirement is already fulfilled while taxiing at idle since taxi-out generally lasts much longer than the warm-up time. However, if different taxi procedures and technologies should be used to minimize the use of the main engines, the engine warm-up time would become a major constraint.

The size, layout and volume of traffic of an airport plays a role in assessing the benefit or even the need for ground propulsion systems. In a small airport with little traffic and short distance between terminal and runway, the taxi-out time might equal

the engine warm-up time, hence conventional taxiing would be unavoidable. However, taxi times are longer in larger and busier airports. Here, the optimal situation would theoretically be reached if the engines were started during taxiing exactly as much time before takeoff as the needed engine warm-up time; the final part of taxiing would be carried out conventionally with the main engine idle thrust. However, predicting the takeoff time with such accuracy is very difficult in practice, as this is ultimately influenced by factors such as the ATC clearance (depending in turn on the local air traffic), the pilots' reactivity, conflicting ground traffic, and possible queues at the runway threshold. Also, safety concerns might prevent arbitrary engine start-up anywhere along the taxiways and might instead require this to be performed in a dedicated area with ground staff and fire protection [14]. The location of this area should be such that the aircraft can easily taxi back to the parking position or at least leave the main taxiways without hindering other ground traffic if the flight needs to be aborted. While such a requirement would limit the benefits of a ground propulsion system in the general case, time-consuming situations like queues at the runway threshold in larger airports or de-icing procedures could be exploited to start up the main engines.

After landing, especially after using thrust reversal, the engines also need to run at idle for a cool-down time of some minutes. Again, idling engines can be exploited to taxi conventionally in the first portion of taxi-in, whereas the ground propulsion system would be active in the second part. This scenario is not as critical from the point of view of safety as taxi-out, since engine cut-off does not pose particular safety risks.

2.2.2 Technical requirements

The ground propulsion system should be used for standard aircraft ground operations. This results in the first requirement that the system shall be capable of moving the aircraft freely in the usual two-degree-of-freedom domain of ground vehicles, i.e. longitudinal motion and coupled lateral and yaw motion. It must especially be able to drive the aircraft both forwards and backwards. This requirement should not pose a particular concern since the eligible technologies (e.g. electric motor drives) can normally be operated in both directions with little or no added system complexity.

The required performances represent a central aspect in the development of a ground propulsion system. A trade-off must be found between the concurring factors of sufficiently high performance on ground, system weight (if onboard), infrastructural constraints, and size of the power source for the system. The ground performances have an influence on the taxi time of the aircraft itself as well as on the interaction with other traffic. Therefore, operational requirements should be used to define minimal performances. While comprehensive fast-time simulation models at airport level and analyses of various regulations and procedures are needed to assess these effects precisely, some limited qualitative considerations will be made here to obtain a rough

estimate of the system power needed.

One critical situation during taxiing is crossing an active runway. This maneuver should be quick enough so as not to perturb the air traffic. In a typical scenario, the taxiing aircraft stops at a holding position before the runway, obtains a clearance to cross from ATC, then accelerates and performs the crossing. The International Civil Aviation Organization (ICAO) prescribes a minimum distance of 90 m from a precision-approach-category III, code 4 runway centerline to the holding position of a trafficked taxiway [40]. For the same case, the Canadian transport authority *CanadaTransport* prescribes a distance of 115 m [80]. Considering the latter, more severe constraint, a possible performance requirement can then be of the following form: the performance of the ground propulsion system shall be such that the aircraft is able to cover twice the distance of 115 m starting from a stop within a prescribed time. The aim of this requirement is to ensure that a runway is completely crossed within the given time. More precise requirements can be formulated if the taxiway slope is also considered. ICAO allows a maximum taxiway slope of 1.5% [40].

Considering an Airbus A319, the breakaway forces that must be overcome to set the aircraft in motion are shown in [68] to be about 6 kN on flat ground. The rolling resistance then drops below the breakaway value once the aircraft is moving. To err on the side of caution, the rolling resistance will be assumed constant at $F_{roll} = 6$ kN over the whole taxi speed range while other resistances (e.g. aerodynamics) are neglected, being relatively small at the considered speeds. With regard to the ideal characteristic of a driving system illustrated in Figure 2.1, a system with a maximum force $F_{max} = 26$ kN is assumed; the net driving force is then $F_d = F_{max} - F_{roll} = 20$ kN. Considering a mid-size aircraft like the A319 mentioned above with a maximum takeoff weight $MTOW = 80$ tons, the maximum acceleration from standstill results $a_{max} = F_d/MTOW = 0.25$ m/s^2. Fixing the required maximum crossing time at 45 s and solving the problem numerically for the power, the 230 m distance is covered in less than 45 s if the power of the propulsion is at least $P = 129$ kW. A real system should also allow for taxiway slopes: the ICAO maximum allowed taxiway slope is 1.5% [40], resulting in an additional resisting force of approx. $F_{slope} = 11{,}770$ N for the mass considered, hence higher system performance will be needed. Repeating the calculation for the case with a constant 1.5% slope with $F_{max} = 36$ kN, $P = 200$ kW, the time needed to cover 230 m is about 46.5 s. The power value of 200 kW has been chosen because it can be an approximate power limit for onboard systems on a narrow-body aircraft, as will be explained in Section 2.3.2.

2.3 Types of Novel Ground Propulsion Systems

Two categories of systems are conceivable for this application: external devices that are connected to the aircraft while on ground and drive it along the ground path, and on-board systems that are highly integrated within the aircraft.

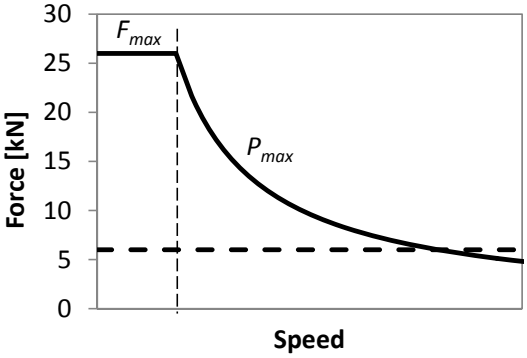

Figure 2.1: **Ideal motor characteristic (solid line) with initial constant force region and subsequent constant power region, and constant rolling resistance of aircraft (dashed line)**

2.3.1 External systems

Since pushback is normally performed with a towing tractor, it seems a natural extension of this procedure to use the tug for pulling the aircraft forwards along the assigned ground path to the runway. This method, sometimes called *dispatch towing*, will be referred to as an *external ground propulsion* in the following as it does not ideally require additional equipment or major modifications on the aircraft.

Examples of a conventional tug currently used for towing single-aisle commercial aircraft are given in Table 2.1. Comparing these data with the simple calculation performed in Section 2.2.2, it is apparent that the tractors provide a good acceleration from standstill due to the high maximum drawbar pull, but the low power will result in poor overall performance, thus making them unsuitable for taxiing. Also, current tractors are coupled to the aircraft through a drawbar connected to the nose gear strut. Larger pulling power may require either a strengthened nose gear structure or a different kind of mechanical connection. Finally, because current regulations consider taxi as a phase of flight, the pilot has the responsibility while taxiing. This is a critical issue for external systems because the pilot must have the ultimate control of the aircraft motion, which is not the case when the aircraft is pulled by a conventional tractor. For all these reasons, it is not possible to use present-day tractors for taxiing, but external ground propulsion requires new vehicles and different technologies.

In this class of systems, the TaxiBot project is being carried out by a consortium with Israel Aerospace Industries, TLD, Airbus, Siemens and Lufthansa LEOS [25, 49, 13, 19]. TaxiBot is a towing tractor that connects to the aircraft by embracing the nose gear and loading it onto a platform instead of using a conventional towbar; this kind of connection is claimed to be compatible with the regarded aircraft types without modifications. The tractor pulls the aircraft with its own diesel-electric drive. The

Table 2.1: **Specifications of two models of towing tractor for single-aisle commercial aircraft**

Make and model	Eagle Tugs XL Series	GSE TT15
Engine	Deutz 3.6L, 4-cylinder aspirated Diesel	Deutz TCD2012 Diesel
Transmission	hydromechanic, 3 forward and 3 reverse speeds	N/A
Power	89 kW @ 2800 rpm	75 kW @ 2400 rpm
Max drawbar pull	133 kN	120 kN
Maximum speed	23 km/h	26 km/h
Towing capacity	168,963 kg	N/A

aircraft pilot can directly control the tractor by steering the nose gear and applying the conventional brakes for slowing down; both the rotational motion and the longitudinal force are detected by the platform and transformed in control signals for the driving force and the steering angle. The pulling force is monitored in order not to exceed the admissible load envelopes on the nose gear. A driver is still needed to control the vehicle when not towing, as well as in case of emergency. Two tractor sizes are planned for wide-body and narrow-body aircraft respectively. At time of writing, three narrow-body prototypes have been certified for use with the Boeing B737 Classic and are being tested in everyday operations at the Frankfurt airport; the certification and test of the wide-body variant is expected in 2016 [19].

2.3.2 On-board systems

An on-board system features a number of motors driving one or more wheels of the landing gear. Given the technical and environmental advantages, the propulsion system is assumed to be an electric one. The key differences between those systems are in the number, type, disposition, and mechanical integration of the motors —- aspects which have an impact on the aircraft weight among other things — and in the source of electric power.

The integration can be easier in the nose gear because of its simpler structure. In particular, due to the absence of the brakes, more room is available within the wheel rim. However, a number of facts have been pointed out against an integration into the nose gear [31]. The weight on the nose gear might be too small to assure the needed friction between tire and ground in all surface conditions, as the aircraft center of gravity is generally in the proximity of the main gear. The nose gear sustains only around 10% of the aircraft weight [68]; this value can be even lower depending on the aircraft weight distribution. Also, because the extended nose gear forms an angle off

the vertical on some aircraft (e.g. on the Airbus A320 family), one of the two wheels can lose contact with the ground at larger steering angles; this may compromise the functionality of two-motor designs. Finally, the additional weight would require extensive redesign of the structure and retraction system of the nose gear and may negatively impact on shimmy behavior and retraction time.

As far as a main gear based propulsion system is concerned, the mechanical integration of the motor and its connection to the wheel are critical. Placing the motor in the aircraft body, in or near the landing gear bay and adding a mechanical linkage to the wheel in the gear strut adds a great deal of mechanical complexity to the landing gear design and is not deemed feasible without dramatic architecture changes. The other solution of placing the motor within the main landing gear assembly is the more feasible one. However, it adds weight to the landing gear and, more importantly, it may conflict with the brakes and the brake cooling fans, making integration with current aircraft challenging and possibly leading to a major gear re-design. An important aspect is also whether a driveline architecture with a reduction gear is chosen, or a larger, high-torque motor with direct drive: the former solution allows the use of smaller and lighter electric motors at the price of an increased risk of failure and more difficult mechanical integration due to the additional gearbox.

One major requirement for an on-board system is that either the system should withstand the high rotational speeds and accelerations reached in the takeoff roll and at touchdown, or a mechanical disengagement system should be present. The former requirement results in stronger, thus heavier motors and in electronic controllers capable to handle the high voltages generated at high speeds. The latter once again adds mechanical components (e.g. a clutch) thus increasing the system complexity and in turn the risk of failure.

An additional feature of an onboard system would be the capability to spin up the wheels immediately prior to touchdown in order to reduce the tire wear. It is questionable if such a feature would be feasible with little effort since motor drives designed for taxi speeds may not be able to spin up to the very high touchdown speeds.

As regards the power supply, an interesting solution consists in using the Auxiliary Power Unit (APU). The APU normally supplies the onboard electrical network and produces bleed air for the pneumatic system, which in turn is used for starting the main engines and, depending on the aircraft type, for the Environmental Control System (ECS). Using the APU during most of the on-ground time while keeping the main engines off results in a reduction of noise, consumption and emissions, because the APU engine is more efficient in the power range in question than the jet engines at idle.

A Honeywell 131-9(A) APU, which is mounted on the Airbus A320 family, is considered as an example. This APU produces a total power of about 300 kW, of which the 115 VAC generator power uses up to 90 KVA [12]. Up to about 200 kW are used by

the air bleed compressor. As usual with jet engine generators, the APU is regulated for constant (optimal) speed by changing the fuel flow in dependence of the drawn power. At idle, this APU burns about 78 kg/h of fuel, while the fuel burn rate is 95 kg/h at full 85 kW generator power and about 130 kg/h at full load with generator and air bleed [39].

A power of 200 kW is available from the APU whenever air bleed is not required, or under the assumption that both generator and compressor are drawing less than 100 kW overall during taxi. This explains why a maximum power of 200 kW was set in Section 2.2.2 for the ground propulsion system. An APU load management system may be necessary to temporary limit non-essential loads such as the ECS when maximum power is requested by the electric taxi system. A change would be needed in the APU usage procedures: it needs to be running during the whole taxi phase to supply the ground propulsion system, except when the main engines are on. Finally, air bleed cannot be produced and the engines cannot be started while the ground propulsion system requires full, or nearly full APU power. This would possibly not result in practical limitations since there may be a requirement that the aircraft should be stopped in an appropriate location for engine start-up due to the safety concerns mentioned in Section 2.2.1.

A more radical solution is to use a different, cleaner power source for the ground propulsion system, for instance a fuel cell. It needs to be noted that such an aircraft would still need a power supply for the on-board electrics and pneumatics, hence a rational choice would be to replace the APU completely with a fuel cell power source. While fuel-cell based ground power systems are being researched [58], the remarkable challenges regarding the weight, integration and safety of the fuel cell, and the fuel supply system are such that this solution may only prove mature in the long term if at all.

Current research projects

In the following, some currently on-going projects are mentioned that are researching and developing on-board ground propulsion systems.

The first prototypical realization of a motorized landing gear was WheelTug [7]. Explicitly designed for retrofitting of existing aircraft, this system is mounted in the nose gear and features two Chorus Motors machines and a planetary reduction. The system is supplied by the APU and is governed by the pilot through dedicated controls in the cockpit. The first proof of concept on a Boeing 767 dates back in 2005, while in 2010, tests were made with a Boeing 737 at the Prague airport. The start of the series production is envisaged for 2016.

The German Aerospace Center DLR, Airbus and Lufthansa Technik have demonstrated a ground propulsion system with electric motors integrated in the nose gear of an Airbus A320 and powered by a hydrogen fuel cell [68] (Figure 2.2). The system was

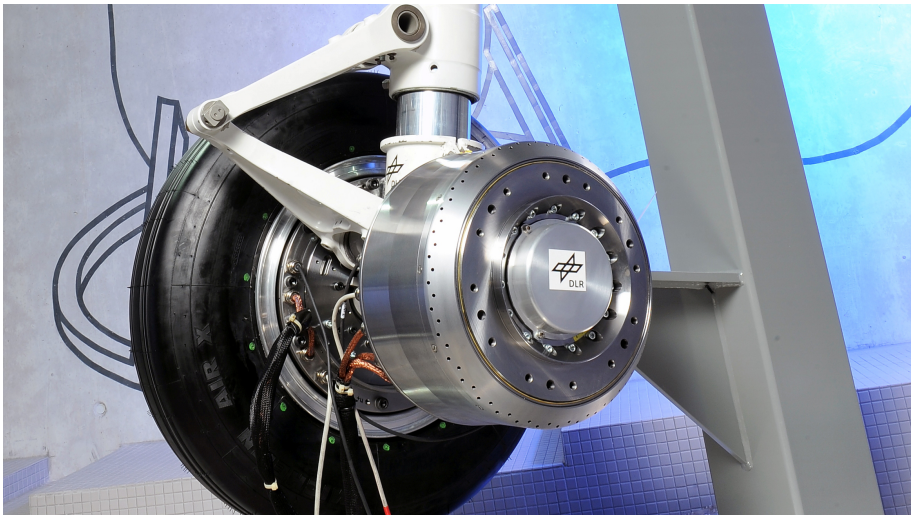

Figure 2.2: **Electric nose wheel drive demonstrator developed by the German Aerospace Center DLR, Airbus and Lufthansa Technik (Image: DLR, CC-BY 3.0)**

tested in July 2011 at the Hamburg Finkerwerder airport. Each of the two permanent magnet synchronous motors has 8 pole pairs, features a maximum torque of 450 Nm and is connected to each nose gear wheel through a 12:1 planetary reduction gear. It is also possible to change the gear into direct drive in order to spin up the nose gear wheels immediately before touchdown and reduce tire wear. While the total power of 50 kW makes this demonstrator still unsuitable for practical application, the global daily fuel saving with this technology at a large airport like Frankfurt has been cited as potentially being as much as 44 tons with about 17-19% emission reduction and almost 100% noise reduction [2].

In the frame of the CleanSky Joint Technology Initiative [6], the *Smart Operations on Ground* work package dealt with developing a prototype of electric motor for ground taxiing to be integrated into the aircraft main gear. Safran, Airbus, the DLR German Aerospace Center and University of Nottingham participated in this project. The feasibility and a possible drive design are discussed in [59]. Among other things, the challenges are the thermal behavior of the motor, the thermal influence of the neighboring brakes and dealing with the takeoff and landing phases as no mechanical clutch is foreseen.

Along with this, Safran launched a separate “Green Taxiing” project [67, 31] together with Honeywell in 2008 aiming to build an electric taxi system prototype and market it by 2016. Retrofitting on current aircraft was also considered. The system being developed features direct-drive, not disengageable synchronous motors integrated within the main gears.

Finally, the on-board electric propulsion system tested by Lufthansa Technik, L3 and Fraport shall be mentioned [48]. Electric motors were fitted into the main gear of an Airbus A320 after removing the brakes and rolling tests were carried out with different duty cycles in order to collect data for future system design.

3 Aircraft Modeling

This chapter presents the aircraft model used in this work. Its purpose is to simulate whole gate-to-gate missions dynamically and evaluate performances such as the fuel consumption as well as the behavior of the system models included in the simulation. For efficient simulation, different parts and domains of the system will need to be modeled on different levels of complexity according to their impact on the aspects examined.

Regarding flight simulation, the objective of this work requires aerodynamics and engine models that are precise enough to assess the sensitivity of the fuel consumption to mass variations in the order of magnitude of 10^1 kg, as well as APU models putting the fuel consumption and the power drawn by the supplied loads into relationship. Conversely, high dynamic precision — such as dynamic response or actuator behavior — is not necessary. These models do not need to reproduce the underlying physics, but they may also be grey-box or black-box models. When applying the approach proposed in this thesis to a real aircraft type, the used models should be validated for that aircraft type to guarantee accuracy of the results. As models explicitly validated for a real aircraft type were not available, non-validated models were used that are representative of a narrow-body commercial aircraft.

Concerning ground simulation, accurate tire modeling is needed. Ground dynamics are key for assessing the performance of the ETS, as this is highly influenced by the time behavior of the relevant dynamic quantities. For instance, studying the thermal behavior of the ETS motors requires accurate knowledge of the applied power, which in turn depends on the speeds traveled and the variable motion resistances along the taxi path. These derive from factors such as the tire rolling resistance, the nature and number of corners, et cetera. Therefore, accurate tire models should be used. Although less computationally demanding tire models exist such as rigid tire models not allowing any slip or deformation, they are unable to simulate the change in tire behavior as the vertical load changes, effectively acting as a wheel-rail constraint during motion. This is not acceptable in the model used in this work, which must be able to simulate whole missions including flight phases. Therefore, more complex tire models are needed that can simulate the tire behavior under slippage realistically.

Parts of the work presented in this chapter were previously published in [62] and appear here in a revised and extended form.

3.1 Modeling Paradigm and Language

Object-oriented modeling in the *Modelica* [35] language has been chosen for this work. Modelica is a declarative language, i.e. one where the control flow of the computation is not defined a priori. A Modelica object-oriented model features a set of sub-models called *classes*. They are normally roughly coincident with single parts, assemblies, or physical and environmental phenomena relevant to the model. Classes interact together by means of appropriate interfaces called *connectors* where common variables, signals and system states are exchanged. This offers a number of advantages over other modeling paradigms such as the widespread signal flow modeling used e.g. in Matlab/Simulink. The modular structure with models and connectors makes it possible to build physical models of single components and sub-assemblies of the real system. This results in more realistic models, allowing a better, more intuitive understanding of the models for the engineer. Also, the principle of classes and modules is very suitable for building discipline-specific libraries and makes it easier to modify or expand a system without major modifications of the entire model or cumbersome code editing. In addition, a great advantage of a declarative language is that the causality of the system model is not determined in the modeling phase. Inputs and outputs are specified only upon compilation of the executable simulation code. This improves the model flexibility dramatically, because a direct model and an inverse model can be generated easily from the very same system model with only minor modifications. An example of this feature is given in [47] in the context of automatic model-based controller generation. This work used the simulation environment Dymola [5], which is based on Modelica and also features a graphic layer where classes are represented as blocks and can be connected to each other in a signal-flow-like fashion.

3.2 Libraries used

In the following, some libraries used, enhanced or modified during this work are presented.

3.2.1 Modelica Multibody Library

The Multibody Library [54] is a subpackage of the freeware Modelica Standard Library, which comes with most Modelica environments. It allows dynamic modeling of three-dimensional mechanical systems. It features a number of classes such as mechanical elements, masses, forces, torques and joints. Parts can be linked together through *multibody connectors* allowing the mutual exchange of forces and torques. Each instance of such a connector in a class is called *frame* and generates a local coordinate system including its rotation matrix to the global system. A global *World* component sets the

absolute coordinate system and determines global parameters such as the gravity field.

3.2.2 DLR Flight Dynamics Library

The Institute of System Dynamics and Control at the DLR German Aerospace Center has been developing a Modelica *Flight Dynamics* Library [46]. It is an extensive library of aircraft parts and relevant physical phenomena with the aim of realizing and simulating integrated, multi-disciplinary dynamic models for a variety of aircraft architectures. Over the years, the library has been expanded with enhanced classes and models and now allows to realize fairly complex models covering flight dynamics, structural dynamics (rigid and flexible aircraft), avionics, electrical network, and hydraulics.

The library is based on the Multibody Library as far as the mechanical connections are concerned. In addition, other global classes define atmospheric conditions and terrain characteristics as well as the World Geodetic System 1984 (WGS84) standard for the global reference system. A bus connector allows the exchange of several variables and parameters between the classes of the aircraft model.

The main components of the library needed to build an aircraft model in an appropriate environment are listed as follows (see Figure3.1):

World model This model provides the reference point of the Earth-Centered Inertial frame, which will be the absolute reference system for all model components. Furthermore, the model provides a geodetic reference based on the WGS84 standard which results in an Earth-Centered Earth-Fixed reference frame; a model of the Earth's gravitation based on the Earth Gravitational Model 1996 (EGM96) standard; a model of the Earth's magnetic field based on the World magnetic Model from the US National Geo-Spatial-Intelligence Agency. The world model makes use of the Modelica *outer/inner* feature. The world component is declared as *inner* model, and all submodels within the aircraft model declaring a dependence on the world model as an *outer* model will have access to all variables and functions of the world model even without an actual connection between the models. This is a convenient way to model environmental phenomena and field effects in Modelica and also allows to insert more than one aircraft model into the same environment.

Atmosphere model It contains atmosphere data either as constant atmospheric conditions or according to the International Standard Atmosphere (ISA) as a function of height. Wind fields can also be implemented. Being again an *inner* model, the data can be accessed by all submodels declaring it as *outer* model.

Terrain model It contains models of the Earth surface with various levels of detail as well as functions for determining the latitude, longitude and height of any point in the absolute (ECI) reference frame.

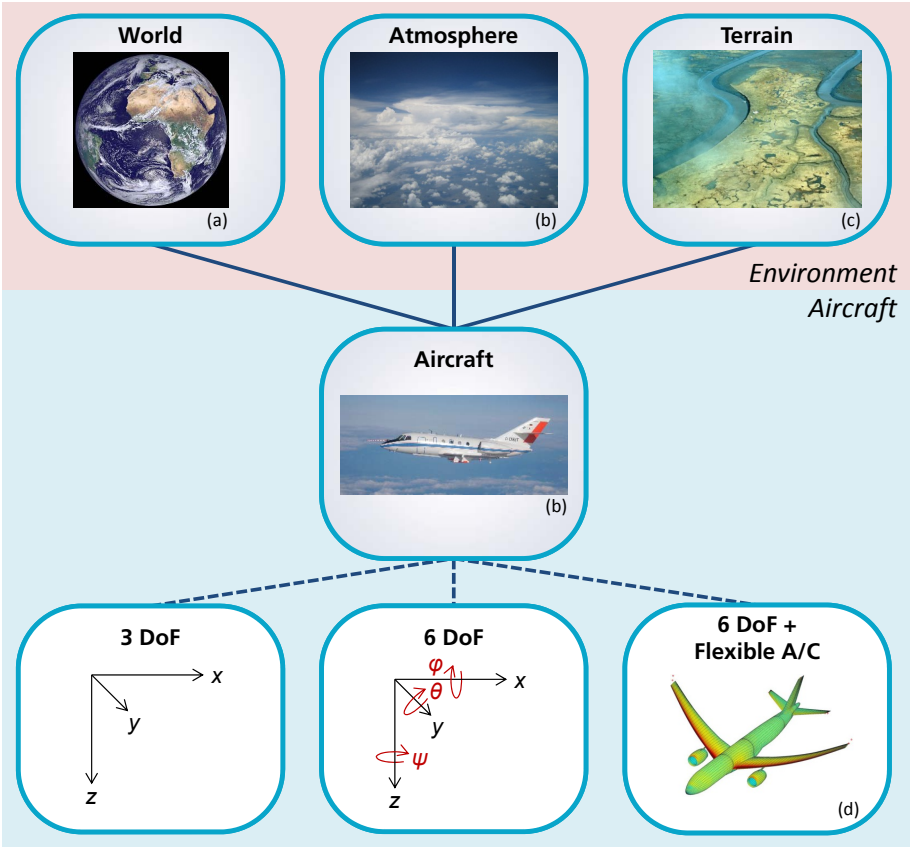

Figure 3.1: **Domains covered by the DLR *Flight Dynamics* model library for building of aircraft models (Images: a) DLR/EUMETSAT; b) DLR (CC-BY 3.0); c) U.S. Fish and Wildlife Service; d) T. Kier, DLR [42])**

Aircraft model It is a structure of several submodels of physical components (airframe, engines, actuators, sensors) and flight-relevant phenomena (kinematics, aerodynamics, wind). The submodels are linked together through mechanic connectors from the Modelica Multibody library as well as a signal bus for exchanging variables across submodels. Various component models exist that can be combined to build different aircraft types, e.g. rigid versus flexible aircraft.

While the Flight Dynamics Library featured very simple landing gear models containing basic force interactions, their level of detail was not adequate for the scope of this work. Therefore, completely new landing gear models have been developed and integrated into the Library, as will be described in the next sections.

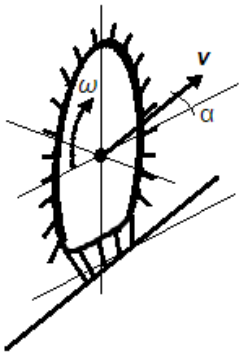

Figure 3.2: ***Brush model* for tires. The tire is represented as a disc with several elastic bristles departing radially from the contact edge. (Image based on [55, p. 94])**

3.3 Tire Model

Tires are the connecting elements between the taxiing aircraft and the ground. Tires provide the necessary friction for controlling the aircraft on the ground and determine the dynamic behavior of the taxiing aircraft to a large extent. Therefore they need to be modeled with high level of detail for the scope of this thesis.

3.3.1 Generalities about tires

A simple physical model called *brush model* shall illustrate the basic principles underlying tire dynamics (see [55] for further reference). The tire *tread*, i.e. the circumference making contact with the ground, is modeled as as a set of one-dimensional radial elastic bristles on the circumference of a rigid disc (Figure 3.2). The elasticity of the bristles reflects that of a portion of the real tire as wide as one bristle. The downward force acting on the tire due to the vehicle weight results in a pressure distribution which is assumed parabolic for simplicity[1]. Friction is present in the contact zone, thus each bristle will adhere to the ground as long as the vertical force due to the pressure distribution is enough. As long as the wheel rolls freely without any torques acting on it, the velocity vector will lie in the wheel plane and the bristles will not deflect horizontally. However, if the vehicle kinematics causes side slip to occur — i.e., the velocity vector forms a *sideslip angle* with the wheel plane — then the bristles will deflect horizontally resulting in a lateral force with respect to the wheel plane (Figure 3.2). A bristle entering the contact zone in the forward part will be deflected linearly as it proceeds through the contact zone until the horizontal force is equal to the vertical

[1] In a real tire, pressure is higher in the front part with respect to the traveling direction due to hysteresis of the deflected tire. This is the primary cause for rolling resistance.

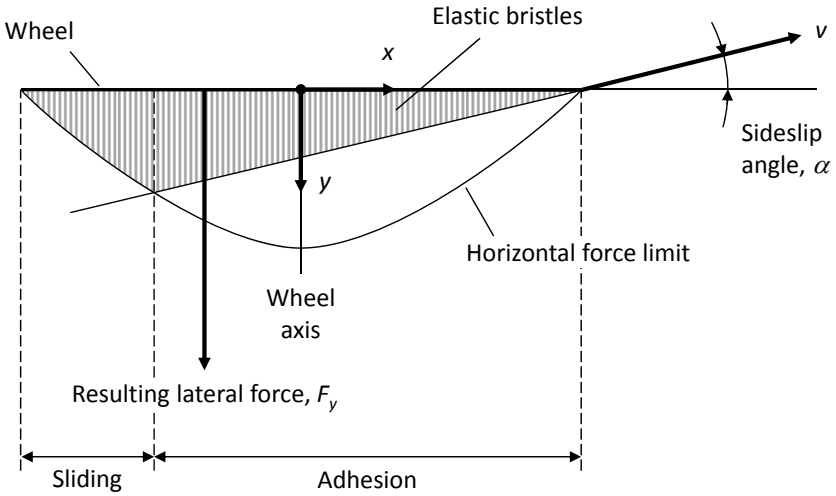

Figure 3.3: **Generation of tire lateral force due to side slip according to the brush model. View from above onto xy-plane (ground plane) (Image based on [55, p. 94])**

force multiplied by the friction coefficient. From this point on, the horizontal force of the bristle will be saturated, and as the vertical pressure diminishes in the aft part, the bristle will slide back to the wheel plane until it leaves the contact patch and the contact with the ground will be lost. The combined effect of all bristles in the contact zone results in a global lateral force F_y (Figure 3.3). As the sideslip angle grows larger, each bristle will reach saturation earlier, and more and more bristles will be saturated simultaneously at a given time. For a large sideslip angle, all bristles in the contact patch will slide, which results in saturation of the global tire lateral force.

Similar considerations explain the generation of longitudinal force due to an axial torque acting on the wheel and the subsequent longitudinal deformation of the bristles. The decisive kinematic quantity in this case is the difference between the velocity component of the wheel center in the wheel plane and the peripheral wheel speed. This simple model implies that the longitudinal and lateral maximum force must be equal because it is determined in both cases by saturation of the same number of bristles touching the ground. However, real tires show an anisotropic behavior mainly due to tread design and anisotropic elasticity of tread and carcass.

When longitudinal and lateral slip occur together, a combined slip condition arises in which the bristle deformation will show an angle relative to the ground plane. The dynamic behavior results from the vector addition of the effects in longitudinal and lateral direction. As a consequence, saturation will be reached earlier, thus the maximum force will be lower for a given slip quantity in one direction if the tire is also slipping in the perpendicular direction.

3.3.2 Physical tire model used

A general-purpose tire model library was already available at the DLR at the beginning of this work. The Modelica *WheelDynamics* library [86] is a set of parametric physical models of road vehicle tires with different levels of complexity. One of these models has been picked for this work. Two major modifications of the original model were necessary for compatibility with the Flight Dynamics library. The first change involved replacing the global reference system with a new ground-fixed reference system. Secondly, expressions were added to describe the position and orientation of the ground surface tangent to the Earth below the wheels at each time instant. Both modifications solved the compatibility problem that the Wheel Dynamics tire model is conceived for simulation of road vehicles on a flat ground fixed in the origin of the global reference frame, whereas the Flight Dynamics aircraft model considers the curved Earth geoid and places the global frame in the Earth center.

The chosen model features a Modelica Multibody connector for exchanging forces and torques with another linked model — which will be the model of a landing gear part. This connector is ideally placed in the wheel center and contains its coordinates in the absolute reference system and the rotation matrix from the absolute to the local reference system, from which the absolute linear and rotational velocities can be derived. The longitudinal and lateral slip velocities $v_{slip,Long}, v_{slip,Lat}$ of the tire tread with respect to the ground are used as variables in the tire dynamics. The total slip velocity is the vector addition of these velocities:

$$v_{slip} = \sqrt{v_{slip,Long}^2 + v_{slip,Lat}^2} \tag{3.1}$$

Radial elasticity determines the tire vertical load f_n according to the following spring-damper expression:

$$f_n = \begin{cases} 0 & \text{if } s_n > 0 \\ -(c_n s_n + d_n \dot{s}_n) & \text{if } s_n \leq 0 \end{cases} \tag{3.2}$$

where s_n is the distance between the ground and the undeformed wheel outline measured along the contact line, c_n is the tire radial stiffness coefficient, d_n is the tire radial damping coefficient, and $\dot{s}_n$ is the time derivative of s_n. Wheel and ground are in contact when $s_n <= 0$, and in this condition, s_n indicates the deflection of the tire tread due to the vertical load.

Regarding the dynamics of this model, the tire force is a function of the slip qualitatively similar to the diagram in Figure3.4 and lies in the same direction as the slip. The behavior of this curve is described by means of model parameters. The friction coefficient will be maximum at the slip factor s_{opt}, called *sAdhesion* in the model because this is the highest slip at which the contact patch is still in complete adhesion. The friction coefficient will decrease to an asymptotic value at the slip factor s_∞, called *sSlide* in the model because complete sliding occurs above this slip factor. For each of

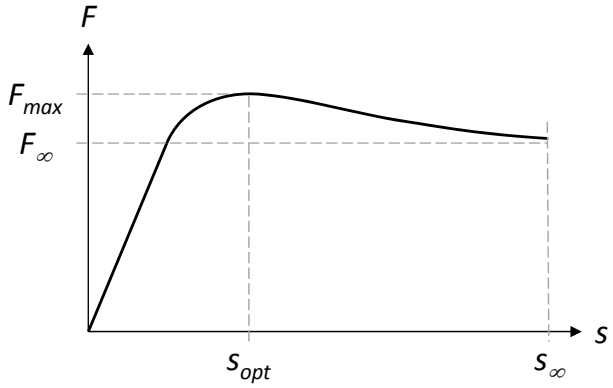

Figure 3.4: **Qualitative behavior of the tire force as function of tire slip in the tire model used**

the two directions, two friction coefficients are given as parameters called *muMinLong*, *muMaxLong* resp. *muMinLat*, *muMaxLat*, and two slip coefficients called *sAdhesionLong*, *sSlideLong* resp. *sAdhesionMinLat*, *sSlideLat*. Two sets of such parameters are given for two different vertical loads $f_{n,1}$ and its double $f_{n,2} = 2f_{n,1}$. This is used to represent the influence of vertical load on the tire behavior.

Firstly, the two parameter sets are interpolated according to the current vertical load f_n. Then for the current sliding direction, the parameters *muMax*, *muMin*, *sAdhesion*, and *sSlide* are determined by Pythagoran relationships depending on the current slip velocities in longitudinal and lateral directions:

$$sAdhesion = \sqrt{\left(sAdhesionLong\frac{v_{slip,Long}}{v_{slip}}\right)^2 + \left(sAdhesionLat\frac{v_{slip,Lat}}{v_{slip}}\right)^2} \tag{3.3}$$

$$sSlide = \sqrt{\left(sSlideLong\frac{v_{slip,Long}}{v_{slip}}\right)^2 + \left(sSlideLat\frac{v_{slip,Lat}}{v_{slip}}\right)^2} \tag{3.4}$$

$$muMax = \sqrt{\left(muMaxLong\frac{v_{slip,Long}}{v_{slip}}\right)^2 + \left(muMaxLat\frac{v_{slip,Lat}}{v_{slip}}\right)^2} \tag{3.5}$$

$$muMin = \sqrt{\left(muMinLong\frac{v_{slip,Long}}{v_{slip}}\right)^2 + \left(muMinLat\frac{v_{slip,Lat}}{v_{slip}}\right)^2} \tag{3.6}$$

A function $\mu_s = f\left(muMax, muMin, sAdhesion, sSlide, v_{slip}\right)$ is defined with these coefficients as an interpolation of three different conditions: full adhesion, mixed adhesion and sliding, full sliding. Details can be found in [86] about the definition of this function as well as further refinements to ensure its continuity and to enhance its behavior for low velocities and low slips. Finally, the longitudinal and lateral tire

forces are calculated as

$$f_{Long} = f_n \mu_s \frac{v_{slip,Long}}{v_{slip}} \tag{3.7}$$

$$f_{Lat} = f_n \mu_s \frac{v_{slip,Lat}}{v_{slip}} \tag{3.8}$$

These forces are passed to the frame connector together with f_n. Also, the torques caused by these forces are calculated and passed over to the frame connector. Two dynamic equations of motion complete the model by putting forces, mass, and accelerations as well as torques, inertia tensor and rotational accelerations into relationship. Simple rolling resistance is considered by setting a constant rolling friction coefficient and multiplying it by the vertical load. The special case of rolling resistance in the vicinity of zero rotational speed is treated separately (see [86] for details).

3.3.3 Rolling resistance model

The tire rolling resistance is a very important aspect for the scope of this work, as it is the primary resistance influencing the performance of an Electric Taxi System. Measurements carried out by Safran MDB in the Cleansky Joint Technology Initiative - *Smart Operations on Ground* project (already mentioned in Section 2.3.2) have shown that the rolling resistance in aircraft tires sensibly depends on the rolling speed, being the breakaway resistance (i.e. starting from standstill) greater than the rolling resistance at higher speeds. Also, the breakaway resistance itself increases with the standing time. Therefore, the simple rolling resistance model based on a constant coefficient was not sufficient to reflect this behavior.

From the analysis of the measurement data carried out on an Airbus A320, the breakaway coefficient rises with an increasing positive derivative at first up to a certain standing time, then with a decreasing one until an asymptotic value is reached. As a consequence, the following function of breakaway coefficient over standing time t, expressed in minutes, has been assumed:

$$\mu_b = \mu_{b,min} + \frac{\mu_{b,max} - \mu_{b,min}}{1 + \exp\left[m_b \left(-t^{\,p_b} + a_b\right)\right]} \tag{3.9}$$

This curve is based on the so-called logistic function $f(x) = (1 + e^{-x})^{-1}$, which has a characteristic S-shape with two asymptotes for $x \to -\infty$ and $x \to +\infty$. The tunable parameters $\mu_{b,min},\ \mu_{b,max},\ m_b,\ p_b,\ a_b$ offer five degrees of freedom for shaping the curve. The asymptotic breakaway coefficient for large standing times was known from the measurements, corresponding to the parameter $\mu_{b,max}$. The other parameters were tuned with a least-square method using measurements of breakaway coefficient for different standing times. A comparison between the tuned curve and the measurements is displayed in Figure3.5.

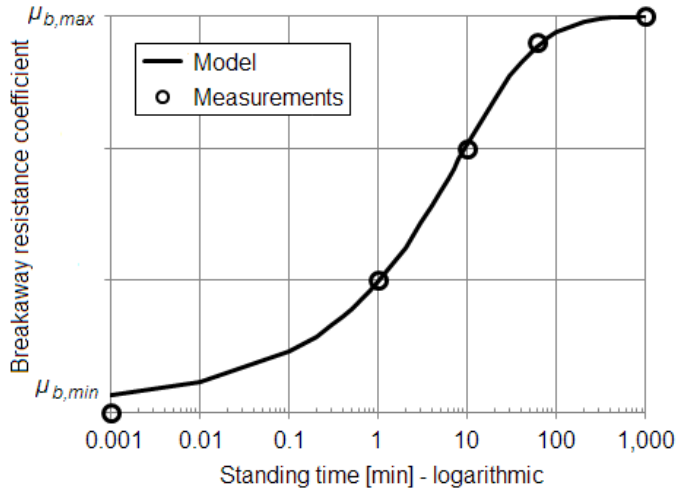

Figure 3.5: **Comparison between measurements and simulation of the tire breakaway coefficient after tuning the model function parameters**

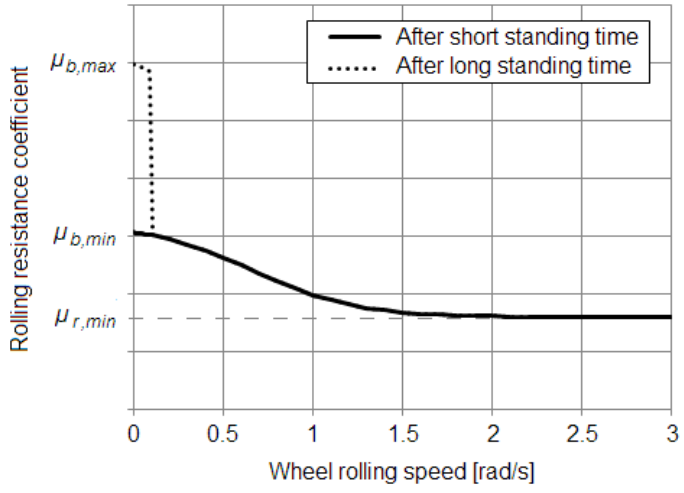

Figure 3.6: **Curve of rolling resistance coefficient as function of the wheel rolling speed after a short and a long stop**

In the tire model, a boolean variable $Stopped$ is used as flag set to true if the absolute rolling speed is below 0.1 m/s, and to false otherwise. The time elapsed since turning the $Stopped$ flag on is counted and used for the calculation of the breakaway coefficient. When $Stopped$ is turned off, the counter is reset to zero.

The rolling resistance coefficient as function of the rolling speed shows a similar S-shaped behavior, starting from the current breakaway coefficient and decreasing to an asymptotic value for increasing speeds. A function similar to (3.9) is then used for modeling the rolling resistance:

$$\mu_r = \mu_{r,min} + \frac{\mu_b - \mu_{r,min}}{1 + \exp\left(m_r \left|\omega\right| - a_r\right)} \tag{3.10}$$

with the current breakaway coefficient μ_b from (3.9), the wheel rotational speed ω, and the tunable parameters $\mu_{r,min},\ m_r,\ a_r$. The parameter $\mu_{r,min}$ corresponds to the asymptotic value of rolling resistance coefficient for high speeds. Figure 3.6 shows the behavior of this curve, after tuning its parameters with a least-square method against the available measurements, as a function of the wheel rolling speed. Two curves are depicted: the first one after a short stop, starting with the minimum value of μ_r, and the second one after an indefinitely long stop, starting with the maximum value of μ_r, which then drops to its minimum value after the speed reaches 0.1 m/s and the $Stopped$ flag is turned off. The minimum is reached asymptotically for higher speeds.

Finally, the rolling resistance torque T_{roll} is calculated as:

$$T_{roll} = \begin{cases} \mu_r f_n \dfrac{\omega}{\omega_r} & \text{if } \left|\omega\right| < \omega_r \\ \mu_r f_n \dfrac{\omega}{\left|\omega\right|} & \text{otherwise} \end{cases} \tag{3.11}$$

where ω_r is a threshold speed, chosen conveniently small, to make the expression continuous in the vicinity of zero speed.

3.3.4 Identification of tire model parameters

The parameters of the tire model determining the dynamic characteristics needed to be identified. For this purpose, data from tire measurement campaigns were made available by Safran MDB in the framework of the Cleansky Joint Technology Initiative - *Smart Operations on Ground* project already mentioned in Section 2.3.2. These data contained diagrams of the lateral force as function of the slip angle for different vertical loads for both a nose and a main gear tire of an Airbus A320, as well as diagrams of the tire elasticity in all three directions. Values of lateral force for fixed slip angles were read out from the diagrams at all available vertical loads for both nose and main gear tires and used as reference measurements for the following optimization problem.

A "tire test rig" model was realized in Modelica for the parameter identification (Figure3.7). The model uses blocks and connectors from the Modelica Multibody

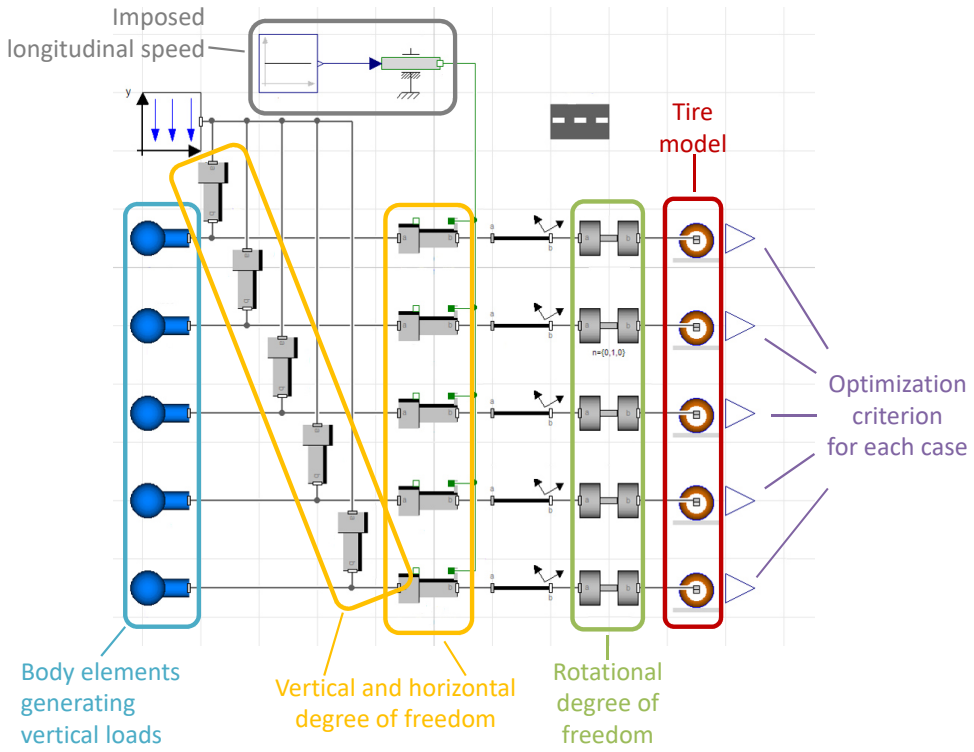

Figure 3.7: **Modelica model of tire test rig for parameter identification**

library allowing exchange of forces and torques in the three spatial directions. The model features:

- a *World* block from the *Modelica Multibody* library, declared as an *outer* model (see Section 3.2.2), defining the absolute reference system and the gravity acceleration vector;
- a *Road* block from the original *WheelDynamics* library, declared as an *outer* model and defining the position and orientation of the ground surface with respect to the absolute reference system.
- A *Speed* block from the Modelica Standard library used to move the tires with a fixed speed. It can be interpreted as a 'speed generator' applying whatever force is necessary to maintain the desired speed.

In addition, a set of the following blocks was implemented for each value of slip angle considered in the reference measurements:

- a *Body* element from the Modelica standard library where the mass generat-

ing the vertical load on the wheel is defined. The resulting vertical force is determined through the gravitation vector available in the *World* outer model;

- a *FreeTranslZ* (Free Translation Z) mechanical joint allowing the vertical degree of freedom. The gravity force acting on the Body mass will be balanced by the tire vertical stiffness only;
- an *ImprTranslX* (Impressed Translation X) mechanical joint allowing the longitudinal degree of freedom and impressing the speed transmitted by the Speed block to the elements right of it in the longitudinal direction;
- a *FixedRotationZ* kinematic rotation keeping the tire at an angle with the traveling direction equal to the slip angle considered in that set of blocks;
- a *RotationY* bearing joint freeing the rotational degree of freedom around y, thus allowing the wheel to spin freely;
- the aircraft wheel model. Masses, dimensions and other parameters are defined for either the nose or the main gear tire. The parameters pertaining to the lateral behavior (*muLatMin1*, *muLatMax1*, *muLatMin2*, *muLatMax2*, *sAdhesion1*, *sSlide1*, *sAdhesion2*, *sSlide2*, *fN1*, *fN2*) are kept in literal form as tuning variables of the optimization problem;
- a *Criterion* output for the optimization criteria.

This model is used as basis for an optimization task. The Modelica Optimization library was used for this work. It is a commercial Modelica package developed by the DLR Institute of System Dynamics and Control containing optimization tools and functions. A multi-case model optimization task was set up. With this task, a single optimization run consists of multiple simulations of the same model where some parameters are changed; the objective function for this run will include all the related simulations. In this work, multiple simulations were performed in each optimization run for all the m values of tire vertical loads used in the measurements. The objective function is calculated in each simulation as:

$$f_k(\mathbf{x}) = \sum_{\alpha=1}^{s} \left(F_{y,sim,\alpha,k}(\mathbf{x}) - F_{y,meas,\alpha,k}\right)^2 \tag{3.12}$$

where $k = 1, \ldots, m$ is the current simulation within each optimization run and $\alpha = 1, \ldots, s$ is the current slip angle among the s slip angles considered in the measurement data. The overall objective function for the optimization run is then:

$$f(\mathbf{x}) = \sum_{k=1}^{m} f_k(\mathbf{x})^2 \tag{3.13}$$

Additionally, a set of inequality constraints was provided. For each vertical load k, the average relative deviation between simulation results and measurements at all slips should not exceed a predefined limit $\delta_{max,k}$, while the maximum relative

deviation occurring at a certain slip should not exceed $2 \cdot \delta_{max,k}$. This relative deviation is defined for each slip angle s and each vertical load k as:

$$\delta_{s,k} = \frac{|F_{y,sim,s,k}(\mathbf{x}) - F_{y,meas,s,k}|}{F_{y,meas,s,k}} \tag{3.14}$$

The limits $\delta_{max,k}$ were taken lower for vertical loads near the normal operating conditions. The rationale of this constraint is that the model should be more precise when simulating operating conditions. Thus parameter sets yielding a good objective function, but leading to excessive deviations in operating conditions should be rejected. Other inequality constraints are limits on the parameter ranges. For instance, the friction coefficients and slip velocities should be strictly positive.

The Pattern Search algorithm was used for this optimization with error tolerance 10^{-3} and 1,000 iterations. A graphic comparison of the lateral force measurements and the model predictions with the optimized parameters is shown in figures 3.8 and 3.9. It can be seen that the optimized model is remarkably precise in simulating the lateral behavior of a real tire. Lack of data prevented optimizing the parameters for the longitudinal behavior, therefore the precision of the model could not be assessed. Parameters from similar car tire models were taken instead.

3.3.5 Model parametrization

As illustrated in the above sections, the behavior of the wheel model is based on a number of parameters that can be very different for each aircraft type. When using the wheel model, a list of parameters needs to be specified, including mass, moment of inertia, dimensions, essential model parameters mentioned in Section 3.3.2 such as friction coefficients and slip velocities. Some *records* have been included into the library for this purpose. In Modelica, records are components containing a set of data that will be assigned to a model as parameters. Records have been realized for different aircraft architectures, for nose gears and main gears, and for different levels of ground grip. One of these records can be specified in the property window of each wheel model. In alternative to this, it is possible to set and modify the parameters individually in the different tabs of the wheel model property window.

3.4 Landing Gear Model

The landing gear model essentially transmits forces and torques generated at tire level to the aircraft body model. Additionally, it includes models of components that are relevant for controlling the ground motion. In the following, the model variants that have been realized will be shown. A schematic illustration of the wheel assemblies used in the landing gear models is given in Figure3.10. The variants of landing gear models are shown schematically in Figure3.11.

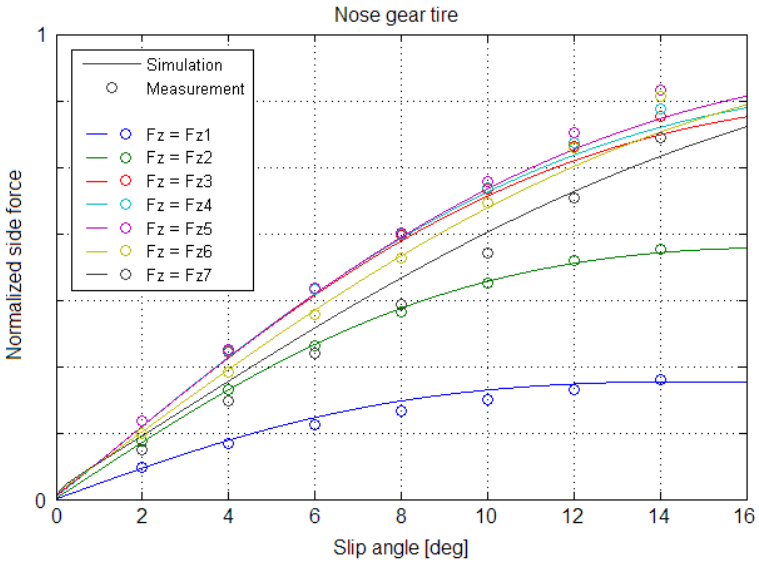

Figure 3.8: **Comparison between measurements and simulation of cornering force vs. slip angle for nose gear tire after optimizing the model parameters**

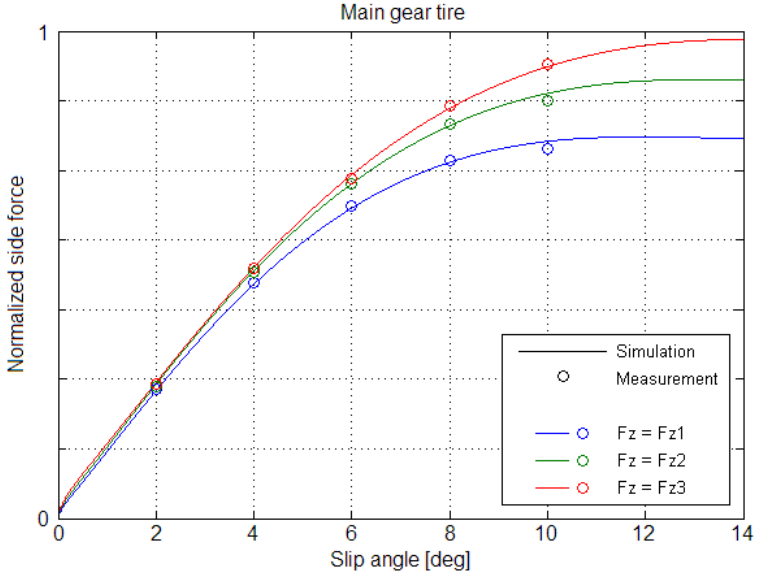

Figure 3.9: **Comparison between measurements and simulation of cornering force vs. slip angle for main gear tire after optimizing the model parameters**

3.4.1 Main landing gear model

This model, intended for narrow body aircraft, contains the following components:

Landing gear model frame This multibody connector from the Modelica Multibody library (see Section 3.2.1) permits to link the landing gear model to the aircraft body model and to transmit forces and torques.

Landing Gear Bus connector and Kinematics connector These two connectors contain subsets of the variables stored in the Bus connector from the Flight Dynamics library (see Section 3.2.2) that links the aircraft components.

Wheel models Two occurrences of the tire model illustrated in Chapter 3.3 representing the two wheels per each landing gear. Links to the Kinematics connector provide the current latitude and longitude needed for calculating the current normal vector and distance of the ground surface.

Wheel bearing models Two occurrences of *Revolute* joint from the Modelica MultiBody library, allowing the rotational degree of freedom around the y-axis of the wheel.

Brake models Two occurrences of *Brake* model from the Modelica Standard library. The model has two rotational flanges that are linked to the two ends of the wheel bearing. The braking torque in Nm commanded at its input port via the Landing Gear Bus connector will be applied to both flanges. The model handles the frictional behavior at zero speeds appropriately, keeping the wheel bearing locked while the external torques are smaller than the braking torque.

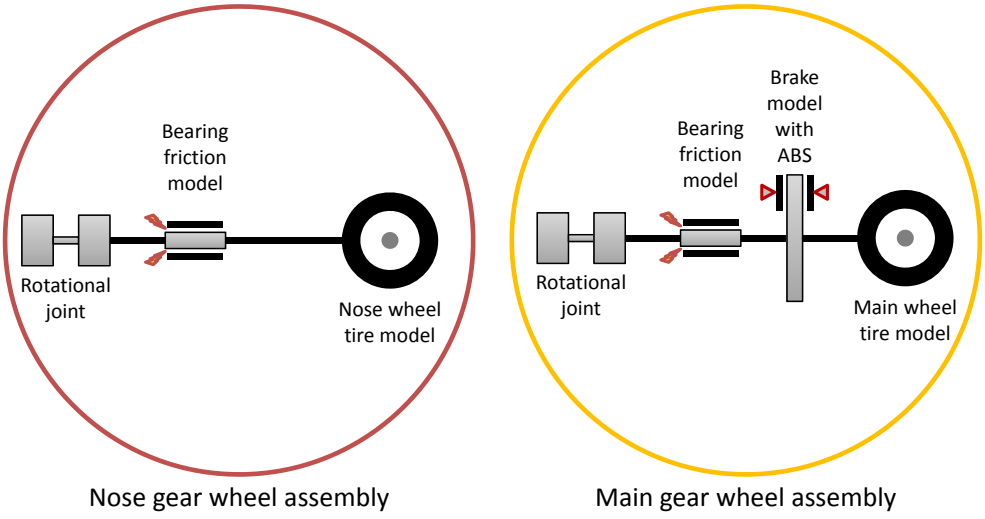

Figure 3.10: **Wheel assembly models for nose gear and main gear**

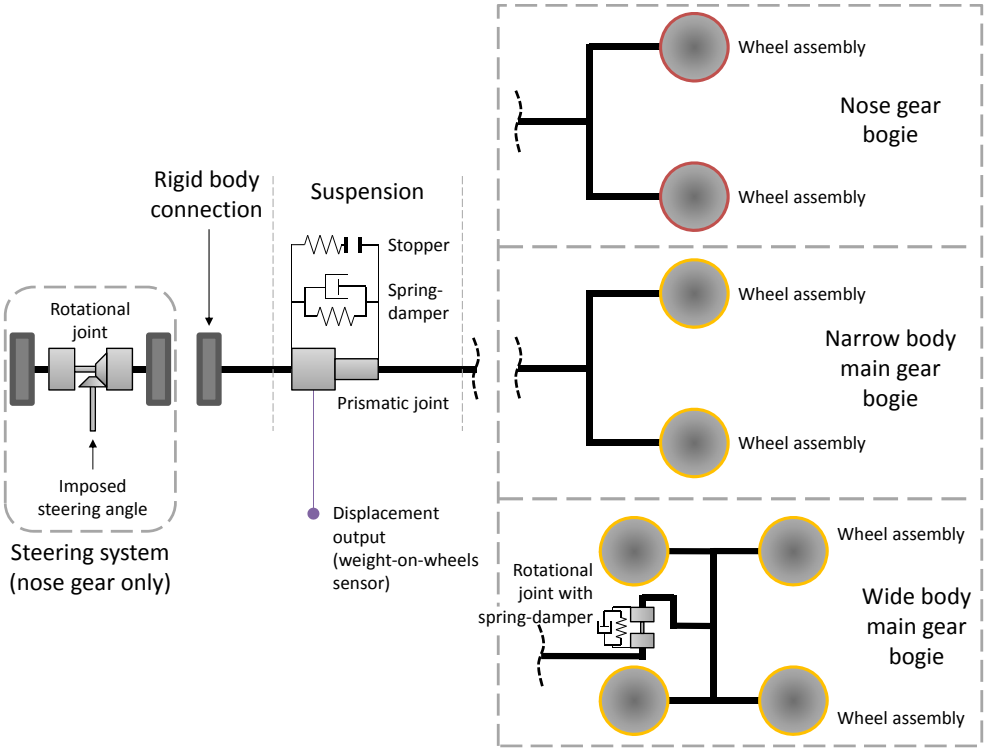

Figure 3.11: **Schematic landing gear models. The three variants illustrated (nose gear, narrow body main gear, wide body main gear) differ in the presence of the steering system, the structure of the bogie, the disposition of the wheels and the wheel assembly model used (see Figure3.10).**

Bearing friction models One such model from the Modelica Standard library is attached to the brake model flange. The bearing rotational friction is modeled as a constant resisting torque (always opposed to the wheel direction of rotation) with estimated values provided by industrial partners.

Fixed translation models They link the bearings to the gear strut/suspension assembly and position them at the appropriate distance in the lateral direction with regard to the gear vertical axis, thus representing the landing gear horizontal structure. Their mass is neglected in the model. In the general case, the wheels will be in a symmetric position, therefore the Fixed Translation elements will be equal.

Gear strut and suspension assembly It features a *Prismatic* joint from the Modelica Multibody library, allowing the vertical degree of freedom, and a spring and damper assembly component representing the gear suspension and shock absorber. Additionally, a *Suspension Dead Stop* block limits the suspension travel. It is an additional spring-damper element with very high stiffness that intervenes only above a certain suspension travel, thus modeling the impulse on the suspension structure reaching its mechanical travel limit.

Weight-on-wheels sensor It features a block measuring the force in vertical direction between gear model frame and strut assembly, and a logic block emitting a "true" boolean output if the force is a compression force, "false" otherwise. This output is uploaded onto the Landing Gear Bus connector.

Although this work focuses on narrow-body aircraft, landing gear models for wide-body aircraft were built too to illustrate the modularity capabilities of Modelica. Main landing gears of wide-body aircraft usually have four wheels. The model features four model assemblies including wheel, bearing, brake, and bearing friction model, as described in Section 3.4.1. These assemblies are linked to the gear center through *Fixed Translation* elements, positioning them at the symmetrical ends of a H-shaped gear bogie structure. A rotational joint with a spring-damper model in parallel allow the rotation of the bogie around the lateral axis with respect to the gear strut. As in the narrow-body main gear model, a suspension model and a weight-on-wheels sensor are present representing the gear strut, and the interfaces with the outside models are a frame connector, a Kinematic Bus connector, and a Landing Gear Bus connector.

3.4.2 Main landing gear model with anti-skid system

The importance of anti-lock braking systems (usually referred to as anti-skid systems in aviation) for safe and efficient landing has been recognized early in aviation history. First mechanical anti-skid systems such as the Maxaret brake unit [1] started to be adopted on a large scale as early as in the Fifties of the 20th century. Today, virtually all commercial aircraft and most general aviation jets are equipped with an anti-skid system. This feature needs to be modeled too in order to have representative landing

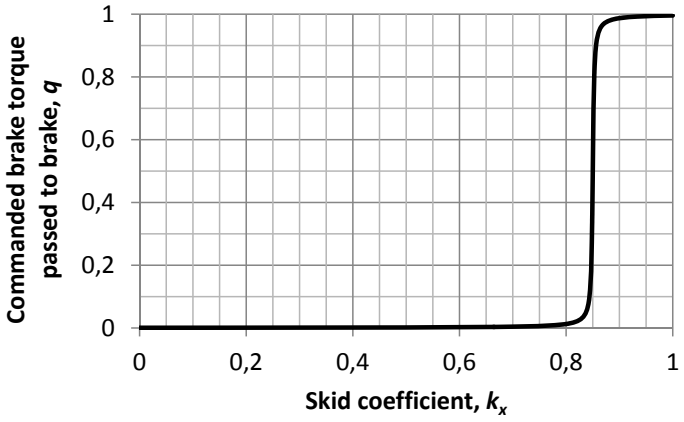

Figure 3.12: **Diagram of brake torque reduction as function of the skid coefficient k used in the anti-skid system model**

gear models.

A brake command regulator model was realized that represent the functionality of an anti-skid system. The inputs are the current ground speed v_G in the aircraft body longitudinal direction, the longitudinal slip velocity $v_{slip,Long}$, and the braking torque t_{bc} commanded by the pilot. The skid coefficient k_x is calculated as

$$k_x = 1 - \frac{v_{slip,Long}}{v_G} \tag{3.15}$$

This coefficient is 1 if the wheel is rolling freely on the ground and 0 if the wheel is completely locked. Next, the braking torque actually passed to the brake model is determined by multiplying the pilot commanded brake torque with the following arctangent function:

$$q = \frac{1}{2} + \frac{1}{\pi} \arctan\left[500\left(k_x - 0.85\right)\right] \tag{3.16}$$

This function varies between 0 and 1 very steeply in the vicinity of the skid coefficient $k_x = 0.85$ (see Figure3.12), effectively resulting in a feedback control of the wheel rotational speed. The values 0 and 1 are reached asymptotically. This means that the braking torque is never passed through unchanged when no anti-skid intervention occurs, and is never set to zero when the anti-skid system intervenes. However, the related error is negligible since $q > 0.99$ for $k_x > 0.914$ and $q < 0.01$ for $k_x < 0.786$. The advantage of using this continuous function is that conditional statements are not needed to limit the amount of brake torque reduction between 0 and 1, which results in a simpler code and better computational efficiency due to the absence of discontinuities.

One instance of anti-skid system model is needed for each wheel within a main landing gear model. The longitudinal slip velocity is taken from the appropriate

output of the wheel model, and the ground speed is taken from the Kinematic Bus connector.

3.4.3 Nose landing gear model

On most aircraft, the nose landing gear features two wheels aligned along the same rotational axis; it can rotate around its vertical axis for steering and it does not have brakes. Therefore, only one variant of generic nose gear model was realized. The nose landing gear model (see Figure3.11) differs from the main landing gear models in that brake models are not present. Furthermore, a rotational joint around the vertical axis and an *impressed position* block are added between the body frame and the suspension assembly. The commanded steering angle is taken from the Landing Gear bus connector and assigned to the rotational joint. Other components are analogous to the main gear model, whereas the dimensions of the structural blocks and the parameters of the wheel models and the suspension model reflect those of a nose gear.

4 Electric Taxi System Modeling

As mentioned in Chapter 1, the assessment methodology presented in this thesis uses an integrated model including aircraft and system models. Specific to the concrete example illustrated in this thesis, an Electric Taxi System model is described in this chapter. This model will be linked with the aircraft model presented in Chapter 3 to perform the simulation-based assessment.

The models of the ETS and its power supply should be able to reproduce the motion dynamics, the torque response and the power demand variation appropriately at aircraft level, whereas secondary phenomena largely completing their effects in a time scale under 1 second, such as electromagnetic effects, are not relevant. When using the proposed approach to compare different system architectures and sizes, scalable motor models may be needed. However, highly accurate models including secondary phenomena can be required for the study of the thermal behavior. Since no real systems were investigated in this work, but a virtual system has been assumed, a simplified thermal model has been built as an example to show the potential of the proposed approach.

4.1 System Architecture Chosen

The choice of an ETS architecture involves the *a priori* determination of three features: the arrangement of the system on the aircraft, the characteristics of the driveline, and the power source. A description of possible architectures of on-board electric taxi systems was given in Section 2.3.2; also, current system prototypes were cited. Based on this information, the diagrams in Figure 4.1 compare the different possible choices for the three aspects mentioned.

Considering this comparison and after reviewing the existing ETS demonstrators and prototypes, a system architecture with two direct-drive motors fitted in the main gear has been chosen in this work, as displayed in Figure 4.2. This architecture shows some advantages over other choices, notably a better traction due to the higher vertical load on the main gear, and a simpler and lighter driveline without gearbox. Conversely, the integration into the main gear assembly and the engineering of high-torque, direct-drive motors capable to withstand high take-off and landing speeds are challenges to be faced.

The two electric motors drive the external wheel of each main landing gear; the

System arrangement

1 or 2 motors in nose gear	*Motor drives in main gear*
✓ Easier integration (no brakes) × Low traction due to low vertical load × Heavy redesign possibly required (strength, shimmy behavior, strut inclination) × Low redundancy if only one motor is installed	✓ Good traction due to high vertical load ✓ Robust structure can accommodate system more easily × Integration issues (brakes)

2 motors in main gear	*4 motors in main gear*
✓ Less complexity ? One larger motor per gear (integration?)	✓ Redundancy ? Two smaller motors per gear (integration?) × More complexity

Motor drive characteristics

Direct drive	*Drive + clutch and gearbox*
✓ Higher reliability ✓ No additional gearbox weight × Heavier, more complex high-torque motors × Must withstand high speeds during take-off and landing	✓ Lighter motors × Additional gearbox weight × Difficult integration of motor + gearbox into wheel rim × Lower reliability

Figure 4.1: **Comparison of ETS architecture variants**

motors are directly connected to the wheels without any gearbox or clutch in between. The APU is used as power supply via a dedicated AC generator linked to the APU gearbox. The regulation of each motor is performed through AC/AC power electronic converters. Electric braking is possible with the motors working as generators, but no additional devices for using or storing the generated power have been considered concretely here for the sake of simplicity. In reality, the generated power must be fed to such a device, which will increase the system weight and complexity, or otherwise used by other electrical loads thus partially relieving the APU from power generation. This may be possible in principle, but it requires an interface to the aircraft electrical system and a load management system. The ETS is not subject to power limitations at any time. An APU load management system is assumed to monitor the power requests from the other aircraft systems and to limit or disconnect them as needed to guarantee the maximum priority to the ETS system.

A model of such a system has been realized in Modelica. The system model is scalable by means of a scaling parameter. This allows to simulate a family of ETS and

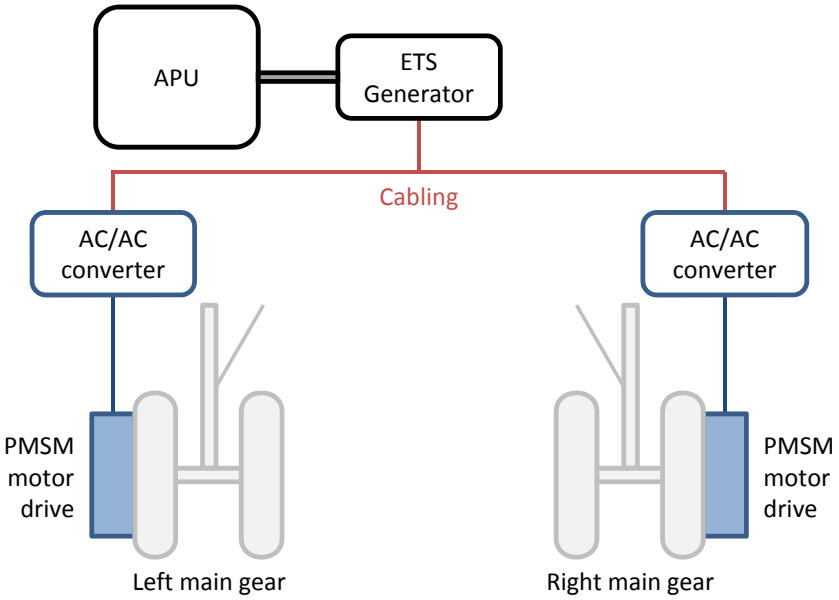

Figure 4.2: **ETS architecture considered in this work**

compare their performances, as will be done in Chapter 7.

4.2 Electro-mechanic Motor Model

The electric machine is the primary component of the taxi system. Among the various electric motor types, a Permanent Magnet Synchronous Machine (PMSM) has been chosen in this work to realize the electric motor model. Compared to other types of motor with external excitation, the PMSM is known to show greater efficiency, higher torque density, higher power density, and easier construction and maintenance [36]. These advantages make this technology particularly attractive for this application.

Considering the purpose and focus of this work, a functional motor model is needed to simulate the relationship between the inputs from the electric network and the dynamic mechanical outputs at aircraft level. High-frequency effects and electromagnetic phenomena within the machine or the electric network that impact the motor dynamic mechanical behavior only marginally are neglected. A detailed discussion and modeling of the electric machine is therefore outside of the scope of the work. For the functional model needed, it is sufficient to recall the working principle of a synchronous machine: a rotating magnetic field is created by sinusoidal currents flowing in the stator windings with appropriate phase shifting between each

other. In a synchronous machine, the rotating magnetic field must be aligned with the permanent magnet rotor field at all times. Therefore, field-oriented control is normally used with PMSM [24]. It involves introducing a *d-q* rotating reference system with the *direct axis* parallel to the rotor magnetic field and the *quadrature axis* perpendicular to it. The voltage and current phasors are then expressed with their components along the $d-q$ axes and are linked by the following relationships [24]:

$$\begin{cases} v_d &= R_s i_d + L_s \dot{i}_d - p\omega L_s i_q \\ v_q &= R_s i_q + L_s \dot{i}_q + p\omega L_s i_d + \psi_{PM} p\,\omega \end{cases} \tag{4.1}$$

where i_d, i_q are the current phasor components in direct respectively quadrature axis, v_d, v_q are the voltage phasor components in direct respectively quadrature axis, R_s is the resistance of one stator phase, L_s is the inductance of one stator phase (kept equal for direct and quadrature axis by assuming a saliency ratio of 1), p is the number of magnetic pole pairs, ω is the rotor speed, ψ_{PM} is the magnetic flux of the permanent magnets. The expression for the mechanical torque T generated by this machine — not considering any magnetic saturation effect — is:

$$T = \frac{3}{2} p\,\psi_{PM}\,i_q \tag{4.2}$$

Finally, the mechanical power P_m and electrical power P_e are determined by:

$$P_m = T\omega = \frac{3}{2} p\,\omega\,\psi_{PM}\,i_q \tag{4.3}$$

$$P_e = \frac{3}{2}\left(i_d v_d + i_q v_q\right) \tag{4.4}$$

Within this motor model, P_e and P_m only differ by the resistive losses; other kinds of losses were not considered for simplicity.

The design parameters of the reference (non-scaled) machine were chosen on the basis of real PMSM machines such as the one developed in [59] and are given in Table 4.1.

4.3 Control Strategy of the Electric Motors

Equation (4.2) shows that the torque is a strictly linear function of the quadrature current i_q for this machine model. The strategy followed in this work for controlling the machine output is then to regulate the quadrature current i_q while keeping i_d zero at all times. The reason for $i_d = 0$ will be explained below.

The modulus of i_q must remain below the rated maximum peak current per phase $\hat{I}$, which results in a rated maximum torque $\hat{T}$ after substituting in (4.2). Moreover, a rated maximum mechanical power $\hat{P}_m$ is set for the motor. When generating the rated

Parameter	Symbol	Value
Rated torque	$\hat{T}_0$	8250 Nm
Rated mechanical power	$\hat{P}_{m0}$	75 kW
Rated peak current per phase	$\hat{I}_0$	275 A
Resistance per phase	R_{s0}	0.225 Ω
Inductance per phase	L_{s0}	$4 \cdot 10^{-3}$ H
Permanent magnet flux	ψ_{PM0}	1 Wb
Number of pole pairs	p	20
Rotor inertia coefficient		2.11 kg · m^2

Table 4.1: **Design parameters of the reference machine for ETS**

torque $\hat{T}$, $\hat{P}_m$ is reached at the rated speed $\hat{\omega}$. Transposing (4.3) and using the rated quantities introduced, the rated speed is calculated as:

$$\hat{\omega} = \frac{\hat{P}_m}{\hat{T}} = \frac{2}{3}\frac{\hat{P}_m}{p\,\psi_{PM}\hat{I}} \tag{4.5}$$

At the rated current and speed, the rated peak voltage per phase $\hat{V}$ results from the composition of the direct and quadrature voltages calculated in this steady-state working point. Substituting $i_d, \dot{i}_d = 0,\ i_q = \hat{I},\ \dot{i}_q = 0,\ \omega = \hat{\omega}$ into (4.1):

$$\hat{v}_d = -p\hat{\omega}L_s\hat{I} \tag{4.6}$$

$$\hat{v}_q = R_s\hat{I} + \psi_{PM}p\hat{\omega} \tag{4.7}$$

$$\hat{V} = \sqrt{\hat{v}_d^2 + \hat{v}_q^2} \tag{4.8}$$

In a real system, it has to be checked whether this voltage constitutes a technical limitation. If $\hat{V}$ cannot be exceeded, then the machine can only be operated at speeds beyond the rated speed by applying *flux weakening*. This method involves setting an appropriate direct current $i_d \neq 0$ to keep the voltage of the machine in an allowed range. In the common *constant voltage, constant power* strategy [50], i_d and i_q are chosen such that $v_d = \hat{v}_d$ and $v_q = \hat{v}_q$ for $|\omega| > \hat{\omega}$. The effect of $i_d \neq 0$ on v_q in (4.1) is to counterbalance the back-electromagnetic force term $\psi_{PM}p\,\omega$ so as to prevent the further increase of v_q with rising ω. With increasing i_d and because the electrical power P_e is also kept constant at the rated value $\hat{P}_e$, it follows from (4.4) that the maximum limit on i_q must be reduced proportionally to the increase of i_d. It can be inferred from (4.2) that this results in a torque reduction with increasing speed.

For reasons of simplicity, this work assumes that no significant voltage limits exist that would require the use of flux weakening techniques within the operating range of the ETS. Therefore, i_d is kept zero at all times. As for i_q, a limit on the mechanical power $P_m \leq \hat{P}_m$ is set. Above the rated speed, the limit on i_q must be reduced further

than $\hat{I}$ to ensure that the mechanical power remains in the allowed range. Considering the rated current limit and transposing (4.3) for i_q, the following general limitation results then for i_q:

$$|i_q| \leq \begin{cases} \hat{I} & |\omega| \leq \hat{\omega} \\ \frac{2}{3} \frac{\hat{P}_m}{p\omega\psi_{PM}} & |\omega| > \hat{\omega} \end{cases} \tag{4.9}$$

The motor model was realized in Modelica by coding the motor equations directly and adding a rotational inertia representing the rotor. A *rotational connector* from the Modelica Standard Library was added to permit a link to the landing gear wheel. This connector sets appropriate equations for the rotational speed and torque of the two elements linked, thus representing a rigid connection between the two elements.

4.4 Motor Scaling

The geometric scaling of the motor is performed in this work through the variation of the axial length of the machine core. Beside resulting in simpler equations, axial scaling is presumed to be easier to perform on real systems than radial scaling which is more strictly limited by the size of other components such as the inner radius of the wheel rim. This means that the cross section and the number of pole pairs remain constant, while the stator, the rotor and the magnets are varied in length by the same ratio. A sizing parameter λ_A is defined as follows:

$$\lambda_A = \frac{l_A}{l_{A0}} \tag{4.10}$$

where l_A is the axial length of the scaled machine and l_{A0} is the axial length of the reference machine, taken 250 mm. Due to the size variation of the coils and the magnets, the following quantities of the scaled machine are also influenced by λ_A linearly, if the contribution of the end windings is neglected [75]:

$$R_s = \lambda_A R_{s0} \tag{4.11}$$
$$L_s = \lambda_A L_{s0} \tag{4.12}$$
$$\psi_{PM} = \lambda_A \psi_{PM0} \tag{4.13}$$
$$\hat{T} = \lambda_A \hat{T}_0 \tag{4.14}$$

where the subscripts 0 denote the respective quantities of the reference machine (with $\lambda_A = 1$). The rated peak current per phase $\hat{I}_0$ of the reference machine is kept equal between scaled machines. Also, the rated mechanical power $\hat{P}_m$ is kept constant at the mechanical power $\hat{P}_{m0}$ of the reference machine when scaling, since the APU supply already sets a power limitation. Moreover, a higher power would only have marginal effects on the dynamic behavior of the aircraft, whereas the key factor in this

application is the maximum torque influencing the acceleration. Following from (4.3) and (4.14), this implies that the rated speed varies too between different machines:

$$\hat{\omega} = \frac{\hat{P}_{m0}}{\hat{T}} = \frac{\hat{P}_{m0}}{\lambda_A \hat{T}_0} = \frac{\hat{\omega}_0}{\lambda_A} \tag{4.15}$$

with $\hat{\omega}_0$ rated speed of the reference machine.

4.5 Thermal Model of Electric Motors

Taking the thermal behavior of the electric motors into account is key in order to ensure safe and prolonged operation. As the green taxi application requires compact high-torque motors in a difficult environment, waste heat dissipation may be challenging. Critical temperatures need monitoring during operation to avoid possible overheating issues.

Thorough thermal analysis must be performed when designing the motor; methods include analytical lumped-parameter thermal-network analysis and numerical analysis through finite element modeling (FEM) [17]. To stay within the scope of this thesis, a simplified thermal motor model will be introduced here. Upon system assessment (Chapter 7), it will serve the purpose of showing that the thermal behavior is critical for the choice of the best system architecture, type and size as it can limit the operating envelope and in turn influence the assessment result.

The stator is modeled as a hollow cylinder with outer radius r_{so}, inner radius r_{si}, and axial length l_A, featuring a number of slots filled with copper windings (see Figure 4.3). The copper wires in each slot are modeled as an homogeneous amount of copper filling the slots with an appropriate fill factor. An insulation layer is present between the copper mass of each slot and the steel mass of the stator. In a thermal circuit representation (see Figure 4.4), the copper mass of all slots and the steel mass of the rest of the stator are subsumed in two singular points with homogeneous temperatures θ_{coil} and θ_{stator} respectively. The heat capacity of the two masses is known through the geometry of the simplified stator and the density and specific heat of the materials. The heat is generated in the copper mass by the resistive losses in the windings. Other losses such as iron losses, end winding losses, and mechanical losses are neglected here for simplicity, although they may contribute to a substantial share of the total losses in reality. The heating power $\dot{Q}$ due to resistive losses is given by [43, p. 103]:

$$\dot{Q} = 3R_s I_{RMS}^2 = 3R_s \frac{\hat{I}^2}{2} \tag{4.16}$$

where I_{RMS} is the root mean square current per phase, which is equal to $\hat{I}/\sqrt{2}$ for sinusoidal currents as assumed here. The copper mass exchanges heat with the stator steel mass by conduction through the insulation layer in the slots. This is realized in

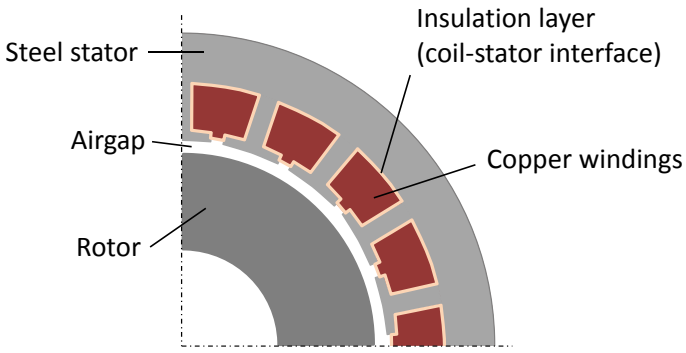

Figure 4.3: **Section of the ETS motor used for thermal modeling**

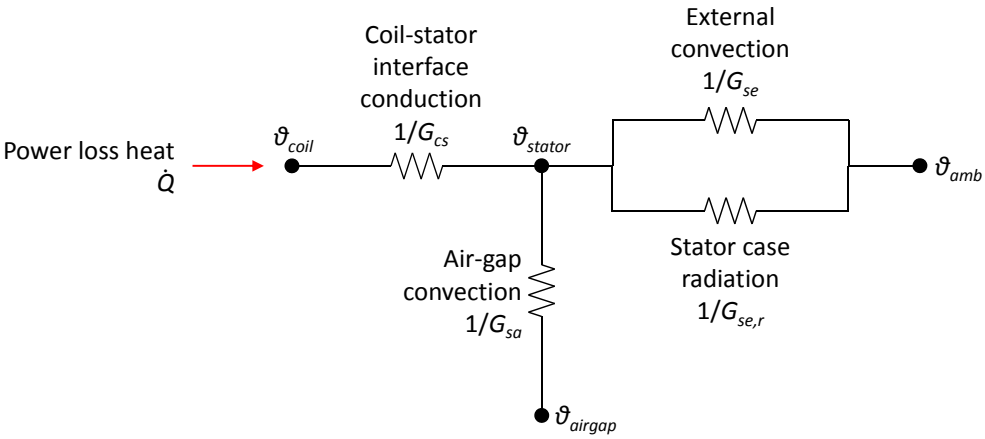

Figure 4.4: **Thermal model of the ETS motor stator represented as resistance circuit**

Table 4.2: **Geometry of simplified stator and other parameters used in thermal ETS motor model**

Parameter	Symbol	Value
Outer stator radius	r_{so}	230 mm
Inner stator radius	r_{si}	200 mm
Depth of winding slots	-	10 mm
Slot width to tooth width ratio, measured at half of the slot depth	-	1
Perimeter-to-width ratio of each slot	-	5
Airgap thickness,	t_{airgap}	5 mm
Winding insulation thickness	t_{mica}	2 mm
Thermal conductivity of insulation	k_{mica}	0.27 W/(m · K)
Resulting steel mass	-	67.78 kg
Resulting copper mass	-	22.594 kg
Specific heat of steel	-	420 J/(kg · K)
Specific heat of copper	-	383 J/(kg · K)
Ambient temperature	θ_{amb}	30 °C

mica, a mineral with excellent insulating properties commonly used in heavy-duty electric applications [76]. The thermal conductance G_{cs} between windings and stator is then:

$$G_{cs} = k_{mica} \frac{S_{mica}}{t_{mica}} \tag{4.17}$$

where t_{mica} is the insulation thickness and S_{mica} is the insulation surface, given by the perimeter of the insulation in all slots of one stator section multiplied by the machine length l_A. The parameters used are listed in Table 4.2.

The stator in turn exchanges heat with the environment through natural convection and radiation on the external surface, and through forced convection in the airgap between stator and rotor assuming a cooling fan is present. The rotor and its influence on the thermal behavior were neglected.

The following relationship approximates the thermal resistance R_{se} for the external natural convection based on experimental data on a family of motors [16]:

$$R_{se} = 0.167\ S_{so}^{-1.039} \tag{4.18}$$

where $S_{so} = 2\pi r_{so} l_A$ is the stator outer surface in accordance with the simplified cylinder model used. Because the ETS motor is fitted within the rim of the landing gear wheel, the natural airflow may be somewhat impeded. For this reason, the above thermal resistance was doubled to add conservativeness. The following thermal conductance due to external convection G_{se} was therefore used:

$$G_{se} = \frac{1}{2R_{se}} = \frac{1}{2 \cdot 0.167\ S_{so}^{-1.039}} \tag{4.19}$$

For the radiation, an emissivity $\epsilon_{stator} = 0.85$ was assumed for a varnished external stator surface, based upon the data reported in [44, p. 105] and choosing a slightly smaller value for conservativeness. The thermal conductance $G_{se,r}$ due to radiation was then calculated as:

$$G_{se,r} = S_{so}\, \epsilon_{stator}\, C_s\, \frac{\theta_{stator}^4 - \theta_{amb}^4}{\theta_{stator} - \theta_{amb}} \tag{4.20}$$

where C_s is the Stefan-Boltzmann constant and θ_{amb} is the ambient temperature (see Table 4.2). Here, it was assumed that the surface of the external environment absorbing the radiation is much larger than the stator surface, which makes the emissivity of the environment negligible [44, p. 105].

As for the airgap convection, the following relationships from [74] have been used. Firstly, the Taylor number is calculated to assess the nature of the airgap flow:

$$\mathrm{Ta} = \mathrm{Re}\sqrt{\frac{t_{airgap}}{r_{si} - t_{airgap}}} \tag{4.21}$$

where $\mathrm{Re} = t_{airgap} \cdot v_{airgap} \cdot \rho_{air}/\mu_{air}$ is the Reynolds number of the airgap flow using the air parameters reported in Table 4.3. As Ta is found to be greater than 100, the airgap flow is turbulent. The following equation then applies for the Nusselt number of the airgap flow:

$$\mathrm{Nu} = 0.386\ \mathrm{Ta}^{0.5}\ \mathrm{Pr}^{0.27} \tag{4.22}$$

where Pr is the Prantl number (see Table 4.3). With the Nusselt number, it is finally possible to calculate the convective heat transfer coefficient of the airgap h_{sa} and in turn the related thermal conductance G_{sa}:

$$h_{sa} = \mathrm{Nu}\frac{k_{air}}{t_{airgap}} \tag{4.23}$$

$$G_{sa} = h_{sa} S_{si} \tag{4.24}$$

where k_{air} is the thermal conductivity of air (see Table 4.3) and $S_{si} = 2\pi r_{si} l_A$ is the stator inner surface.

Finally, the heat transfer between the elements of the thermal model is governed by the following equations. For the heat transfer rate $\dot{Q}_{cs}$ between coil and stator:

$$\dot{Q}_{cs} = G_{cs}\,(\theta_{coil} - \theta_{stator}) \tag{4.25}$$

For the heat transfer rate $\dot{Q}_{se}$ between stator and the environment through the external surface:

$$\dot{Q}_{se} = (G_{se} + G_{se,r}) \cdot (\theta_{stator} - \theta_{amb}) \tag{4.26}$$

For the heat transfer rate $\dot{Q}_{sa}$ between stator and the environment through the airgap flow:

$$\dot{Q}_{sa} = G_{sa}\,(\theta_{stator} - \theta_{airgap}) \tag{4.27}$$

Table 4.3: **Air parameters used in convective heat transfer model. The parameters are given for a temperature of 50 °C.**

Parameter	Symbol	Value
Thermal conductivity	-	0.0285 W/(m · K)
Kinematic viscosity	μ_{air}	$1.80 \cdot 10^{-5}$ m^2/s
Prantl number	Pr	0.7
Density	ρ_{air}	1.06 kg/m^3
Specific heat at constant pressure	$c_{p,air}$	1000 J/(kg · K)
Airgap flow speed	v_{airgap}	5 m/s

Here, θ_{airgap} is the average temperature of the airgap flow. Assuming a linear temperature distribution along the airgap, θ_{airgap} is calculated as the average between the inlet temperature (ambient temperature) and the outlet temperature determined by the heat exchanged with the stator:

$$\theta_{airgap} = \theta_{amb} + \frac{1}{2} \frac{\dot{Q}_{sa}}{\rho_{air}\ c_{p,air}\ \dot{m}_{airgap}} \tag{4.28}$$

with ρ_{air} density of air, $c_{p,air}$ specific heat of air at constant pressure (see Table 4.3) and $\dot{m}_{airgap}$ airgap mass flow, calculated as:

$$\dot{m}_{airgap} = v_{airgap} \cdot \pi \left[r_{si}^2 - (r_{si} - t_{airgap})^2 \right] \tag{4.29}$$

4.6 Power Electronic Converters

The power electronic converter model performs two tasks. The first one is to control the motor as discussed in Section 4.3. This includes supplying the motor model with the appropriate i_q and with $i_d = 0$ depending on the current command input received from outside; at the same time, the current limitations in (4.9) are enforced.

The second task is to calculate the ETS power request to the APU-generator model. To this regard, the instantaneous electric motor power P_e is obtained from the motor model first. This value is increased by the power losses P_{loss}. For simplicity, these losses subsume all power losses occurring in the APU-generator system, in the cabling and in the power electronic converters. The value of P_{loss} is calculated as:

$$P_{loss} = P_{loss,0} + \gamma_1 P_e + \gamma_2 P_e^2 \tag{4.30}$$

$P_{loss,0}$, γ_1, and γ_2 are appropriate coefficients whose values used are reported in Table 4.4. The first term $P_{loss,0}$ is a constant power loss representing the power needed to supply the ETS controlling devices. The linear term represents losses in the converter

Table 4.4: **Coefficients used for the calculation of power losses in the ETS system**

Parameter	Value
Constant losses $P_{loss,0}$	50 W
Linear loss coefficient γ_1	0.02
Quadratic loss coefficient γ_2	$1.7 \cdot 10^{-6}$

semiconductors. The quadratic term represents resistive losses. The total power P_{ETS} requested to the APU-generator system is then:

$$P_{ETS} = P_e + P_{loss} \tag{4.31}$$

4.7 Model of APU and Power Generation

The power for the ETS is supplied by a dedicated generator attached to the APU. Without going into the technical details of the APU-generator assembly, the information reported in Section 2.3.2 is sufficient to build a functional APU-generator model for narrow-body aircraft suitable for the purpose of this work. A parabolic relationship between the generated APU power and the APU fuel consumption (Figure 4.5) was taken based on the data contained in [39]. Thus in each instant, the overall power P_{APU} requested to the APU (ETS, hydraulic system, bleed air, electric network) results in an instantaneous fuel flow. Because of the lack of publicly available data regarding the power request profiles of aircraft systems, the overall APU power used as input for the fuel flow calculation has been approximated as the sum of the ETS requested power and a constant power request taken 25 kW for the aircraft systems during the whole taxi profile. In addition, when the main engines are started, a constant bleed air power request of 105 kW is added for 30 s.

APU emissions of CO, HC and NO_x have been taken into account by using average emission indexes for small jet APU as measured at the Zürich airport in 2003 [4]. The emission indexes for each pollutant express the mass of pollutant emitted per mass of fuel burnt. These indexes need to be multiplied by the consumed fuel mass to obtain the produced emissions. Note that using average values implies that the motor efficiency with regard to emissions is constant over the whole operating range; in reality however, the nature and quantity of emissions strongly depends on operating conditions such as combustion temperature and pressure. More precise emission studies need to be based on detailed data for the specific APU considered.

Table 4.5 summarizes the parameters used for the APU-generator model.

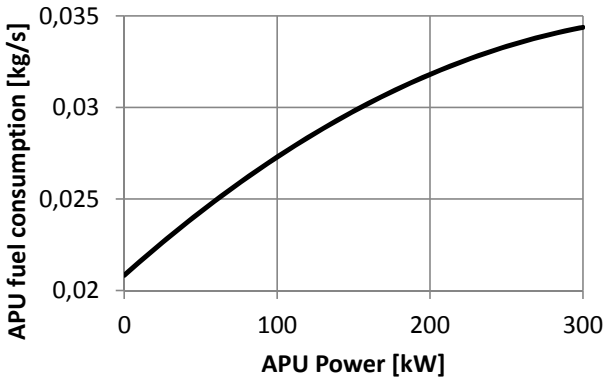

Figure 4.5: **APU fuel consumption over power**

Table 4.5: **Parameters used in the APU-generator model**

Parameter	Unit	**Value or expression**
Fuel flow	$kg \cdot s^{-1}$	$\left(75 + 0.2675 P_{APU} - 3.5 \cdot 10^{4} P_{APU}^{2}\right) / 3600$
CO emission index	$g \cdot kg^{-1}$	8.67
HC emission index	$g \cdot kg^{-1}$	0.71
NO_x emission index	$g \cdot kg^{-1}$	6.8

4.8 Weight of the ETS

The addition of the ETS onto the aircraft results in a weight increase, which in turn impacts on the mission block fuel. The weight is therefore a key driver in the assessment of the mission-level balance of the ETS technology. The weight of the main components of the ETS will be estimated in this section. The total weight of the ETS system on which this work is based is summarized in Table 4.6.

4.8.1 Motors

Estimating the weight of the motors is particularly difficult in the initial design phase of an ETS because of the large variety of motor technologies, design possibilities and parameter ranges. Also, as high torques and currents are needed for this application, particular technologies are required for which only very limited literature is available. As detailed motor design falls outside the scope of this thesis, only an approximate estimate can be given for the weight based on generic data found in the literature. In [59], a high-torque motor design was chosen for an electric taxi system among several possibilities. The best design had an active weight of 65.39 kg and a rated torque of 5,000 Nm. Based on this, a torque density of 76.46 Nm per kg of active mass is derived.

Table 4.6: **Estimated weight of the ETS system**

Component	Weight [kg]
Left gear motor	$\lambda_A \cdot 150$
Right gear motor	$\lambda_A \cdot 150$
APU power generator	78
AC/AC converters	133
Cabling	52
Miscellaneous	37
Total weight	$300 + \lambda_A \cdot 300$
Total weight for reference ETS ($\lambda_A = 1$)	600

Considering the reference data in Table 4.1, an active weight of 107.9 kg results for the reference machine by using the same torque density. This value was increased to account for the non-active parts of the machine. The overall weight of each machine in the reference size ($\lambda_A = 1$) was then set at $m_{mot0} = 150$ kg. The weight m_{mot} of the scaled machines is assumed to have a linear relationship with the sizing parameter:

$$m_{mot} = \lambda_A m_{mot0} \tag{4.32}$$

4.8.2 Power electronic converters

If an electric efficiency of the ETS motors of 75% is conservatively assumed at rated mechanical power and speed, an overall rated electric power of 200 kW results in order to generate 150 kW overall mechanical power. It follows that one 100 kW power electronic converter is needed for each ETS motor. It is assumed that the current from the generator needs to be modulated in frequency and amplitude through AC/AC converters to supply the motors. A typical value for the power density of conventional AC/AC converters used in aeronautic applications is 1.43 kg/kW = 0.7 kW/kg [20]. However, Schlabe [69] notes that the power density is strongly dependent on the adopted technology and design; also, the aeronautic industry aims to reach a power density of 8 kW/kg for AC/AC converters through innovation. Based on this, a power density of 1.5 kW/kg for the converters is set in this work assuming that a newly developed ETS can take advantage of some innovations in the field of power electronics. Since the overall electrical power with two motors is 200 kW, a total weight of $200/1.5 = 133$ kg results for the two power converters needed.

4.8.3 Power generation

The power generation for the ETS features a dedicated generator attached to the aircraft APU. This generator results in additional weight.

As mentioned in Section 4.6, the power transfer from the APU-generator to the ETS motors is subject to power losses. Using (4.30) and (4.31) with $P_e = 200$ kW assumed in Section 4.8.2, a supply system efficiency of $P_e/P_{ETS} = 0.81$ is found. Therefore, a generator power of $200/0.81 = 247$ kW is needed. A generic 225 kW APU generator of the type commonly used in narrow-body aircraft for electric supply weighs 71 kg [53]. Using the same power density, the required generator weighs then $71/225 \cdot 247 = 78$ kg.

4.8.4 Cabling

The following formula for the estimation of the cabling mass m_{cab} is given in [69]:

$$m_{cab} = 1.2\rho_{Cu} l_{cab} A_{cab} \tag{4.33}$$

where ρ_{Cu} is the density of copper (taken $\rho_{Cu} = 8920$ kg $\cdot$ m^{-3}), l_{cab} is the assumed total wire length, A_{cab} is the wire cross-sectional area, and the factor 1.2 accounts for wire insulations and other accessory mass. In the considered ETS architecture, a three-phase cable runs from the APU generator to the converters, which are assumed as located in the vicinity of the main landing gear; from there, two separate three-phase cables run to the landing gear motors. The cabling length is therefore assumed to be 50 m of three-phase cables, resulting in a total wire length $l_{cab} = 150$ m. The wire cross-sectional area A_{cab} is determined based either on the allowed current density for thermal reasons, or on the admissible voltage drop along the cable. In this work, the current density criterion was considered. The required wire cross-sectional area in this case is estimated in [69] as:

$$A_{cab} = \frac{I_{RMS}}{9 \cdot 10^6 \text{ Am}^{-2}} \tag{4.34}$$

where I_{RMS} is the rated root-mean-square current flowing in the cables. Because the cables running from the APU generator to the converters account for most of the cabling length, the electric values of the power supply are used for dimensioning. Assuming an electrical system power of 200 kW (as found in Section 4.8.2) and a 230 V 3-phase AC generator which is commonly used in aeronautical applications, a root-mean-square current per phase $I_{RMS} = 290$ A results. The cabling weight m_{cab} determined through (4.33) is thus 52 kg.

4.8.5 Other parts

The total weight of secondary ETS parts such as mountings, accessories, computers, pilot command devices, etc. is taken 37 kg.

5 Energetically Optimal Ground Path Following

In this part of the work, an optimization strategy is developed for the path following of a given assigned taxi trajectory. This strategy serves the purpose of identifying the best operational performance of a given Electric Taxi System in accordance to chosen evaluating criteria and producing a path-following profile that will be used in the mission simulation with the integrated aircraft model. This allows both direct *comparisons at ground level* between different system architectures, i.e. how different systems compare on the same taxi trajectory, and well-funded *comparisons at mission level* in that each system is used in its particular best operational conditions and specific advantages and disadvantages of the considered architecture determine the mission-level result.

The trajectory optimization problem is composed of a very large number of optimizing variables, depending on the trajectory length. Using standard optimization methods would require long computational times; also, convergence to a global optimum is not guaranteed. For this reason, convex optimization has been chosen to efficiently find the global optimum for the specific system given. Related techniques from robotic and vehicle dynamic problems are adapted to the aircraft taxi path following problem as presented in this chapter. Efficient solving tools ensure that a global optimum is found in short computational time.

Firstly, a mathematical model of the dynamics of the aircraft on ground, the Electric Taxi System and the trajectory description is written. This model is simplified in comparison to the Modelica aircraft model presented in Chapter 3, thus allowing transformation into a convex formulation. Afterwards, the convex, path-dependent optimization problem is formulated based on the mathematical model and optimizing cost functions are defined. In a further step, a convex form and an algorithm for inclusion of time constraints along the taxi trajectory are introduced and discussed. Finally, practical steps for the application of the convex path following optimization to the concrete problem are presented.

Parts of the work presented in this chapter were previously published in [64, 63] and appear here in a revised and extended form.

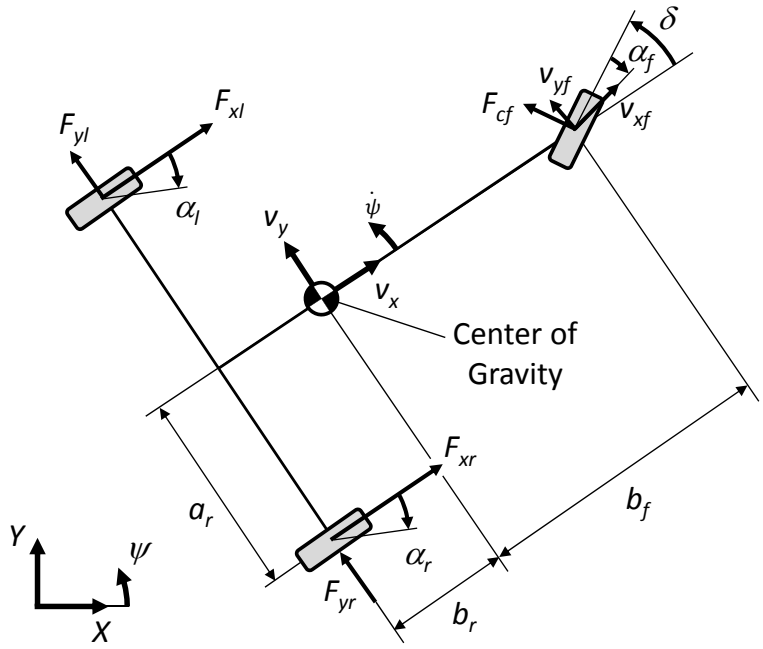

Figure 5.1: **Vehicle dynamic model used for the path following optimization problem**

5.1 Vehicle Dynamic Model

The dynamic model of the aircraft on ground is based on the vehicle depicted in Figure 5.1. Some simplifying assumptions are made to keep the problem tractable. The vehicle has three degrees of freedom: two translational degrees on the (flat) ground and the yawing rotation. Vertical dynamics as well as roll and pitch motions are neglected. Each landing gear features one wheel. One electric motor is fitted on each main landing gear for driving and slowing down; jet engines and conventional brakes are not present. The nose gear wheel can be steered and has no axial moments, i.e. it spins freely. The only resistance influencing the dynamics is the tire rolling friction, assumed constant; other sources of resistance such as aerodynamics are neglected since their contribution is relatively small at taxi speeds. Tires are assumed to have no longitudinal slip, i.e., pure rolling is assumed due to the relatively small driving forces in comparison with the vertical load in normal conditions.

The ground dynamics are described in the body-fixed reference frame with origin in the vehicle center of gravity by the following expressions for F_x (longitudinal force in

body-fixed frame), F_y (lateral force in body-fixed frame), and M_z (yawing moment):

$$
\begin{aligned}
m\left(\dot{v}_x - \dot{\psi} v_y\right) &= F_x = -F_{cf}\sin\delta + \frac{(T_l + T_r)}{R_R} - F_{res} && (5.1)\\
m\left(\dot{v}_y + \dot{\psi} v_x\right) &= F_y = F_{yl} + F_{yr} + F_{cf}\cos\delta && (5.2)\\
J_z\ddot{\psi} &= M_z = b_f F_{cf}\cos\delta + \\
&\quad + \frac{a_r\left(-T_l + T_r\right)}{R_R} - b_r\left(F_{yl} + F_{yr}\right) && (5.3)
\end{aligned}
$$

where the following symbols appear:

- v_x and v_y are the longitudinal and lateral speed in the body-fixed reference frame;
- $\dot{\psi}$ is the yaw rate;
- m and J_z are the vehicle mass and the vehicle moment of inertia around the yaw axis;
- δ is the nose gear steering angle;
- F_{cf} is the cornering force of the nose gear wheel;
- F_{yl} and F_{yr} are the lateral forces of the left respectively right main gear wheel tires;
- F_{res} subsumes all the motion resistances. As mentioned previously, only a constant rolling friction is considered here as the product of the vehicle mass multiplied by a constant rolling friction coefficient μ_R;
- T_l and T_r are the driving torques applied on the wheel of the left and right main gear respectively;
- R_R is the effective radius of each of the main gear wheels;
- a_r, b_f, and b_r are the distances between the center of gravity and the landing gears as shown in Figure 5.1;

The main gear tire lateral forces are assumed to have a linear dependence on the sideslip until reaching a constant saturation value $F_{yi,max}$ as described as follows:

$$
F_{yi} = \begin{cases} F_{yi,max}\cdot \operatorname{sign}\left(c_r\alpha_i\right) & \text{if} c_r\alpha_i \geq F_{yi,max} \\ c_r\alpha_i & \text{otherwise} \end{cases} \qquad \text{with} \quad i = \{l, r\} \qquad (5.4)
$$

where α_l, α_r are the tire sideslip angles. The same assumption holds for the front tire cornering force F_{cf} as a function of its sideslip angle α_f. The sideslip angles depend

on the vehicle kinematics as follows:

$$\begin{aligned} \alpha_f &= \delta - \arctan \frac{v_y + b_v \dot{\psi}}{v_x} \\ \alpha_l &= -\arctan \frac{v_y - b_r \dot{\psi}}{v_x - a\dot{\psi}} \\ \alpha_r &= -\arctan \frac{v_y - b_r \dot{\psi}}{v_x + a\dot{\psi}} \end{aligned} \tag{5.5}$$

The taxi path is described by the position of the vehicle center of gravity in global Cartesian coordinates X, Y as well as the vehicle course, identical to the yaw angle ψ. They are in general functions of the time:

$$\mathbf{p}(t) = [p_X(t) \quad p_Y(t) \quad p_\psi(t)] \tag{5.6}$$

By defining the vehicle course at all time instants along with the vehicle position, both v_x and v_y are known as well as the vehicle sideslip angle $\beta = \arctan(v_y/v_x)$. This implies that the left and right sideslip angles in (5.5) are also defined in advance, while the nose gear sideslip angle is defined up to addition of the steering angle δ. In the following, it is chosen to describe a trajectory such that $\beta = 0$ at all times, i.e., the vehicle longitudinal axis is always tangent to the trajectory. This condition results in $v_y = 0 \,\forall\, v_x$.

With the following transformation matrix from local (body-fixed) to global coordinates:

$$\mathbf{T}(\mathbf{p}) = \begin{bmatrix} \cos p_\psi & -\sin p_\psi & 0 \\ \sin p_\psi & \cos p_\psi & 0 \\ 0 & 0 & 1 \end{bmatrix} \tag{5.7}$$

it is possible to transform the dynamic equations (5.1), (5.2), and (5.3) to the global reference. By using the matrices:

$$\mathbf{M} = \begin{bmatrix} m & 0 & 0 \\ 0 & m & 0 \\ 0 & 0 & J_z \end{bmatrix} \qquad \mathbf{F} = \begin{bmatrix} F_x \\ F_y \\ M_z \end{bmatrix} \qquad \mathbf{R} = \begin{bmatrix} F_{res} \\ 0 \\ 0 \end{bmatrix} \tag{5.8}$$

the dynamic equation in the global frame can be written in vector form:

$$\mathbf{M}\ddot{\mathbf{p}} = \mathbf{T}(\mathbf{p})\,(\mathbf{F} - \mathbf{R}) \tag{5.9}$$

5.2 Electric Taxi System Model

The taxi drive is modeled through positive (driving) or negative (braking) torque inputs T_l, T_r applied on the left and right main gear wheel respectively. These inputs

are subject to torque limits:

$$-T_{max} \leq T_i(t) \leq T_{max} \qquad \text{with } i = \{l, r\} \tag{5.10}$$

Also, considering ideal electric motors, there is a power limit that translates into a torque limit as a hyperbolic function of the rotational speeds ω_l resp. ω_r:

$$-P_{max} \leq T_i(t)\omega_i \leq P_{max} \qquad \text{with } i = \{l, r\} \tag{5.11}$$

Concerning the thermal behavior of the electric motors, the following temperature behavior is assumed for a predefined critical point in the motor assembly (which is assumed to have been identified in advance):

$$\dot{\theta}_i(t) = k_h T_i^2(t) - k_c \left(\theta_i(t) - \theta_{amb}\right) \quad \text{with } i = l, r \tag{5.12}$$

being $\theta_i(t)$ the temperature of the critical point considered, θ_{amb} the ambient temperature, k_h and k_c constant heating resp. cooling coefficients. In other words, the heating power is taken proportional to the square of the motor torque — which is linearly proportional to the motor current in first approximation — while the cooling is considered a first-order process; further details of the cooling system are not dealt with here.

The power source of the ground propulsion system is the APU. It has been shown in Section 4.7 that the fuel consumption of an APU can be modeled by a parabolic function of the generated power. In this part of the work, that behavior is approximated by a linear function of the driving power, i.e. the positive values of T_l, T_r:

$$c = c_0 + c_1 \left[\max\{0, T_l(t)\}\omega_l(t) + \max\{0, T_r(t)\}\omega_r(t)\right] \tag{5.13}$$

where c_0 is the fuel flow at idle and c_1 is the fuel flow per each unit of requested power. Power losses are neglected. No storage system is foreseen for the energy coming from regenerative braking, which is assumed lost. In a real system, that power would be converted into waste heat in a rheostatic device.

This section and the previous one have described an integrated model of the aircraft on ground with electric taxi system which is simplified in comparison to the Modelica model of Chapter 3 and can be used directly in the convex formulation of the optimization problem, as will be shown in the next sections. This model was realized in Matlab by implementing the mathematical description in a script.

5.3 Formulation and Setup of the Optimization Problem

As stated in the introduction to this chapter, a convex optimization technique has been chosen for efficient and fast computation of the optimal path following solution. In this section, the formulation of the taxi path following problem as a convex optimization problem will be presented.

5.3.1 Convex optimization problem

An optimization problem:

$$\begin{aligned} \underset{x\in\mathbb{R}^n}{\text{minimize}} \quad & f_0(x) \\ \text{subject to} \quad & f_i(x) \leq 0 \quad \forall\, i \in [1,m] \\ & h_j(x) = 0 \quad \forall\, j \in [1,p] \end{aligned} \tag{5.14}$$

with $f_0, f_i, h_j \in \mathbb{R}$, is called a *convex optimization problem* if f_i is convex[1] $\forall\, i \in [0,m]$ and h_j is of the affine (i.e., linear) form $a_j^T x - b_j \;\forall\, j \in [1,p]$ with $a_j \in \mathbb{R}^n,\ b_j \in \mathbb{R}$. The main property — which is of interest here — of a convex optimization problem is that any local solution of the problem is also a global solution. The reader is referred to [18, p. 138] for the proof of this statement.

5.3.2 Convex equations of motion

The methodology used in the following was introduced in [84] in the context of path planning of industrial robots and was applied in [28] in a vehicle dynamics problem. The approach consists in replacing the time as independent variable with the path position s along the trajectory. Assuming $t_0 = 0$ at the start of the trajectory, the travel time t at a point s along the trajectory is:

$$\dot{s} = \frac{ds}{dt} \quad \Rightarrow \quad t = \int_s dt = \int_0^s \frac{1}{\dot{s}} ds \tag{5.15}$$

This transformation is applied to the trajectory description in (5.6), thus becoming $\mathbf{p}(s)$. Introducing the notation:

$$\mathbf{p}'(s) = \frac{d\mathbf{p}}{ds} \qquad \mathbf{p}''(s) = \frac{d^2\mathbf{p}}{ds^2}$$

the first and second time derivatives of $\mathbf{p}(s)$ can be written as:

$$\dot{\mathbf{p}}(s) = \mathbf{p}'(s)\,\dot{s} \tag{5.16}$$

$$\ddot{\mathbf{p}}(s) = \mathbf{p}''(s)\,\dot{s}^2 + \mathbf{p}'(s)\,\ddot{s} \tag{5.17}$$

The following change of variables is now introduced:

$$a(s) = \ddot{s}, \qquad b(s) = \dot{s}^2,\ b > 0 \tag{5.18}$$

[1] A function $f : X \to \mathbb{R}$ is called convex if $\forall x_1, x_2 \in X,\ \forall t \in [0,1]$ the following holds: $f(tx_1 + (1-t)x_2) \leq tf(x_1) + (1-t)f(x_2)$, or in other words, if the line segment between any two points of the function lies above the function graph drawn on an Euclidean plane.

By using the matrices:

$$\begin{aligned} \mathbf{m}(s) &= \mathbf{T}^{-1}(\mathbf{p}(s))\,\mathbf{M}\,\mathbf{p}'(s) \\ \mathbf{r}(s) &= \mathbf{T}^{-1}(\mathbf{p}(s))\,\mathbf{M}\,\mathbf{p}''(s) \end{aligned}$$

and substituting (5.17), the equation of motion (5.9) can be expressed as a system of a linear differential equation linking a and b together and an affine relationship of $a(s)$, $b(s)$, $T_l(s)$, $T_r(s)$, $F_{yf}(s)$:

$$a(s) = \frac{d\dot{s}}{dt} = \dot{s}\frac{d\dot{s}}{ds} = \frac{1}{2}\frac{d\dot{s}^2}{ds} = \frac{1}{2}\frac{db(s)}{ds} \tag{5.19}$$

$$\mathbf{m}(\mathbf{s})a(s) + \mathbf{r}(\mathbf{s})b(s) = \mathbf{F}(\mathbf{s}) - \mathbf{R} \tag{5.20}$$

5.3.3 Center of gravity forces

The center of gravity forces F_x, F_y, M_z appearing in (5.1), (5.2), and (5.3) are dependent on the tire lateral forces; these are a function of the tire side slips which in turn depend on the speeds in the local reference frame (see (5.5)). Using the transformation matrix (5.7) and the expression (5.16) for the first derivative of $\dot{\mathbf{p}}\,(s)$, the local speed vector can be written as:

$$\mathbf{v} = \begin{bmatrix} v_x \\ v_y \\ \dot{\psi} \end{bmatrix} = \mathbf{T}^{-1}(\mathbf{p}(s))\,\mathbf{p}'(s)\dot{s} \tag{5.21}$$

Introducing the symbols $L_x(s), L_y(s), L_{\dot{\psi}}(s)$ as the components of the vector $\mathbf{T}^{-1}(\mathbf{p}(s))\,\mathbf{p}'(s)$, the local speed vector becomes:

$$\mathbf{v} = \begin{bmatrix} v_x \\ v_y \\ \dot{\psi} \end{bmatrix} = \begin{bmatrix} L_x(s) \\ L_y(s) \\ L_{\dot{\psi}}(s) \end{bmatrix} \dot{s} \tag{5.22}$$

The main gear tire sideslips α_l, α_r from (5.5) can now be rewritten by substituting (5.22) as:

$$\alpha_l = \arctan\frac{L_y - b_r L_{\dot{\psi}}}{L_x - a_r L_{\dot{\psi}}}\frac{\dot{s}}{\dot{s}} = \arctan\frac{L_y(s) - b_r L_{\dot{\psi}}(s)}{L_x(s) - a_r L_{\dot{\psi}}(s)} \tag{5.23}$$

$$\alpha_r = \arctan\frac{L_y - b_r L_{\dot{\psi}}}{L_x + a_r L_{\dot{\psi}}}\frac{\dot{s}}{\dot{s}} = \arctan\frac{L_y(s) - b_r L_{\dot{\psi}}(s)}{L_x(s) + a_r L_{\dot{\psi}}(s)} \tag{5.24}$$

It is now apparent that the main gear side slip angles are only dependent on the position s along the path and are therefore known in advance once the trajectory is described. This is in connection with the fact that the trajectory description in (5.6) automatically defines the behavior of the vehicle side slip angle β in advance for every

point along the trajectory. When defining the trajectory, the main gear lateral forces can be calculated immediately for every point along the trajectory. The tire saturation limits $F_{yl,max}, F_{yr,max}$ can be taken into account by bounding the main gear lateral forces. With saturated tires, it must be possible to achieve the dynamics required by the trajectory description through other actuators (e.g. the nose gear steering or differential motor torques), otherwise the trajectory will be infeasible.

To summarize, the center of gravity forces in (5.1), (5.2), (5.3) are expressed as a function of the path as:

$$F_x = \frac{1}{R_R}\left(T_l(s) + T_r(s)\right) - F_{res} \tag{5.25}$$

$$F_y = F_{yf}(s) + F_{yl}(s) + F_{yr}(s) \tag{5.26}$$

$$M_z = b_f F_{yf}(s) + \frac{a_r\left(-T_l(s) + T_r(s)\right)}{R_R} - b_r\left(F_{yl}(s) + F_{yr}(s)\right) \tag{5.27}$$

where the variable $F_{yf} = F_{cf}\cos\delta$ has been introduced as the nose gear lateral force (along the lateral axis of the body-fixed reference) and the contribution $F_{cf}\sin\delta$ of the nose gear lateral force to the longitudinal dynamics has been assumed small, hence neglected. The center of gravity forces are affine — thus convex — functions of the main gear lateral forces $F_{yl}(s)$, $F_{yr}(s)$, known in advance as shown before, as well as the motor torques $T_l(s)$, $T_r(s)$ and the nose gear lateral force $F_{yf}(s)$. These three variables are the effects of the three actuators governing the ground motion and will be regarded as the three control variables of the problem. In the real system, the control variables are actually the actuator inputs (e.g. motor currents, steering angle). It is assumed that the knowledge of the system properties (inverse motor models, inverse nose gear tire model) allows to map the three control variables to the actuator inputs, thus permitting the use of the optimization results in a real system. As with the main gear tire forces, the nose gear lateral force F_{yf} is also limited in modulus by a maximum lateral force at saturation $F_{yf,max}$ corresponding to the maximum tire lateral force. Since safety is more important than dynamics for this application, the maximum lateral forces should be chosen with an adequate safety margin from the maximum forces actually achievable.

5.3.4 Power constraints

In this section, the equations presented in Section 5.2 will be transformed in an approximate convex form.

It is reminded that the trajectory is chosen such that the vehicle side slip angle β and in turn the lateral speed v_y are zero at all times (see Section 5.1). As a consequence, the longitudinal axis of the vehicle is always tangent to the trajectory, which results in $v_x = \dot{s} = \sqrt{b}$. In addition, the effect of the yaw motion on the rotational speed of the

main gear wheels is neglected:

$$\omega_l \approx \omega_r \approx \frac{v_x}{R_R} = \frac{\sqrt{b(s)}}{R_R} \tag{5.28}$$

After these steps, the power limit on each motor in (5.11) becomes:

$$\left| \frac{T_i(s)\sqrt{b(s)}}{R_R} \right| \leq P_{max} \quad \text{with } i = \{l, r\}$$

and observing that $b > 0$ by definition, the set of admissible motor torques due to the power limitation is:

$$|T_i(s)| \leq \frac{P_{max} R_R}{\sqrt{b(s)}} \quad \text{with } i = \{l, r\} \tag{5.29}$$

This set is not convex[2] in the variable b as can easily be seen in figure 5.2. A linear approximation of the power limitation is therefore introduced in the following inequality:

$$|T_i(s)| <= T_{max} - k_P(b(s) - b_P) \quad \text{with } i = \{l, r\} \tag{5.30}$$

While this set is convex (in fact, affine) in b, the approximation results in a non-constant power limitation; a power peak is present, then the power decreases. The position of the power peak as a function of the motor speed and the slope of the power decrease are influenced by the constants b_P and k_P. These two parameters need to be chosen carefully to keep the approximation error (visible in fig. 5.2b) small in the region of the speeds $\sqrt{b(s)}$ traveled with the real ETS.

5.3.5 Thermal constraints

The thermal equation (5.12) also becomes a function of the independent variable s by considering the time-path transformation (5.15) and reminding that $\dot{s} = \sqrt{b}$:

$$\frac{d\theta_i}{ds} = \frac{k_h T_i^2(s)}{\sqrt{b}} - \frac{1}{\sqrt{b}} k_c \left(\theta_i(s) - \theta_{amb}\right) \quad \text{with } i = \{l, r\} \tag{5.31}$$

The temperature function calculated by integrating this expression is not convex in the optimizing variables. The path integral preserves the convexity property of the argument provided that the latter is convex [18]. However, the second term in (5.31) — i.e. the cooling part — is not convex in b as is apparent by calculating its second

[2] A set S is called convex if the line segment between two arbitrary points in S lies in S completely. In mathematical terms, a set S is called convex if $\forall x_1, x_2 \in S$ and $\forall \theta \in [0, 1]$ the following holds: $\theta x_1 + (1 - \theta) x_2 \in S$.

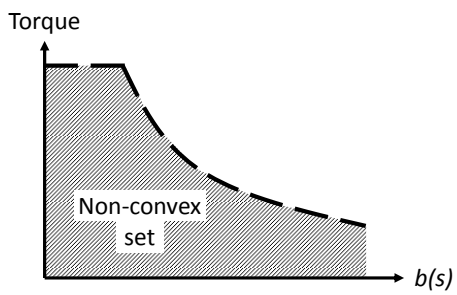

(a) **Set delimited by** (5.29)

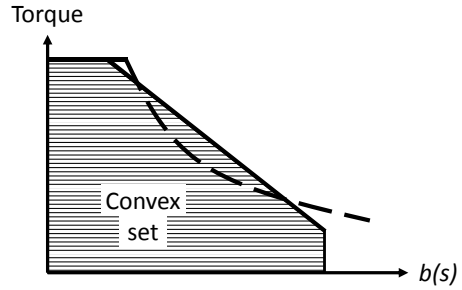

(b) **Set delimited by** (5.30) **(solid line) and comparison with the set delimited by** (5.29) **representing the real power limitation (dashed line)**

Figure 5.2: **Convexity of discussed constraints on torque representing motor power limits**

derivative and considering that the heating coefficient $k_c > 0$ and $\theta_i(s) > \theta_{amb}$ during operation of the ETS:

$$y = -\frac{1}{\sqrt{b}} k_c \left(\theta_i(s) - \theta_{amb}\right); \qquad \frac{d^2y}{db^2} = -\frac{3}{4} b^{-\frac{5}{2}} k_c \left(\theta_i(s) - \theta_{amb}\right) < 0 \quad \forall\, b > 0$$

Therefore the integral of (5.31) is not convex. This prevents setting a temperature limit in the convex optimization problem. Instead, a limit on the heating energy over the whole trajectory is set in the following form:

$$\int_0^{\bar{s}} \frac{T_i^2(s)}{\sqrt{b(s)}}\, ds \leq E_{h,max} \quad \text{with } i = \{l, r\} \tag{5.32}$$

with $E_{h,max}$ maximum allowed heating energy level for each motor over the whole trajectory. This is not an explicit energetic quantity, but a parameter proportional to the heating energy since no heating coefficients appear in (5.32). Determining the appropriate limit in a real application can be done with knowledge of the real system. The Hessian matrix of the argument $y = T_i^2(s)/\sqrt{b(s)}$ is:

$$H_y = \begin{bmatrix} \frac{d^2y}{dT_i^2} & \frac{d^2y}{dT_i \cdot db} \\ \frac{d^2y}{dT_i \cdot db} & \frac{d^2y}{db^2} \end{bmatrix} = \begin{bmatrix} \frac{2}{\sqrt{b}} & -\frac{T_i}{\sqrt{b^3}} \\ -\frac{T_i}{\sqrt{b^3}} & \frac{3}{4}\frac{T_i^2}{\sqrt{b^5}} \end{bmatrix}$$

It is positive-definite as its determinant is $T_i^2/2b^3 > 0\, \forall\, T, b > 0$ and its first component is $2/\sqrt{b} > 0\, \forall\, b > 0$. Therefore the argument of the integral is convex and (5.32) is in turn convex due to the preservation of convexity through the path integral [18]. Because the motor cooling is neglected, a constraint of this kind is more conservative than a temperature limit of the form of (5.31).

5.3.6 Cost functions

Two cost functions will be considered and compared. The first one is the integral of the travel time over the whole trajectory from the starting point $s = 0$ to the end point $s = \bar{s}$ and will be used in a time minimizing optimization problem:

$$C_T = \int_0^{t(\bar{s})} t \, dt = \int_0^{\bar{s}} \frac{1}{\dot{s}} ds = \int_0^{\bar{s}} \frac{1}{\sqrt{b(s)}} ds \tag{5.33}$$

This cost function is convex in the optimizing variables as the argument is a convex function of b.

The second cost function is the total fuel consumption along the trajectory:

$$C_F = \int_0^{t(\bar{s})} c(t) dt \tag{5.34}$$

Substituting (5.15), reminding that $\dot{s} = \sqrt{b(s)}$ and considering the assumed motor speeds (5.28), the fuel consumption is expressed as a function of s:

$$C_F = \int_0^{\bar{s}} \left[c_0 + \frac{c_1}{R_R} \left(T_l^+(s) + T_r^+(s) \right) \sqrt{b(s)} \right] \frac{1}{\sqrt{b(s)}} ds$$

$$C_F = c_0 C_T + \int_0^{\bar{s}} \left[\frac{c_1}{R_R} \left(T_l^+(s) + T_r^+(s) \right) \right] ds \tag{5.35}$$

where the following shorthand notation appears: $T_i^+ = \max\{0, T_i\}$ with $i = \{l, r\}$. (5.35) is convex in b, T_l and T_r since the first term is convex (see (5.33)) and the second term is the integral of maximum functions of T_l, T_r which are convex. It should be noted that the first term related with the APU idle fuel consumption is C_T weighted by the idle fuel consumption c_0. This suggests that the minimization of C_F will determine a trade-off between pure time minimization and pure energy minimization.

5.3.7 Summary of the convex optimization problem

The convex optimization path-following problem is stated as follows:

$$
\begin{aligned}
\underset{a,b,T_l,T_r,F_{yf}}{\text{minimize}} \quad & \epsilon\, C_T + (1-\epsilon)\, C_F \\
\text{subject to} \quad & \mathbf{m}(\mathbf{s})a(s) + \mathbf{r}(\mathbf{s})b(s) = \mathbf{F}(\mathbf{s}) - \mathbf{R} \\
& -T_{max} \leq T_i \leq T_{max} \\
& |T_i(s)| <= T_{max} - k_P(b(s) - b_P) \quad \text{with } i = \{l, r\} \\
& \int_0^{\bar{s}} \frac{T_i^2(s)}{\sqrt{b(s)}}\, ds \leq E_{h,max} \quad \text{with } i = \{l, r\} \\
& -F_{yf,max} \leq F_{yf} \leq F_{yf,max} \\
& a(s) = \frac{1}{2}\frac{db(s)}{ds} \\
& b(s) > 0,\ b(0) = b_0,\ b(\bar{s}) = b_{\bar{s}}
\end{aligned}
\tag{5.36}
$$

The factor ϵ is a weighting factor for the two cost functions. $\epsilon = 0$ results in a fuel minimization problem; $\epsilon = 1$ determines a time minimization problem. b_0 and $b_{\bar{s}}$ are the squared initial speed and squared final speed respectively.

5.4 Solving the Optimization Problem

This section presents an example of trajectory optimization to illustrate the capabilities of this problem formulation and draw first conclusions from the results of the path-following optimization.

5.4.1 Transformation into discrete optimization problem

Implementing the problem in a computer requires the transformation of (5.36) into a discrete optimization problem. The equations are transformed into a discrete form by applying the trapezoidal rule. The discrete optimization problem is formulated as

follows:

$$
\begin{aligned}
\underset{a,b,T_l,T_r,F_{yf}}{\text{minimize}} \quad & \epsilon\, C_T + (1-\epsilon)\, C_F \\
\text{subject to} \quad & \mathbf{m}_k a_k + \mathbf{r}_k b_k = \mathbf{F}_k - \mathbf{R} \\
& -T_{max} \leq T_{i,k} \leq T_{max} \\
& |T_{i,k}| <= T_{max} - k_P(b_k - b_P) \quad \text{with } i = \{l, r\} \\
& \sum_{k=0}^{n} \frac{T_{i,k}^2(s)}{\sqrt{b_k}} \leq E_{h,max} \quad \text{with } i = \{l, r\} \\
& -F_{yf,max} \leq F_{yf,k} \leq F_{yf,max} \\
& a_k = \frac{1}{2}\frac{b_{k+1} - b_k}{\Delta s_{k+1}} \\
& b_k > 0 \; \forall \; k \in [1, n], \; b_1 = b_0, \; b_n = b_{\bar{s}}
\end{aligned}
\tag{5.37}
$$

where the index $k \in [1, n]$ refers to each of the n points of the discretized taxi trajectory. This is now described through a matrix of global X, Y coordinates and course angles for each discrete point, as well as the discretization step Δs_k to the next trajectory point:

$$
\mathbf{p} = \begin{bmatrix} p_{X,1} & p_{Y,1} & p_{\psi,1} \\ \vdots & \vdots & \vdots \\ p_{X,n} & p_{Y,n} & p_{\psi,n} \end{bmatrix} \qquad \mathbf{\Delta s} = \begin{bmatrix} \Delta s_1 \\ \vdots \\ \Delta s_n \end{bmatrix} \tag{5.38}
$$

All quantities presented in sections 5.3.2 and 5.3.3 are now defined in discrete form for each point along the trajectory: the first and second derivative vectors of the path kinematics $\mathbf{p}'_k, \mathbf{p}''_k$, the transformation matrix from local to global coordinates $\mathbf{T}_k$, the equivalent mass and damping matrices $\mathbf{m}_k, \mathbf{r}_k$, the trajectory-dependent components of the vehicle speed $L_{x,k}, L_{y,k}, L_{\dot{\psi},k}$, and the vector of generalized vehicle forces $\mathbf{F}_k$. The cost functions (5.33) and (5.35) are transformed into discretized form by summations along the trajectory. Applying the trapezoidal rule involves calculating the average values of the arguments between two subsequent points:

$$
C_T = \sum_{k=1}^{n-1} \frac{\Delta s_k}{2} \left(\frac{1}{\sqrt{b_k}} + \frac{1}{\sqrt{b_{k+1}}} \right) \tag{5.39}
$$

$$
C_F = c_0 C_T + \sum_{k=1}^{n-1} \frac{c_1}{2R_R} \left(T_{l,k}^{+} + T_{r,k}^{+} + T_{l,k+1}^{+} + T_{r,k+1}^{+} \right) \tag{5.40}
$$

The optimizing variables a, b, T_l, T_r, F_{yf} representing the solution of the discretized optimization problem are now vectors defining the respective quantities for each trajectory step. These vectors will be interpolated linearly afterwards to generate continuous signals for the control of the modeled ground propulsion system.

Table 5.1: **Description of the trajectory chosen for the test of the optimization setup. "L" in the Geometry column is the length of the element (arc length for curves); "R" is the curve radius. A negative curve radius means a right curve, a positive one means a left curve**

Element	Geometry	Discretization step Δs_k
Straight #1	L = 300 m	20 m
Transition	L = 20 m	2 m
Corner #1	R = 250 m, L = 372 m	2 m
Transition	L = 20 m	2 m
Straight #2	L = 2200 m	20 m
Transition	L = 40 m	2 m
Corner #2	R = -100 m, L = 215 m	2 m
Transition	L = 40 m	2 m
Straight #3	L = 300 m	20 m
Transition	L = 30 m	2 m
Corner #3	R = 200 m, L = 215 m	2 m
Transition	L = 30 m	2 m
Straight #4	L = 600 m	20 m
Transition	L = 30 m	2 m
Corner #4	R = 450 m, L = 115 m	2 m
Transition	L = 30 m	2 m
Straight #5	L = 900 m	20 m

The discretized optimization problem was programmed in the Matlab [9] computing environment. The convex optimization tool CVX [3] was used for this purpose. This tool uses a paradigm called by the authors *Disciplined convex programming* [38] offering a framework of commands and syntax conventions that allows to code some classes of convex optimization problems conveniently. The problem was solved with the SDPT3 numerical solver for semidefinite-quadratic-linear programming. [81] The vectors of the optimization variables $b_k, T_{l,k}, T_{r,k},$ and $F_{yv,k}$ were normalized through specific coefficients to keep them in a similar order of magnitude, thus improving the numeric efficiency of the solver.

5.4.2 Optimization of the taxi trajectory example

The problem setup was tested by optimizing the travel along the test trajectory shown in Figure 5.3. It is composed by a number of straights and turns with different radii; these elements are linked with each other through clothoid transitions to ensure a smooth yaw rate change. The reader is referred to section 5.6.1 further on for more detailed information on designing taxi trajectories for the path-following optimization.

Table 5.2: **Parameters of aircraft considered**

Parameter	Symbol	Value
Mass	m	67,250 kg
Inertia coeff. around z-axis	J_z	$3.75 \cdot 10^6$ kg $\cdot$ m^2
Main gear y-distance	a_r	3.795 m
Main gear x-distance	b_r	2.51 m
Nose gear x-distance	b_f	10.19 m
Maximum nose gear lateral force	F_{yv}	3298.6 N
APU idle fuel flow	c_0	0.02 kg/s
APU fuel flow/power	c_1	$6.95 \cdot 10^{-8}$ kg/(s $\cdot$ W)
Cornering stiffness of nose gear	c_f	$1.49 \cdot 10^5$ N/rad
Cornering stiffness of main gear	c_r	$6.16 \cdot 10^5$ N/rad
Thermal limitation	$E_{h,max}$	13

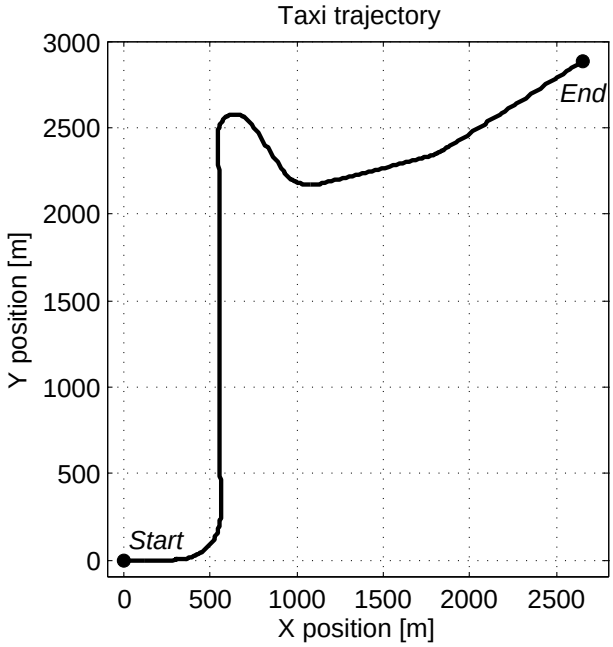

Figure 5.3: **Trajectory chosen for the test of the optimization setup**

The geometries of the trajectory elements are described in Table 5.1. Based on the different discretization steps shown in the table and reminding that the vehicle side

slip β is set to zero, that continuous description was transformed into a discrete one in the format given in (5.38). Using different discretization steps for straights and corners is the result of a trade-off between computational effort and precision of the solution. Both the initial speed $\sqrt{b_0}$ and final speed $\sqrt{b_s}$ were set at 0.1 m/s. Also, a speed limit vector $\tilde{\mathbf{v}}_\mathbf{x} = [\tilde{v}_{x,1}, \ldots, \tilde{v}_{x,n}]$ was defined to control the maximum admissible speed along the trajectory and the following set of constraints was added to the optimization problem:

$$b_k \leq \tilde{v}_{x,k}^2 \quad \forall\, k \in [1, n]$$

For the maximum tire lateral forces $F_{yf,max}, F_{yl,max}$, and $F_{yr,max}$ at tire saturation, a friction coefficient $\mu = 0.5$ was assumed. Furthermore, the nose gear maximum force was limited to a conservatively established 20% of this value to guarantee stable conditions. The limits for each wheel are determined by the weight distribution according to the relative positions to the center of gravity (see Figure 5.1), neglecting any weight transfers caused by the dynamics:

$$F_{yf,max} = 0.2\, \frac{b_r}{b_f + b_r} \cdot \mu m g$$

$$F_{yl,max} = F_{yr,max} = \frac{1}{2} \frac{b_f}{b_f + b_r} \cdot \mu m g$$

where g is the gravity acceleration. Recalling the tire model used in (5.4) and the tire slips as functions of the path in (5.23) and (5.24), the main gear lateral forces are defined in advance for each discrete point of the trajectory and are used for the first two components of the vector $\mathbf{F}_k$.

This optimization problem was solved for a mid-size, narrow-body aircraft with the parameters listed in Table 5.2.

The optimization goal was consumption minimization ($\epsilon = 0$) with a thermal limit set to $E_{h,max} = 13$. The kinematics and dynamics resulting from the optimization are shown in Figure 5.4 and 5.5. In the latter diagram, the average motor torque $T_{avg} = (T_l + T_r)/2$ and differential motor torque $T_{diff} = T_r - T_l$ are shown in the plots. This linear combination of the optimizing variables T_l, T_r is preferred when discussing the results in order to have a better feeling for the effects of the motor actuation: T_{avg} influences the longitudinal dynamics whereas T_{diff} influences the yaw dynamics.

Because the cost function and the thermal limitation penalize the application of motor torques, it can be seen in Figure 5.5 that no differential moments were applied since the nose gear tire was not saturated in this particular trajectory and was able to generate the desired yawing behavior. Due to the simplifications made in the vehicle model, the nose gear steering does not induce any motion resistance in the longitudinal direction which should be counterbalanced by additional motor torque, therefore nose gear steering is the preferred method of generating yaw moment whenever possible in this optimization setup.

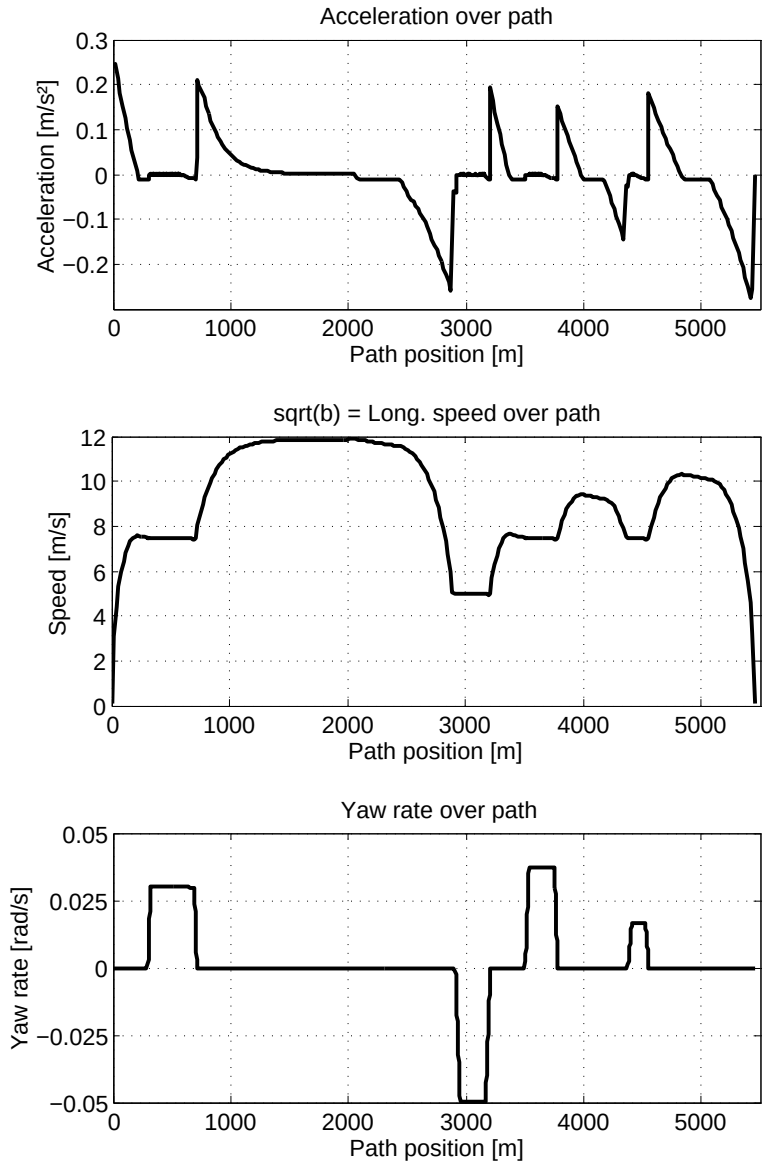

Figure 5.4: **Optimization results for test trajectory, kinematic variables**

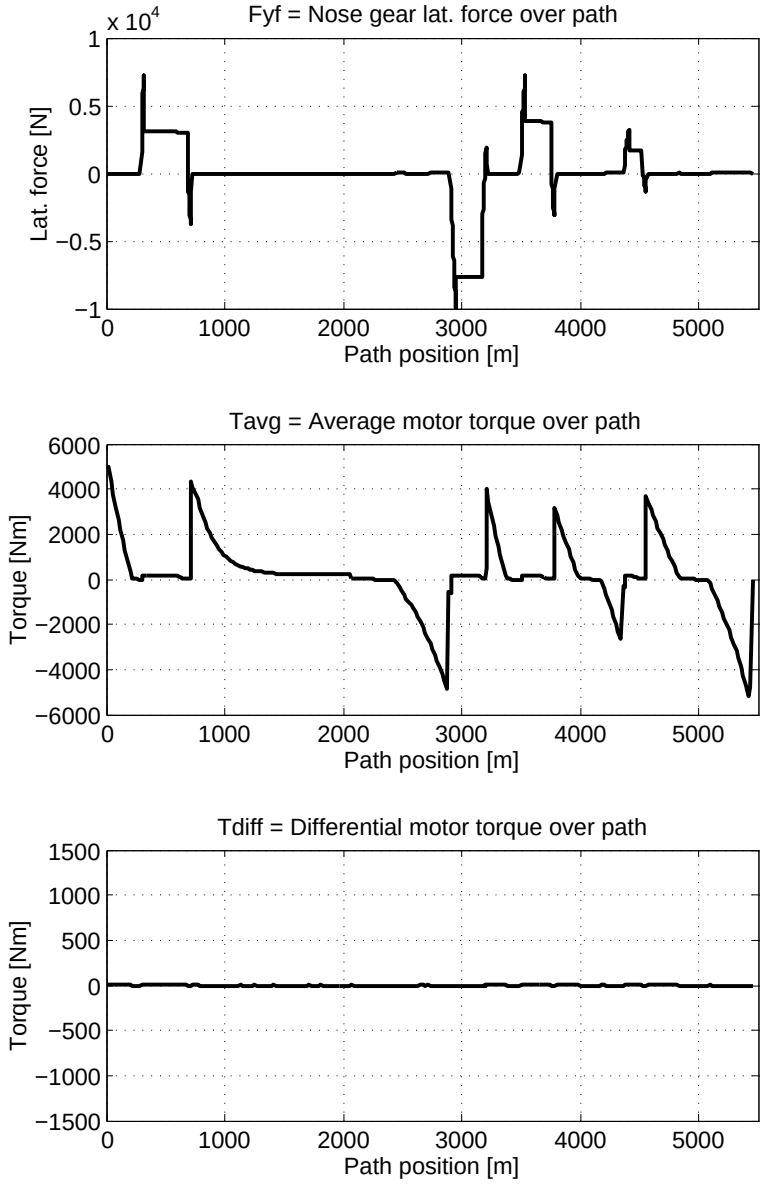

Figure 5.5: **Optimization results for test trajectory, dynamic variables**

Table 5.3: **Summary of performed optimizations with main results**

Opt. Name	Description	ϵ	$E_{h,max}$	Time [s]	Fuel Cons. [kg]
T	Time minimization	1	∞	621.3	17.9
C	Consumption minimization	0	∞	626.1	17.8
HT	Time minim., thermal limits	1	13	654.3	18.3
HC	Consumption min., thermal limits	0	13	655.9	18.2

Inverting the equation for the nose gear slip angle in (5.5) allows to verify whether the resulting steering angle command δ is applicable in reality. The diagrams in Figure 5.6 show the steering angle and steering rate corresponding to the optimal solution. It can be seen that for this trajectory, the modulus of the steering angle δ is never greater than approximately 0.1 radians = 5.7 degrees, whereas the modulus of the steering rate $\dot{\delta}$ is never greater than 0.015 rad/s, which is known to be compliant with the performances of real nose gear steering systems on mid-size aircraft. This result is not surprising since the trajectory considered features smooth transitions between straights and corners.

5.4.3 Comparison of cost functions and thermal limits

In this section, four optimizations with different problem setups are compared. Table 5.3 shows the changing parameters of the four optimizations as well as their fuel consumptions and travel times. In the following, the four cases will be called T, C, HT, and HC as detailed in Table 5.3. The HC setup corresponds to the optimization results discussed in the previous section and shown in Figure 5.4 and 5.5. The aim of this comparison is to investigate the effect of the thermal constraint and the differences between a time minimizing optimization and a consumption minimizing optimization.

The difference between the two optimization criteria is found to be small regarding both the fuel consumption and the travel time. This difference is further reduced if heat energy limits are used. The reason of this lies in the relatively high APU idle consumption. Figure 5.7 shows the contribution of each of the two summands in the consumption minimizing cost function (5.40) representing the idle consumption and the power-related consumption respectively. Only the T and C optimization setups are shown for clarity. It is apparent that the idle consumption accounts for most of the total fuel consumption, which skews the trade-off between time and fuel consumption sensibly towards the time minimization. In other words, an APU used at only a fraction of its power has such a low efficiency that the fuel minimizing path is hardly different from the time minimizing path and the energetically best strategy implies short travel times, hence relatively high average speeds.

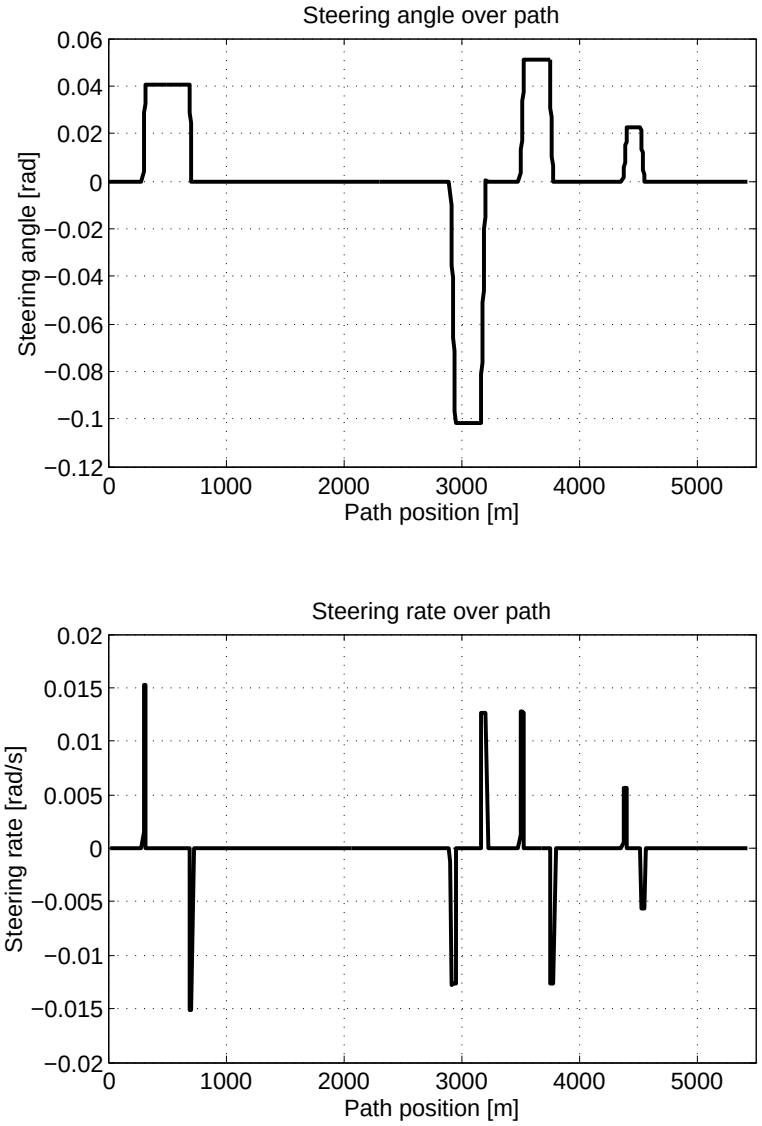

Figure 5.6: **Optimization results for test trajectory, steering angle and steering rate**

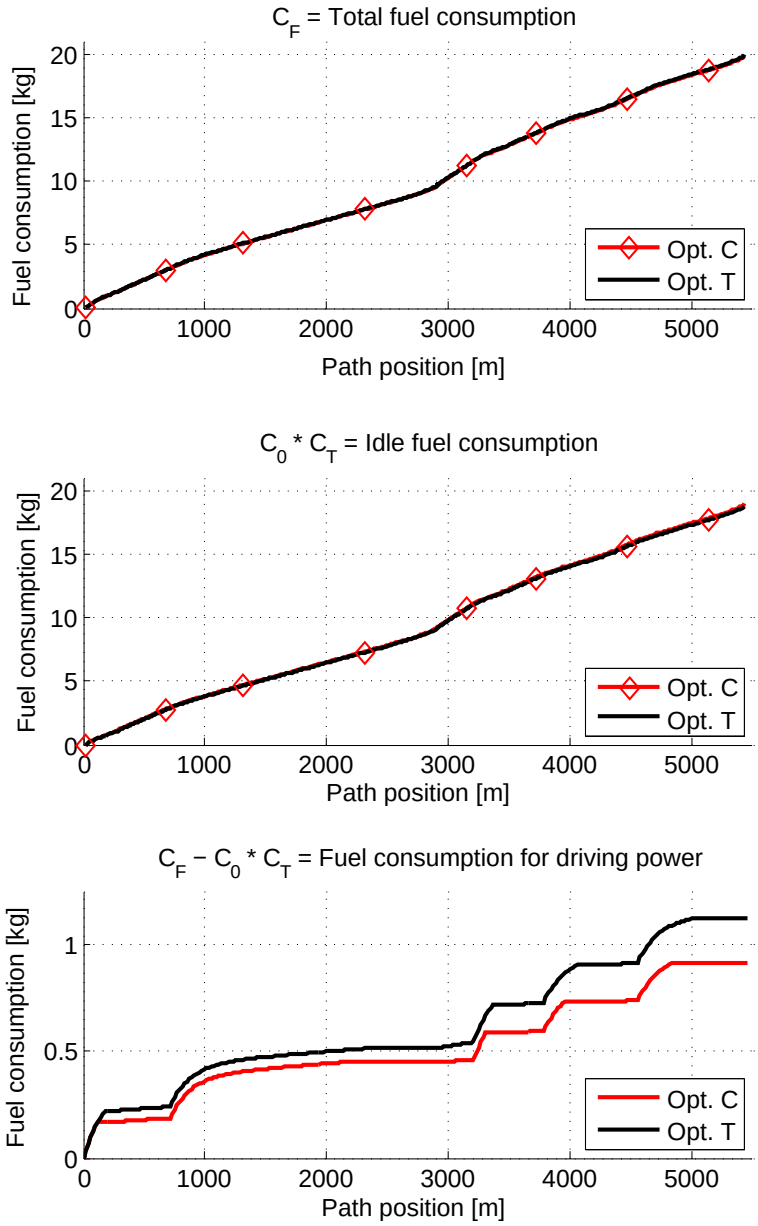

Figure 5.7: **Comparison between overall APU fuel consumption as well as idle part and driving power part for the T and C optimization setups. The two lines mostly overlap in the first two diagrams because of the very small difference in overall fuel consumption and travel time (which impacts on the idle fuel consumption). A difference is visible in the last diagram showing the fuel consumption due to generation of driving power, which is due to the different optimizing goal.**

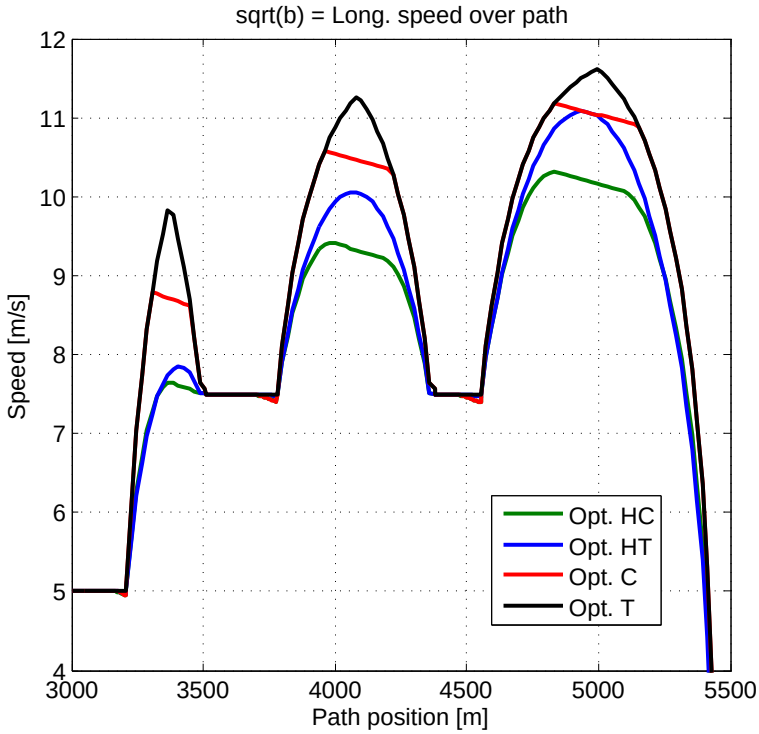

Figure 5.8: **Comparison between speeds for the four optimization setups in the second part of the test trajectory**

The longitudinal speeds in the final part of the trajectory, including the last three corners (nearly constant-speed phases at the respective speed limit) and the last three straights (accelerating-decelerating peaks), are shown in Figure 5.8 for the four optimization setups to show the different optimized solutions in detail. The time minimizing optimization without thermal limits (optimization "T" in Figure 5.8) commands the highest average speeds in straights: the system capabilities are exploited fully, with maximum power either in acceleration or deceleration. In the fuel minimizing optimization without thermal limits (optimization "C" in Figure 5.8), the maximum speeds reached in straights are not as high: after reaching a certain speed, rolling without driving torques is used to travel along a straight. The speed decreases slowly due to the rolling resistances $\mathbf{R}$. The two optimizations with thermal limits (called "HT" respectively "HC" in Figure 5.8) show a similar behavior; however, the accelerations — and consequently the average speeds — are lower than without thermal limits because reduced motor torques are generally applied.

Figure 5.9 shows the nose gear lateral force and the differential torques in a small portion of the trajectory including the second and the third corner. The T optimization

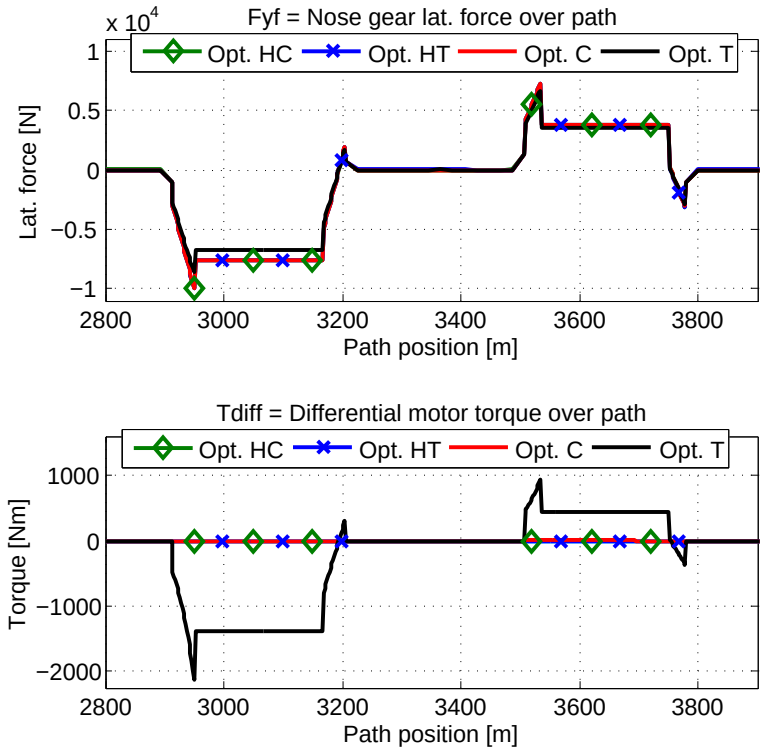

Figure 5.9: **Comparison between nose gear lateral forces (above) and differential motor torques (below) for the four optimization setups during the second and third corner of the test trajectory. While the C, HC and HT setups overlap almost perfectly, the T setup behaves differently in that some differential torque is applied during corners. This also results in less lateral force needed from the nose gear steering compared to the other three setups.**

setup (time minimization without thermal limits) behaves differently from the other optimizations. Because the motor torques are not penalized in the time minimizing setup, some differential torque is commanded together with a lower nose gear lateral force. By contrast, the three other setups penalize driving torques to some extent either in the cost function or through the heat energy limits, therefore only the nose gear lateral force is used to corner whenever possible.

5.5 Minimum-Time Constraints

Taxiing in a busy airport may be subject to a number of constraints due to the surrounding traffic. For instance, points of conflict such as runway and taxiway crossings

must be cleared within a time window usually defined by the ground control authority in order to minimize the impact on other traffic, thus maximizing the airport capacity. It would therefore be interesting to include constraints on the travel time over the whole trajectory or sections of it in the optimal path following framework, and in particular constraints on the time that must at least elapse before specific waypoints are cleared. This kind of constraint will be referred to as a *minimum-time constraint*. An intuitive explanation as to why minimum-time constraints are of particular interest in this work is that, if it is known that a certain waypoint must not be passed too early, then more uniform, lower speeds on average might generally be traveled in a context of energy minimization rather than traveling at relatively higher speeds only for having to wait for the minimum passing time at the waypoint. By contrast, constraints on the *maximum* available time to clear a waypoint (i.e. *maximum-time constraints*), while also important in practical operations, are less interesting in the present study. It was noted in the previous chapter that even when minimizing the fuel consumption, very similar results are obtained as with time minimization. To put it differently, performances close to the maximum are already commanded even when time is not a factor. Maximum-time constraints that are sensibly different than the times already achieved in non-constrained optimization cannot be met because of insufficient performance and just result in an infeasible optimization problem. Maximum-time constraints are therefore performance sizing factors in the system design rather than parts of the path-following optimization problem.

It was shown in Section 5.4.3 that the optimal travel time with consumption minimization as optimization goal is only marginally longer than the minimal time. Setting minimum-time constraints can therefore be expected to lower the average speed, which would require less kinetic energy. This could be beneficial for the thermal behavior of the motors since the average temperatures may be lower. Conversely, because the APU idle consumption is high, the overall fuel consumption should become larger than the case without time constraints.

While minimum and maximum passing times may theoretically be derived by thorough investigation of the airport flight schedule, they are clearly influenced and determined by the momentary traffic situation, hence a precise forecast of the passing times can be hard to achieve in everyday practice. These aspects pertaining to ground traffic management fall outside the scope of this thesis. In the following analysis, it is assumed that passing times are known precisely — within an order of magnitude of one second — prior to the offline calculation of the optimal taxi trajectory. The primary aim of this work is to show how time constraints can be included into the path following optimization problem and how their exploitation can impact positively on the assessment and design of electric taxi systems.

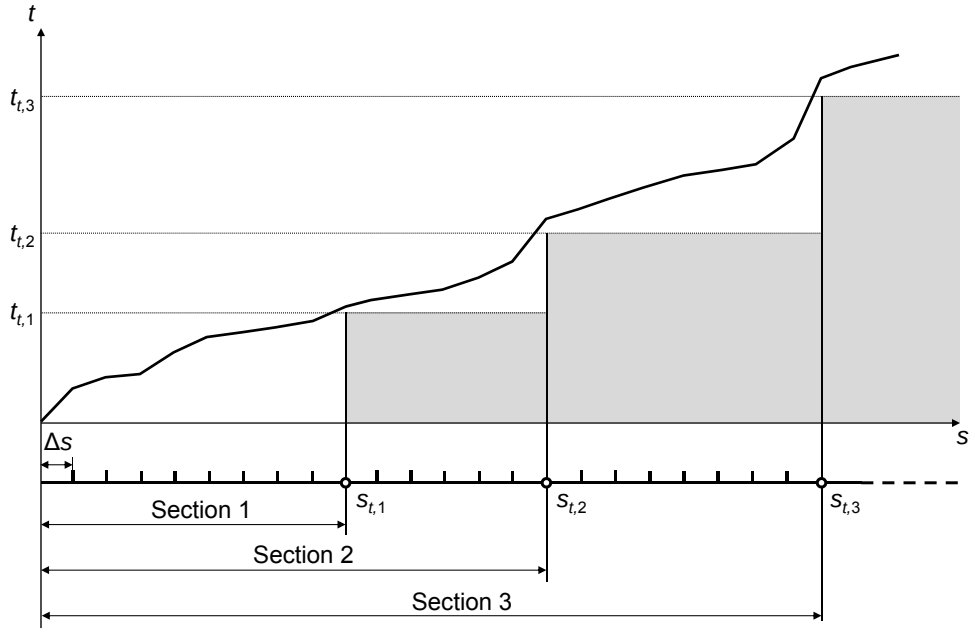

Figure 5.10: **Path-time diagram illustrating an example with three minimum-time waypoints and sections. Each waypoint $s_{t,k},\ k \in [1,3]$ may be passed only if the related minimum time $t_{t,k}$ has elapsed. This defines the non-permissible area marked in grey. Note that while the length of the discretized segments Δs has been drawn constant in the diagram, this needs not be the case in general.**

5.5.1 Definition of minimum-time constraints

It is assumed that a number of constraints is given on the minimum time in which certain waypoints s_t along the trajectory are reached, i.e. the aircraft cannot pass those waypoints before the given time elapsed from start of taxi (see Figure 5.10). The portion of trajectory from start (i.e. $s = 0$) to the k-th waypoint $s_{t,k}$ will be referred to as *section* k.

The travel time needed to reach the waypoint s_t from start is expressed as:

$$t_t = \sum_{i=1}^{t-1} \frac{2\Delta s_i}{\sqrt{b_i} + \sqrt{b_{i+1}}} \tag{5.41}$$

This is the summation of the travel times along each discrete portion of the trajectory, expressed as length of each portion Δs_i divided by the average speed along that portion, given by $\left(\sqrt{b_i} + \sqrt{b_{i+1}}\right)/2$.

Remark 1. *The expression* (5.41) *is a convex function of* $b_1 \dots b_n$.

Proof. We start by considering a generic single element of the summation, i.e.

$$f\left(b_i, b_{i+1}\right) = \frac{2\Delta s_i}{\sqrt{b_i} + \sqrt{b_{i+1}}}$$

which is defined for the domain $b_i, b_{i+1} \in (0, +\infty]$. The square root function $q(x) = \sqrt{x}$ is concave $\forall\ x > 0$ since $q'' = -1/4 \cdot x^{-3/2} < 0\ \forall\ x > 0$. Since the sum of concave functions is also concave, [18] it follows that $g(b_i, b_{i+1}) = \sqrt{b_i} + \sqrt{b_{i+1}}$ is concave.

Considering $h(x) = 2\Delta s_i / x$ and noting that $h'(x) = -2\Delta s_i x^{-2} < 0\ \forall\ x > 0$ and $h''(x) = 4\Delta s_i x^{-3} > 0\ \forall\ x > 0$, we can now apply a composition rule for convexity [18] stating that $f\left(b_i, b_{i+1}\right) = h\left(g(b_i, b_{i+1})\right)$ is convex since g is concave and h is convex and monotonically decreasing. Finally, by noting that the sum of convex elements is convex [18], we conclude that the summation in (5.41) is a convex function of $b_1 \ldots b_n$. □

A constraint on the minimum travel time would be:

$$t_t\left(b_1 \ldots b_n\right) - \tilde{t}_t \geq 0$$

which is of the form [convex expression ≥ 0]. This type of constraint is not permitted in the convex optimization problem setup (5.14), as only constraints of the form [convex expression ≤ 0] or [concave expression ≥ 0] are allowed. For this reason, a constraint on the minimum travel time along a section of the trajectory cannot be taken into account exactly, but only in an approximated way.

5.5.2 Approximation of the minimum-time constraint

The way followed in this work to approximate the minimum time constraint is to set constraints on the travel speed. Setting a minimum time along a section is equivalent to setting a maximum average speed along that section. The expression for the average speed over a section from start to the waypoint s_t is:

$$\bar{v}_t = \frac{\sum_{i=1}^{t-1} \Delta s_i}{\sum_{j=1}^{t-1} \frac{2\Delta s_j}{\sqrt{b_j} + \sqrt{b_{j+1}}}} \tag{5.42}$$

The convexity property of (5.42) will now be checked. Let $g : \mathbb{R} \to \mathbb{R}$ be a convex function of x (i.e. $g'' > 0$) and $h : \mathbb{R} \to \mathbb{R}$ be a convex, monotonically decreasing function of x (i.e. $h' < 0,\ h'' > 0$). Considering a composition $f = h\left(g(x)\right)$, the sign of its second derivative $f'' = h''g'^2 + h'g''$ cannot be determined in general since $h''g'^2 > 0$ and $h'g'' < 0$. Therefore, nothing about the convexity property can be stated in general about f. This conclusion can be extended to the multi-dimensional case, i.e. with $g : \mathbb{R}^n \to \mathbb{R}$. Taking:

$$g(b_1 \ldots b_n) = \sum_{j=1}^{t-1} \frac{2\Delta s_j}{\sqrt{b_j} + \sqrt{b_{j+1}}} \qquad h(x) = \frac{1}{x} \sum_{i=1}^{t-1} \Delta s_i$$

nothing can be said about the definiteness of the Hessian matrix of $\bar{v}_t = h\left(g(b_1 \dots b_n)\right)$. Therefore, the average speed (5.42) is not convex, thus not suitable as a constraint in the convex optimization problem.

The following expression is proposed in this work to approximate a minimum time constraint over a trajectory section from start to the waypoint s_t:

$$\frac{\sum_{i=1}^{t-1} \Delta s_i \frac{b_i + b_{i+1}}{2}}{\sum_{j=1}^{t-1} \Delta s_j} \leq \left(\frac{\sum_{j=1}^{t-1} \Delta s_j}{\tilde{t}_t} \right)^2 \tag{5.43}$$

The left term is an affine, hence convex function of $b_1 \dots b_n$ and returns the weighted average of the mean values of the squared speed b over all the trajectory segments. The weighting factor is the length Δs_i of each segment. The right term is the square of the maximum allowed average speed, given by the quotient between the length of the considered section and the minimum travel time required. Note that the left term does in general not correspond to the square of the average speed over the considered trajectory section; this would be given by the square of (5.42). A sufficient condition for the two expressions to coincide is when only one single trajectory segment is considered, which is not the case in general.

As a consequence of this fact, we replace $\tilde{t}_t$ with $\tilde{t}_t^*$ in (5.43). This is no longer the required minimum time, but a parameter with the dimensionality of time that can be used to influence the minimum travel time over the considered section. Being this only an approximation, its value needs to be determined iteratively over several optimization runs.

Case with one minimum-time section

The following algorithm is applied to determine $\tilde{t}_t^*$ in a case with only one minimum-time section:

1. Initialize $\tilde{t}_t^*$ by using the required minimum travel time $\tilde{t}_t$;
2. perform an optimization run;
3. calculate the travel time t_t over the section by (5.41) and check that the difference $t_t - \tilde{t}_t$ is in the range [0,1]. This range ensures that the minimum time constraint is respected (i.e. $t_t - \tilde{t}_t > 0$ s) while discarding too conservative results ($t_t - \tilde{t}_t <$ 1 s);
4. if the difference check succeeded, then keep $\tilde{t}_t^*$ and terminate the algorithm, otherwise subtract $t_t - \tilde{t}_t$ from $\tilde{t}_t^*$ and jump to point no. 2.

Case with several minimum-time sections

If a number $r \in \mathbb{Z}, r > 1$ of constraints are set for different trajectory sections that have segments in common, their mutual influences must be taken into account. Remind that by *section* k, a portion of trajectory from the beginning of the trajectory ($s = 0$) to a defined waypoint $s = s_{t,k}$ is meant. When multiple sections are considered, they will therefore be nested in each other, every section starting from $s = 0$. It may be the case that setting a minimum time constraint on certain sections already causes the minimum time in some of the other sections to be respected without setting the respective constraints. Even if all constraints are needed anyway, the mutual influences between the different sections may cause the need for some adaptation in the parameter values. A suitable iterative strategy consists in finding the minimum-time parameter $\tilde{t}_{t,k}$ for each section $k \in [1, r]$ starting from the last one and going backwards, while checking in each step that all subsequent sections $j \in [k+1, r]$ still respect their respective minimum-time constraints.

The iterative approach in the general case with r constraints on minimum travel time in order to determine the values of the parameter vector $\tilde{\mathbf{t}}^* = \left[\tilde{t}^*_{t,1} \dots \tilde{t}^*_{t,r}\right]$ is described by the flow chart in Figure 5.11 and explained verbally in the following.

Firstly, the parameter vector $\tilde{\mathbf{t}}^*$ is initialized with a vector of ones. Setting a minimum-time parameter to 1 s is used to effectively deactivate that minimum-time constraint: a minimum time of 1 s from start to any waypoint chosen for practical purposes is assumed to be respected by default due to the limited system performance.

Subsequently, an outer loop is started in which for each section k ranging backwards from r to 1, an optimization is run and the passing time $t_{t,k}$ is evaluated. If it is less than the required minimum time $t_{t,k}$, the parameter $\tilde{t}^*_{t,k}$ is adapted and the optimization is run again. This is also the case if the margin is found to be over +1 s and $\tilde{t}^*_{t,k}$ was not 1 s (i.e. not practically deactivated), as this means $\tilde{t}^*_{t,k}$ was effectively controlling the passing time at k and the result was too conservative.

Once a suitable parameter $\tilde{t}^*_{t,k}$ is temporarily identified, an inner loop is started which evaluates whether the passing time $t_{t,j}$ of each section j ranging from r to $k+1$ is still within the target margin of [0 s, +1 s], or still greater than minimum time with a deactivated parameter (i.e. $\tilde{t}^*_{t,j} = 1$) . If these conditions are not met, the parameter $\tilde{t}^*_{t,j}$ is adapted, an optimization is run, and the resulting passing time $t_{t,j}$ is evaluated. If it has remained unchanged after the optimization run, then it is obviously influenced by the passing times of other sections rather than its own parameter $\tilde{t}^*_{t,j}$; therefore, the latter is deactivated by setting $\tilde{t}^*_{t,j} = 1$ and the inner loop continues for the previous waypoint in $[k+1, r]$. If the passing time has changed instead, then the inner loop is aborted and the check starts again from the current k in the outer loop, since the passing times of all the sections after j need to be re-evaluated and re-tuned if necessary.

At the end of the algorithm, the valid optimized solution is given by the optimization

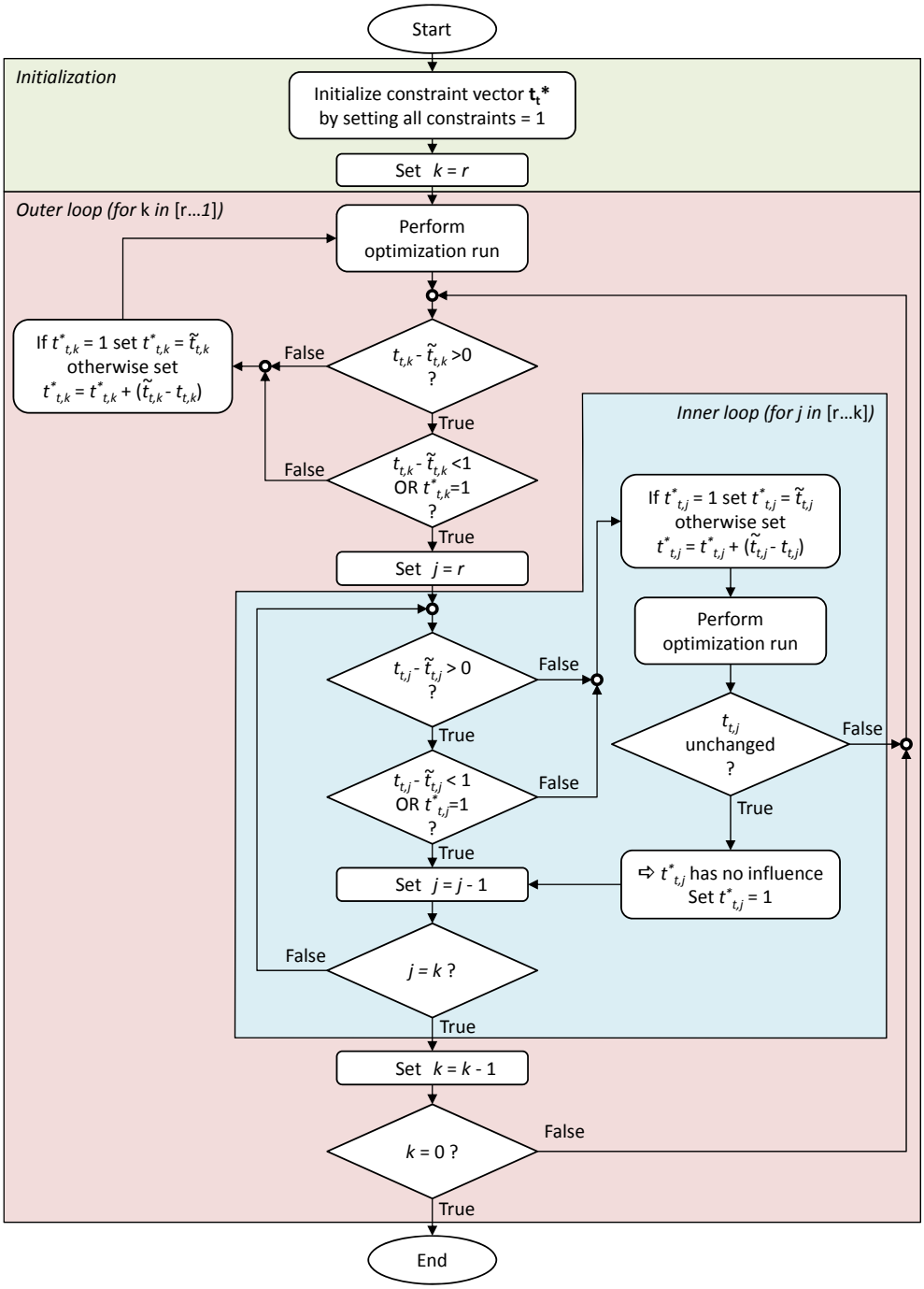

Figure 5.11: **Flow chart of minimum-time parameter finding algorithm for the generic case with several minimum-time constraints**

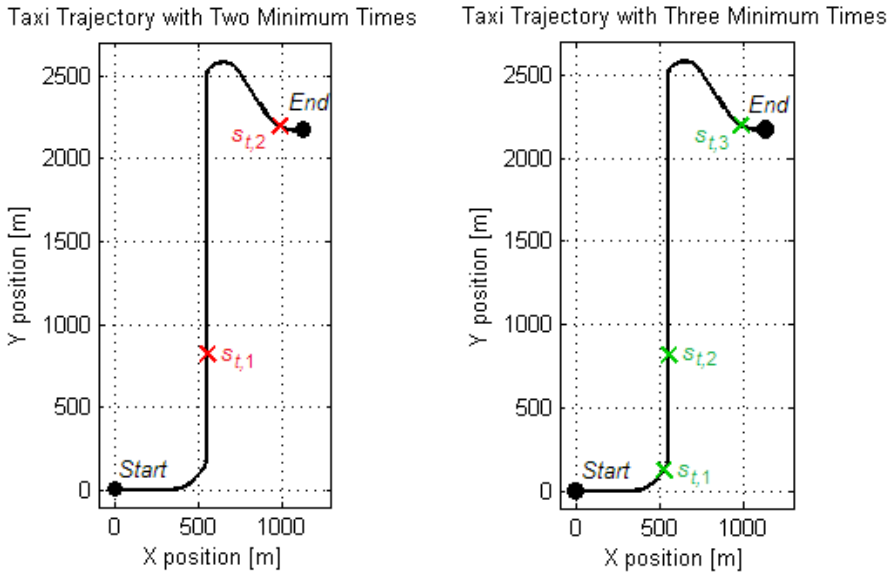

(a) **with two minimum times** (b) **with three minimum times**

Figure 5.12: **Trajectories chosen for the trajectory optimizations subject to minimum times**

run that was performed last, since all the passing time checks were successful.

5.5.3 Examples of optimization with minimum-time constraints

The minimum-time parameter searching algorithm discussed in the previous section has been applied to two examples. The trajectory considered is a portion of the one used in Section 5.4.2 and is plotted in Figure 5.12; also, the same aircraft parameter set is considered. The optimization objective was the minimization of fuel consumption and no thermal constraints were set.

Trajectory with two minimum-time points

In the first example, two minimum-time points are defined as in Figure 5.12a. Their minimum passing times are given as 200 and 500 s respectively from the start. Figure 5.13 shows the converging behavior of the searching algorithm through the deviation between required and actual passing times at the considered waypoints. The vector of minimum-time parameters $\tilde{\mathbf{t}}^*$ needed for the optimization to respect both the required minimum times with a deviation smaller than 1 s is found after iterating

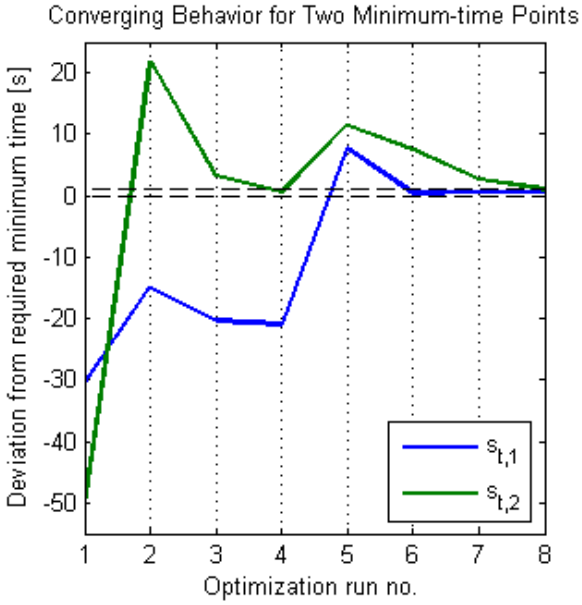

Figure 5.13: **Converging behavior of the minimum-time parameter searching algorithm for the trajectory with two minimum-time points. The dashed horizontal lines highlight the targeted deviation range of [0 s, + 1 s].**

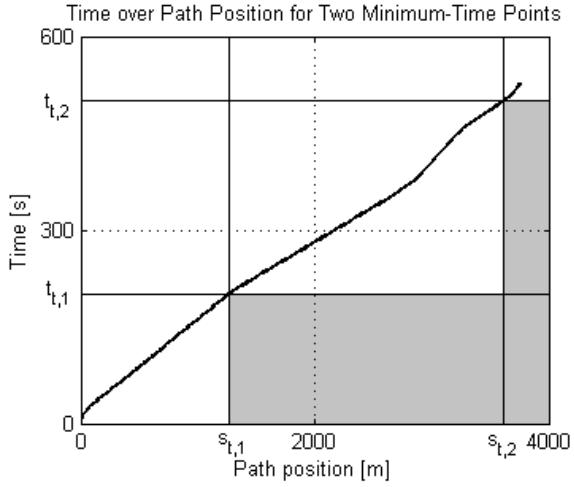

Figure 5.14: **Path-Time diagram for the optimized trajectory with two minimum-time points. The non-permitted area is highlighted in grey.**

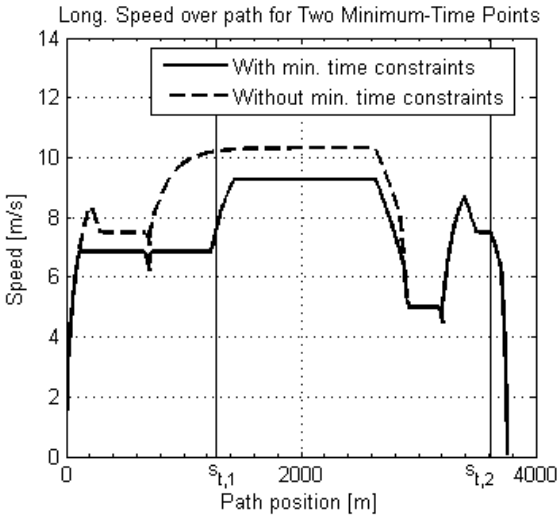

Figure 5.15: **Optimized longitudinal speed over time for the trajectory with two minimum-time points compared with the same trajectory without minimum-time constraints**

8 optimization runs and is $\tilde{\mathbf{t}}^* = [192.3815,\ 464.8008]$. Reminding that the searching algorithm only changes one parameter at a time in each iteration, the mutual influence between the different parameters is apparent in that both deviations change in each iteration. The optimization performed in the last iteration is also the one delivering the final, optimized path-following results. Figure 5.14 shows the path-time diagram for the optimized trajectory, which confirms that the overall speed is regulated so that the non-permitted area is precisely cleared without unnecessary conservativeness at the affected waypoints.

Figure 5.15 shows the calculated optimal longitudinal speeds over the path position for the cases with and without minimum-time constraints. The effect of the minimum-time constraint on the first waypoint can be seen in the speed profile in the vicinity of the first waypoint: after passing the waypoint while being on the same straight (compare the position of the first point along the trajectory in Figure 5.12a), the speed is increased from approx. 7 to approx. 9 m/s. Evidently, a lower speed was necessary before the waypoint to respect the minimum-time condition. In the case without minimum-time constraints, the same portion is passed at full speed of above 10 m/s. Concerning the second waypoint, the speed is kept lower in the straight at around 2,000 meters from start with respect to the case without minimum-time constraints, whereas the corners towards the end of the second portion are passed at the same speeds. Here, the effect of minimizing the fuel consumption seems to play a relevant role in that the speeds that are reduced due to minimum-time constraints are the higher speeds traveled in the straight portions, normally requiring more power.

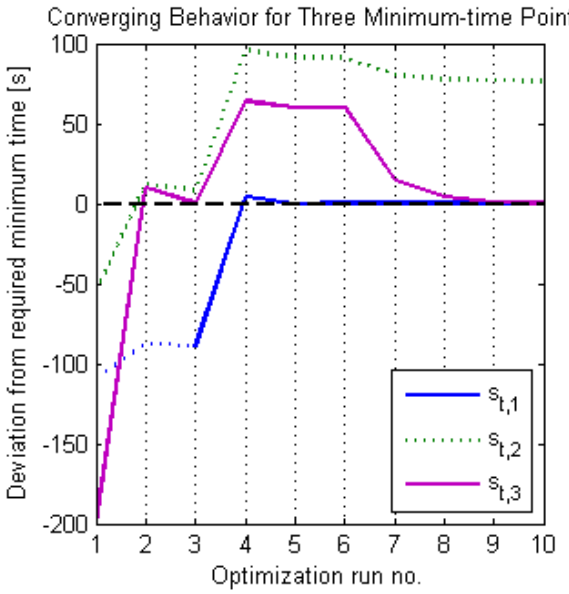

Figure 5.16: **Converging behavior of the minimum-time parameter searching algorithm for the trajectory with three minimum-time points. The dashed horizontal lines highlight the targeted deviation range of [0 s, + 1 s]. The dotted portions of the deviation lines highlight the optimization runs where no effective minimum time constraint was set for the respective waypoint.**

Trajectory with three minimum-time points

In the second example, an additional constrained waypoint is added before the other waypoints (Figure 5.12b). The required minimum passing times are given as 200, 225, and 600 s respectively. The converging behavior of the algorithm in this case is illustrated in Figure 5.16.

The dotted portions of the lines in the diagram highlight the runs in which an ineffective minimum-time constraint of 1 was set. This means the passing time for the related waypoint in those runs was due to the minimum-time constraints of the other waypoints. This was always the case for the second waypoint $t_{s,2}$ until convergence, i.e. the passing times of the first and third waypoint influence the traveling speed in such a way that the passing time condition on the second waypoint is already met without need for an extra constraint. This is illustrated in Figure 5.17: the trajectory on the path-time diagram clears the second waypoint with a sensible margin from the non-permissible area. Ten optimization runs are necessary before the final vector of minimum-time parameters $\mathbf{t}^* = [195.6049,\ 1,\ 560.0195]$ guaranteeing respect of the minimum passing times is found. It can be seen once again from Figure 5.18 that

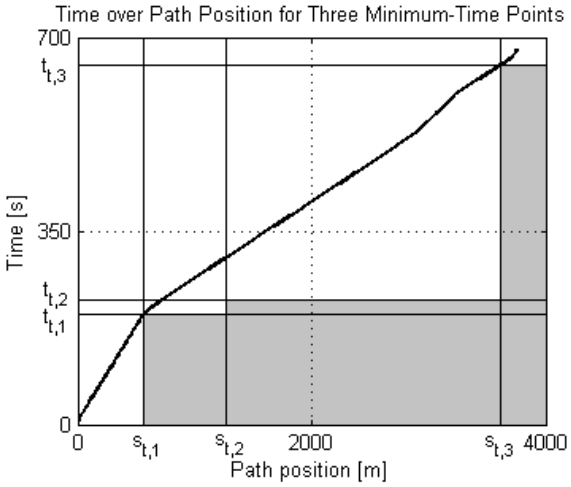

Figure 5.17: **Path-Time diagram for the optimized trajectory with three minimum-time points. The non-permitted area is highlighted in grey.**

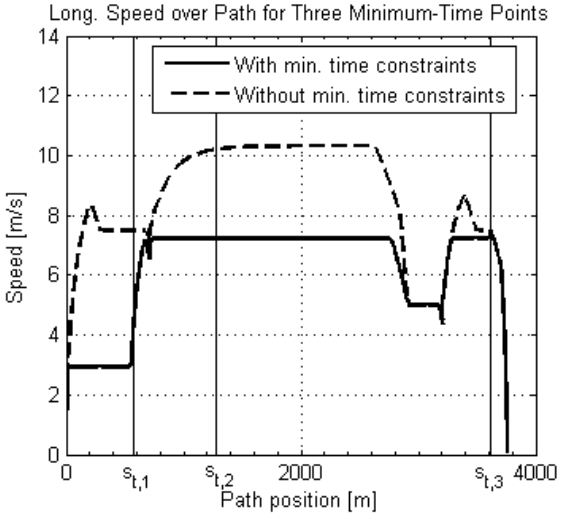

Figure 5.18: **Optimized longitudinal speed over time for the trajectory with three minimum-time points compared with the same trajectory without minimum-time constraints**

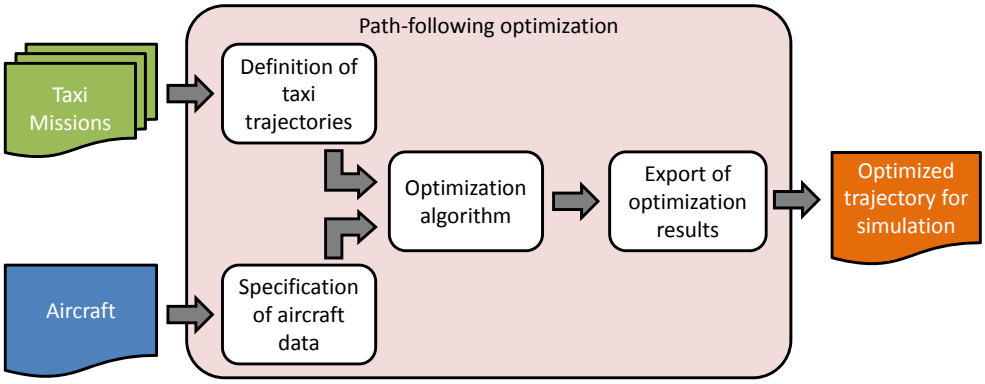

Figure 5.19: **Practical steps for the application of the path-following optimization**

the traveled speed is clearly affected by the first and third waypoint, but not by the second one.

5.6 Application of the Path-Following Optimization Tool

The previous sections of this chapter presented the convex path-following optimization framework used in this work and showed some examples to focus on specific features of the methodology. This section is intended to give some guidelines on how to apply the path-following optimization procedure within the framework of the assessment of electric taxi systems. In this work, the operations described in this section have been implemented in a number of Matlab scripts to enhance the efficiency and the usability of the toolchain.

As explained in Chapter 1, the aims of path-following optimization are to give a first assessment of the ground performance of the taxi system, and to generate off-line driving and steering commands to be used later in the aircraft model control. The operations needed in practice to perform a path-following optimization and obtain the desired results will be illustrated step by step in the following. A schematic illustration of these operations is given in Figure 5.19 for clarity.

5.6.1 Definition of taxi trajectories

The first step consists in discretizing the ground trajectory to be followed and describing it in global coordinates. Each discretized point is defined through its global coordinate pair $\{X, Y\}$; also, the course angle Ψ is given for each point to define the

direction and yaw angle with which the aircraft must pass the waypoint. Thus each waypoint is identified by a vector $[X,\ Y,\ \Psi]$. The waypoint vectors form the discrete trajectory description matrix $\mathbf{p}$ shown in (5.38). The origin of the global reference system – oriented with the x-axis pointing north and the y-axis pointing east – is placed at the starting point s_0 of the trajectory; the initial course Ψ_0 is also given.

A Matlab script was realized for this work that automatically performs the calculations illustrated below and outputs the discrete trajectory description matrix $\mathbf{p}$ needed in the path-following optimization problem. The input of the script is a list with a geometric description of each subsequent trajectory portion (straights with length, curves with length and radius) as well as the speed limit and the discretization step Δs for each portion. Curve transitions are also added automatically as explained below.

A generic trajectory is composed by a sequence of straight and curved sections. A straight section is defined through its length l and its orientation with respect to the North, i.e. the constant course angle $\bar{\Psi}$. After defining an integer number of waypoints $w \in \mathbb{Z}$ in which the straight portion should be divided, the discretization step Δs is calculated as:

$$\Delta s = \frac{l}{w} \tag{5.44}$$

The describing vector of each discrete point can then be calculated sequentially by:

$$\begin{bmatrix} X_k \\ Y_k \\ \Psi_k \end{bmatrix} = \begin{bmatrix} X_{k-1} + \Delta s \cos \Psi_k \\ Y_{k-1} + \Delta s \sin \Psi_k \\ \bar{\Psi} \end{bmatrix} \qquad k = 1, \ldots, w \tag{5.45}$$

where $k = 0$ is the last point of the previous trajectory portion that is linked to the considered straight, or the starting point $[0,\ 0,\ \Psi_0]$ of the trajectory if the considered straight is the first portion of the trajectory.

A curved section is assumed to be composed by a transition from straight to curved path, a constant-radius portion – i.e. a circular arc – and a transition from curved to straight path. Such a section is completely described through the path length of each of the three portions and the curve radius R of the circular arc. Transitions ensure smooth changes in the controlled variables at the interfaces between different trajectory portions. A suitable transition function which is extensively used in civil engineering is the Euler spiral, or clothoid. In the continuous domain, a clothoid transition of length l is defined through a curvature Γ (i.e. the reciprocal of the curve radius R) which is linearly proportional to its arc length:

$$\Gamma(s) = \frac{1}{R} = \underline{\Gamma} + \frac{s}{l}\left(\bar{\Gamma} - \underline{\Gamma}\right) \qquad \text{with } s \in [0, l] \tag{5.46}$$

where $\underline{\Gamma}$ is the curvature at the end of the previous trajectory portion and $\bar{\Gamma}$ is the curvature at the beginning of the next one. The course angle and the global coordinates

Table 5.4: **Values for curve inscription parameters**

Case	$\underline{\Gamma}$	$\bar{\Gamma}$
Initial inscription from straight to curve	0	$1/R$
Final inscription from curve to straight	$1/R$	0

along the transition are:

$$\Psi(s) = \Psi_0 + \int_0^s \Gamma(s')\, ds' = \Psi_0 + \underline{\Gamma} s + \frac{s^2}{2l}\left(\bar{\Gamma} - \underline{\Gamma}\right) \tag{5.47}$$

$$X(s) = X_0 + \int_0^s \cos\Psi(s') s'\, ds' \tag{5.48}$$

$$Y(s) = Y_0 + \int_0^s \sin\Psi(s') s'\, ds' \tag{5.49}$$

with $X_0,\ Y_0,\ \Psi_0$ coordinates and course angle at the beginning of the transition. Transforming these expressions into discrete form, the following is obtained for each waypoint:

$$\begin{bmatrix} X_k \\ Y_k \\ \Psi_k \end{bmatrix} = \begin{bmatrix} X_{k-1} + \Delta s \cos\Psi_k \\ Y_{k-1} + \Delta s \sin\Psi_k \\ \Psi_{k-1} + \Delta s \left[\underline{\Gamma} + \frac{k}{w}\left(\bar{\Gamma} - \underline{\Gamma}\right)\right] \end{bmatrix} \qquad k = 1, \ldots, w \tag{5.50}$$

where $w \in \mathbb{Z}$ is the number of waypoints in which the transition has been discretized, and Δs is calculated for the considered portion through (5.44). The waypoint $k = 0$ is the last point of the previous trajectory portion, or the starting point $[0,\ 0,\ \Psi_0]$ of the trajectory if the considered portion is the first one in the trajectory. The parameters $\underline{\Gamma},\ \bar{\Gamma}$ assume the values listed in table 5.4.

In the constant-radius curve with length l and divided into $w \in \mathbb{Z}$ waypoints, (5.48) and (5.49) still apply, while the course angle is linearly proportional to the traveled distance:

$$\Gamma = \frac{1}{R} \qquad \Psi(s) = \Psi_0 + \int_0^s \Gamma\, ds' = \Psi_0 + \Gamma s \tag{5.51}$$

with Ψ_0 course angle at the beginning of the arc. The discrete equations for each waypoint are therefore:

$$\begin{bmatrix} X_k \\ Y_k \\ \Psi_k \end{bmatrix} = \begin{bmatrix} X_{k-1} + \Delta s \cos\Psi_k \\ Y_{k-1} + \Delta s \sin\Psi_k \\ \Psi_{k-1} + \Delta s\, \Gamma \end{bmatrix} \qquad k = 1, \ldots, w \tag{5.52}$$

As for the other portion types, the waypoint $k = 0$ is either the last point of the previous trajectory portion or the starting point $[0,\ 0,\ \Psi_0]$ of the trajectory if the constant-radius curve is the first portion in the trajectory.

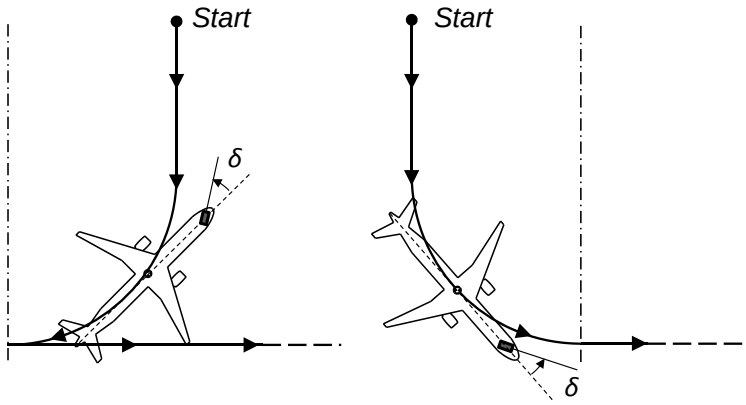

Figure 5.20: **Conversion of pushback trajectory into an equivalent forward driven trajectory by mirroring around the marked axis (dashed-dotted line). Note that the steering direction remains unchanged.**

As shown in Section 5.4.2, a speed limit vector $\tilde{\mathbf{v}}_{\mathbf{x}} = [\tilde{v}_{x,0}, \ldots, \tilde{v}_{x,n}]$ can be defined. It contains the upper bound of the longitudinal speed for each waypoint. For example, corners normally need to be negotiated at lower speeds for safety. A suitable limit (usually 5 to 10 m/s) should therefore be set on all the corner waypoints.

It is important to remember that the discussed convex optimization problem does not accept negative or zero speeds (see Section 5.3.7). These cases need to be handled as follows.

Zero speed A planned stop at a certain waypoint needs to be replaced by a small positive speed limit at that waypoint such as 0.1 m/s.

Negative speed These parts of a trajectory need to be driven on at positive speeds. Backward driving normally occurs during pushback in taxi-out. For the path-following optimization, it is necessary to build an equivalent taxi-out trajectory that will be traveled on at positive speeds, while corners still are oriented in the same steering direction. This results in a mirroring of the backwards driven trajectory around an axis passing through the point where the direction is changed and perpendicular to the forward driven trajectory portion in that point, as shown in Figure 5.20. The speed limit constraints need to be changed in sign accordingly. At the end of pushback, a quasi-zero speed limit needs to be set to approximate the stop and subsequent change of driving direction.

5.6.2 Specification of aircraft data and constraints

The next operation is to input all the numeric parameters needed for the optimization. The first group of quantities concerns the aircraft geometry and dynamics:

- aircraft mass m;
- aircraft moment of inertia around the yaw axis J_z;
- effective radius R_R of the main landing gear wheels. This is the distance between the wheel axis and the ground surface as influenced by the tire deflection under the vertical load;
- the projections b_f, b_r onto a xy-plane of the distances between the center of gravity and the wheel axis of the nose and main gear wheels respectively (see Figure 5.1);
- the distance a_r between the aircraft longitudinal axis and the plane of the (motorized) main landing gear (see Figure 5.1);
- the cornering stiffnesses c_f, c_r of the nose and main gear wheels respectively as well as the tire saturation forces $F_{yf,max}, F_{yr,max}$;
- the coefficient μ_R of rolling resistance of the tires;
- the idle fuel consumption of the APU c_0 and the fuel flow to power ratio c_1. Setting these parameters requires some knowledge about the performance of the aircraft APU.

Another set of quantities is needed to characterize the electric taxi system:

- the maximum torque T_{max} of the electric motors;
- the parameters b_P, k_P introduced in (5.30) to approximate the motor power limitation. They should be chosen so that the approximation is particularly good around the predicted operating points of the motors.

Because the convex optimization framework is based on a number of approximations, it is suggested to set values slightly lower than the real system capabilities in order to leave some margin for error correction in the subsequent simulation phases in the toolchain.

If a thermal constraint needs to be considered, the parameter $E_{h,max}$ introduced in (5.32) needs to be set. Since this parameter is not explicitly a heat quantity with the dimensionality of an energy, its value needs to be determined indirectly, for example by assessing the optimization results with a thermal motor model, predicting critical temperatures within the motors and observing their behavior in dependence of $E_{h,max}$. Because this constraint approximates the overall heat production over the trajectory, the value of $E_{h,max}$ resulting in a certain maximum temperature will show a strong dependence on the trajectory length.

5.6.3 Performing the optimization

When the setup is completed, the optimization problem can be solved. As mentioned in Section 5.4.1, the convex optimization tool CVX [3] with the SDPT3 numerical solver [81] were used in the Matlab environment [9] in the course of the present work. In general however, any optimization software can be used that is able to take advantage of the convexity of the problem formulation for a faster convergence. How the problem data should be passed, whether in form of code or through a graphic user interface, is specific for the chosen software.

5.6.4 Exporting the optimization data

After a solution is found, the results are prepared for export to the next steps of the toolchain. The following procedure was implemented in a Matlab script in this work.

Firstly, a vector is built containing the distances of all waypoints from the trajectory origin measured along the path, i.e. their path positions. Because all results are defined as a function of the path position, this vector containing the values of the independent variable is needed in the later simulation as an input. For each waypoint, this is equivalent to the summation of all the discretized steps Δs_i along the trajectory from the start to that waypoint:

$$\mathbf{d} = \begin{bmatrix} d_1 \\ d_2 \\ \vdots \\ d_k \\ \vdots \\ d_n \end{bmatrix} = \begin{bmatrix} 0 \\ d_1 + \Delta s_1 \\ \vdots \\ d_{k-1} + \Delta s_{k-1} \\ \vdots \\ d_{n-1} + \Delta s_{n-1} \end{bmatrix} \tag{5.53}$$

Then, the following vectors are saved for subsequent export:

- the above distance vector $\mathbf{d}$;
- the vector $\mathbf{\Psi}$ of course angles at each waypoint. It is the third column in the trajectory matrix $\mathbf{p}$ in (5.38);
- the vector $\mathbf{v}_x$ of longitudinal speeds at each waypoint:

$$\mathbf{v}_x = \begin{bmatrix} v_{x,1} \\ \vdots \\ v_{x,k} \\ \vdots \\ v_{x,n} \end{bmatrix} = \begin{bmatrix} \sqrt{b_1} \\ \vdots \\ \sqrt{b_k} \\ \vdots \\ \sqrt{b_n} \end{bmatrix} \tag{5.54}$$

- the vectors $\mathbf{T}_l, \mathbf{T}_r$ of the motor moments at each waypoint;
- the vector δ of the steering angle at each waypoint.

The special cases with non-positive speeds discussed in Section 5.6.1 also result in additional tasks during the export of the results.

Zero speed Remind that for the waypoints where the aircraft is supposed to stop, a small speed limit such as 0.1 m/s was set upon trajectory definition. An additional piece of information is needed for the subsequent toolchain steps whether the aircraft should be stopped at those waypoints; also, the stop duration needs to be defined since the optimization results are a function of the path variable, hence they cannot contain any time-based information. For the former issue, a boolean flag is introduced for each waypoint assuming the value *true* if the aircraft needs to be stopped at that waypoint, and *false* elsewhere. For consistency, *true* values should only be assigned for waypoints subject to the small speed limit mentioned. All waypoint flags are summarized in a vector and exported. For the stopping times, data on the duration of each stop need to be made available, for example in form of a table.

Negative speed The trajectory portions where backward driving takes place were mirrored upon trajectory definition and traveled on with positive speeds. This results in opposite signs for the motor torques. Consequently, the affected parts of the vectors $\mathbf{T}_l, \mathbf{T}_r$ need to be changed in sign. Clearly, this also applies to the affected parts of the speed vector $\mathbf{v}_x$. Note that the mirroring did not affect the steering angle, thus no change is needed on the steering angle vector δ.

5.7 Summary

This chapter illustrated the generation of optimal path-following data based on a convex problem formulation. Starting from a three-wheeled vehicle model representing the aircraft on ground, the dynamic equations in the global reference system were derived (Section 5.1). The path-following optimization problem has then been formulated as a function of the path variable along the trajectory (Section 5.3). Elements of the problem such as the electric driving system and especially the APU have been modeled in convex form too and integrated into the optimization problem. A method for integrating thermal constraints has been presented in Section 5.3.5 by indirectly limiting the amount of heat produced by the motors. Two cost functions were presented in Section 5.3.6: time minimization and fuel consumption minimization in the APU.

Having defined the problem completely, a discretization was performed (Section 5.4) and the problem was solved for a sample trajectory. The effect of different cost functions with and without thermal limits was shown. A significant result was the very small difference in travel time and fuel consumption when comparing the op-

timizations based on the different cost functions (Section 5.4.3). It is concluded that due to the high APU idle consumption and the relatively small amount of fuel used for power generation, a consumption minimizing driving strategy is only marginally different from a time minimizing one.

Constraining the time required to pass a waypoint was discussed in Section 5.5. The discussion focused in particular on minimum times that need to have elapsed from the start in order to clear the considered waypoints. A method to include minimum-time constraints into the convex problem in an approximate form was presented. An iterative algorithm was realized to find the related constraint parameters.

Finally, considerations of practical nature about using the convex path-following optimization were discussed in Section 5.6. In particular, Section 5.6.1 described how to discretize generic taxi trajectories and how to deal with limitations of the adopted problem formulation such as strictly positive speeds. The aircraft and system data needed for the problem definition were summarized in Section 5.6.2. The data from the optimization results that need to be treated and saved for the subsequent steps of the toolchain were listed in Section 5.6.4.

6 Ground Controller for Path Following

This chapter discusses the development of a ground controller for the model-based path following of taxi trajectories. Within the general strategy of the work described in Chapter 1, model-based simulation is used to determine the performances of the electric taxi system. The aircraft commands and kinematic quantities that have been calculated through the convex optimization algorithm are used as inputs of the aircraft model during simulation. A number of reasons prevents the aircraft model from following the assigned path precisely, such as modeling and parameter uncertainties caused by the approximations and simplifications introduced in the model used in the convex optimization problem. For this reason, feedback control is necessary to eliminate the tracking error during the path following simulation. The aircraft ground motion will be governed by the sum of feed-forward commands calculated with the offline optimization and feedback commands dependent on the errors between the actual and the desired position. The control design task will be performed concretely on a narrow-body aircraft with characteristics shown in Table 6.1, which is consistent with the aircraft type used throughout the present work.

Beside stability and robustness, the ground controller should guarantee a similar tracking performance in the whole operating envelope to allow a sound comparison of different aircraft and system architectures.

In order to tune and analyze the behavior of the motion controller, the simplified nonlinear dynamic model of the aircraft on ground (5.1), (5.2), (5.3) already used in the definition of the convex optimization problem will be considered.

The longitudinal and lateral error will be controlled by two independent feedback loops, as illustrated in the following.

Table 6.1: **Parameters of aircraft considered in the development of the ground controller**

Parameter	Symbol	Value
Maximum Take-Off Weight (MTOW)	m	73,500 kg
Operating Empty Weight (OEW)		41,100 kg
Inertia coeff. around z-axis	J_z	$3.78 \cdot 10^6$ kg $\cdot$ m^2
Main gear y-distance	a	3.795 m
Main gear x-distance	b_h	2.51 m
Nose gear x-distance	b_f	10.19 m
Cornering stiffness of nose gear	c_f	$1.49 \cdot 10^5$ N/rad
Cornering stiffness of main gear	c_r	$4.00 \cdot 10^5$ N/rad
Coefficient of quadratic motion resistance	k_{aero}	1.297 N $\cdot$ s^2/m^2
Effective main gear wheel radius	R_R	0.5198 m
Reference speed for longitudinal control	$\bar{v}_x$	5 m/s

6.1 Longitudinal Controller

6.1.1 Model of longitudinal error dynamics

The longitudinal tracking error, i.e. the tracking error in the tangent direction to the trajectory path, is defined as:

$$e_{long} = s(t) - s_{des}(t) \tag{6.1}$$

being $s(t)$ the path coordinate along the trajectory and $s_{des}(t)$ its commanded value at the time t. It is assumed that the sideslip angle β is small, hence the lateral component of the motion is neglected in the tracking of the longitudinal error. As a consequence, the aircraft longitudinal axis is always tangent to the path and the following holds: $\dot{s}(t) \approx v_x(t)$. With an analogy, the derivative of the commanded path coordinate is taken as the commanded longitudinal speed: $\dot{s}_{des}(t) \approx v_{x,des}(t)$. The longitudinal tracking error and its first and second derivative therefore become:

$$\begin{aligned} e_{long} &= s(t) - s_{des}(t) && (6.2)\\ \dot{e}_{long} &= v_x(t) - v_{x,des}(t) && (6.3)\\ \ddot{e}_{long} &= \dot{v}_x(t) - \dot{v}_{x,des}(t) && (6.4) \end{aligned}$$

Regarding the longitudinal dynamics (5.1), resistances F_{res} of the following form are considered:

$$F_{res} = \mu_R \cdot mg + k_{aero} v_x^2 \tag{6.5}$$

This includes one constant term caused by the rolling resistance and one quadratic term caused by aerodynamic resistances.

6.1.2 Design of the longitudinal controller

To ensure both fast reaction and suppression of the longitudinal error even in presence of uncertainties, a linear proportional-integral-derivative (PID) feedback controller is chosen:

$$T_{fb} = k_d \dot{e}_{long} + k_p e_{long} + k_i \int_0^t e_{long}\, dt \tag{6.6}$$

To design this controller, the longitudinal dynamics (5.1) will be linearized around a reference speed $\bar{v}_x > 0$. The term v_y is neglected, reminding of the assumption of small sideslip angle, as well as the effect of the steering angle on the longitudinal dynamics. Also, it is assumed that the feedback controller will act on both wheel motors with the same effort; hence the motor torques $T_l + T_r$ are substituted by their sum $T = T_l + T_r$. The linearized longitudinal dynamics therefore become:

$$\dot{v}_x = -\frac{1}{m} \left.\frac{dF_{res}}{dv_x}\right|_{\bar{v}_x} v_x + \frac{1}{mR_R} T \tag{6.7}$$

Substituting (6.3) and (6.4), the expression for the longitudinal error dynamics is found:

$$\ddot{e}_{long} = -\frac{1}{m} \left.\frac{dF_{res}}{dv_x}\right|_{\bar{v}_x} (\dot{e}_{long} + v_{x,des}) - \dot{v}_{x,des} + \frac{1}{mR_R} T \tag{6.8}$$

The state-space form of the longitudinal error dynamics is as follows:

$$\begin{aligned} \begin{bmatrix} \ddot{e}_{long} \\ \dot{e}_{long} \end{bmatrix} &= \begin{bmatrix} -\frac{1}{m} \left.\frac{dF_{res}}{dv_x}\right|_{\bar{v}_x} & 0 \\ 1 & 0 \end{bmatrix} \begin{bmatrix} \dot{e}_{long} \\ e_{long} \end{bmatrix} + \\ &+ \begin{bmatrix} \frac{1}{mR_R} & -1 & -\frac{1}{m} \left.\frac{dF_{res}}{dv_x}\right|_{\bar{v}_x} \\ 0 & 0 & 0 \end{bmatrix} \begin{bmatrix} T \\ \dot{v}_{x,des} \\ v_{x,des} \end{bmatrix} \end{aligned} \tag{6.9}$$

The eigenvalues of the dynamic matrix are:

$$\det\left(\begin{bmatrix} -\frac{1}{m} \left.\frac{dF_{res}}{dv_x}\right|_{\bar{v}_x} & 0 \\ 1 & 0 \end{bmatrix} - \lambda \mathbf{I} \right) = \lambda \left(\left.\frac{dF_{res}}{dv_x}\right|_{\bar{v}_x} + \lambda \right) \tag{6.10}$$

$$\lambda_1 = 0 \qquad \lambda_2 = -\left.\frac{dF_{res}}{dv_x}\right|_{\bar{v}_x} \tag{6.11}$$

Note that λ_2 is always ≤ 0 due to the definition of F_{res} in (6.5). λ_2 is a stable eigenvalue, while λ_1 can be stabilized by an appropriate feedback controller.

The parameters k_d, k_p, k_i of the PID controller were calculated automatically by means of the *Matlab Control Toolbox* functions by requiring a crossover frequency of

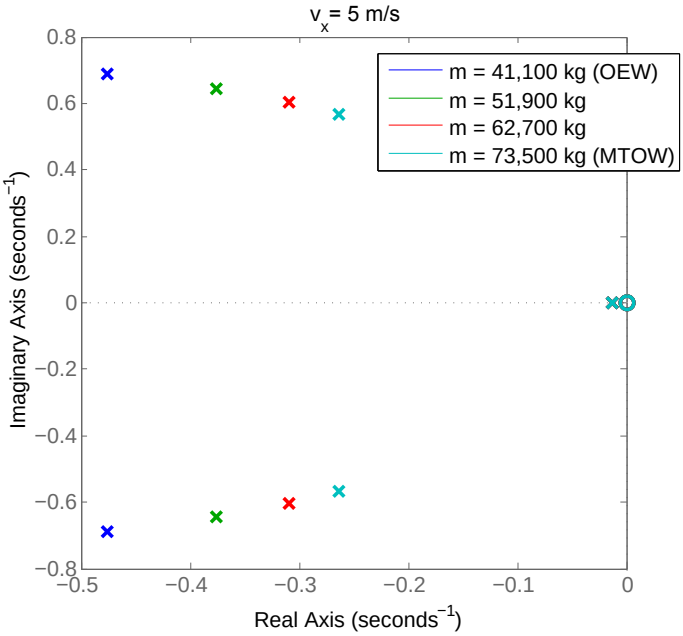

Figure 6.1: **Pole-zero map of the closed-loop longitudinal dynamics at speed of 5 m/s and mass variation between OEW and MTOW**

0.75 rad/s and a phase margin of 45 degrees. For an aircraft with the data reported in Table 6.1, following controller gains result:

$$\begin{bmatrix} k_d \\ k_p \\ k_i \end{bmatrix} = \begin{bmatrix} 20,600 \\ 15,200 \\ 196 \end{bmatrix} \tag{6.12}$$

6.1.3 Robustness of longitudinal controller

The robustness of the longitudinal controller to modeling uncertainties is now verified by simulation with the linearized model of longitudinal motion (6.7) as plant, for different operating speeds and for an aircraft mass in the range between Operating Empty Weight (OEW) and Maximum Take-Off Weight (MTOW).

Considering the aircraft mass variation, Figure 6.1 shows the closed-loop pole-zero plot for varying mass in the interval between Maximum Take-Off Weight (MTOW) and Operating Empty Weight (OEW) at the speed of 5 m/s. It can be seen that the poles move further towards the left with decreasing aircraft mass, thus improving stability and responsiveness. Figure 6.3 shows the closed-loop Bode plot of the sensitivity function for varying mass from OEW to MTOW at the speed of 5 m/s. With reference

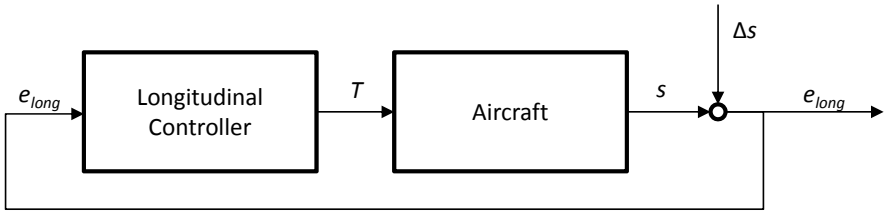

Figure 6.2: **Closed-loop diagram of the longitudinally controlled aircraft on ground**

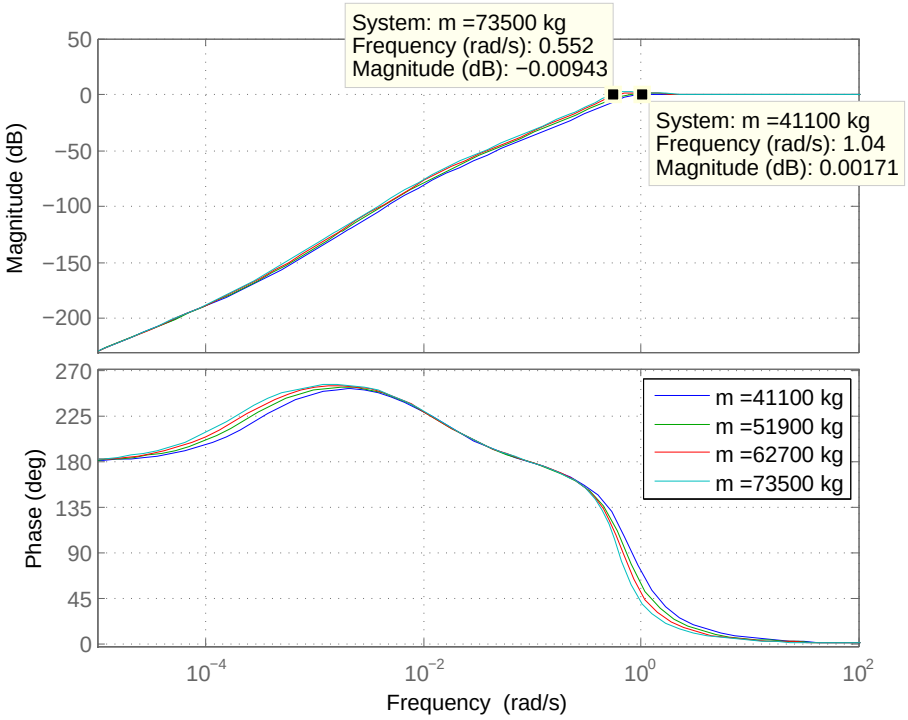

Figure 6.3: **Bode diagram of the sensitivity function (transfer function from Δs to e_{long}) for varying aircraft mass at speed of 5 m/s**

to the closed-loop system in figure 6.2, the sensitivity function is the transfer function from a change Δs in the reference path position to the longitudinal error e_{long}. Its Bode plot confirms the improved responsiveness: the crossover frequency of the error rejection is increased with decreasing mass, ranging from 0.55 rad/s for MTOW to 1.04 rad/s for OEW.

The effect of system linearization is assessed by plotting the Bode plot of the sensitiv-

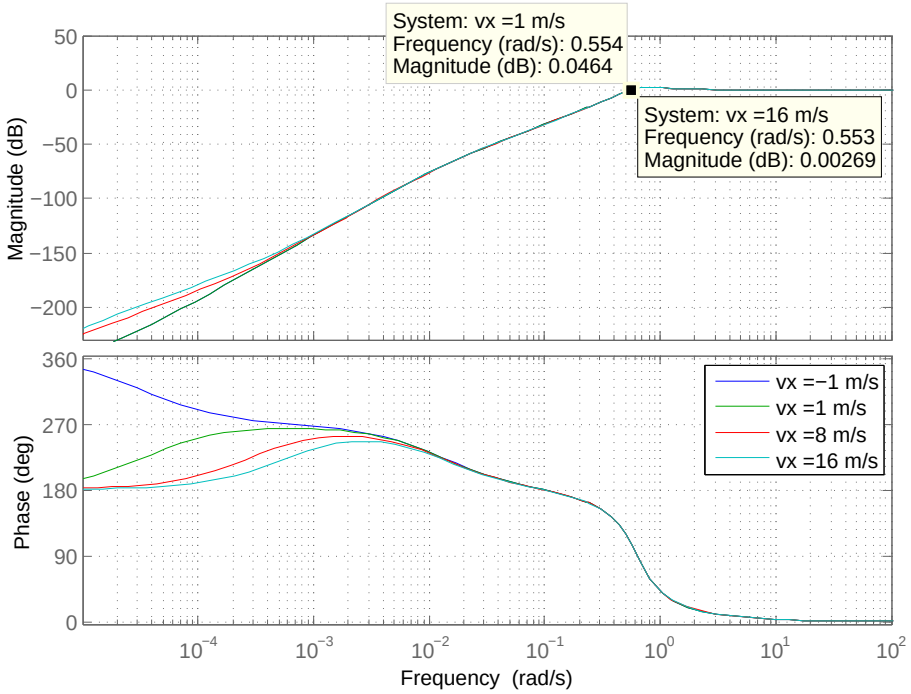

Figure 6.4: **Bode diagram of the sensitivity function (transfer function from Δs to e_{long}) for aircraft speeds of -1, 1, 8, and 16 m/s at Maximum Take-Off Weight**

ity function for speeds of -1, 1, 8, and 16 m/s, at MTOW and with all other parameters at their nominal value. As can be seen in Figure 6.4, the plots are very similar in the four cases; the crossover frequency of the sensitivity function barely changes with varying speeds, ranging from 0.553 to 0.554 rad/s. This indicates that the system is only very mildly nonlinear and the linearized system is a very good approximation; the designed longitudinal controller vastly retains its performance.

6.2 Lateral Controller

6.2.1 Model of lateral error dynamics

We define the course error as:

$$e_\psi = \psi_{des} - \psi \tag{6.13}$$

being ψ_{des} the desired course and ψ the actual course at each time instant. With reference to Figure 6.5 and assuming a small course error, the position error in the

perpendicular direction to the trajectory can be defined through its derivative as:

$$\dot{e}_{lat} = -v_y + v_x e_\psi \tag{6.14}$$

with v_x and v_y longitudinal and lateral speed in the aircraft-fixed reference frame. v_x is assumed to vary much more slowly than the lateral dynamics, hence it is taken constant, i.e. $\dot{v}_x \approx 0$. The following equations are derived from the error definitions:

$$\ddot{e}_\psi = \ddot{\psi}_{des} - \ddot{\psi} \tag{6.15}$$

$$\ddot{e}_{lat} = -\dot{v}_y + v_x \dot{e}_\psi + \dot{v}_x e_\psi \approx -\dot{v}_y + v_x \dot{e}_\psi \tag{6.16}$$

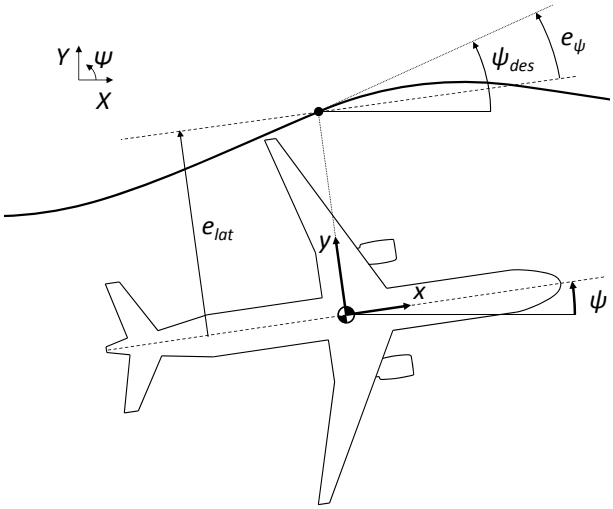

Figure 6.5: **Definition of lateral and course error for lateral motion control**

Rearranging these equations for $\ddot{\psi}$ and $\dot{v}_y$ and substituting into (5.2) and (5.3), the aircraft dynamic equations for the lateral dynamics and for the yaw dynamics can be written as function of the defined errors:

$$\ddot{e}_{lat} = v_x \dot{\psi}_{des} - \frac{1}{m} F_y \tag{6.17}$$

$$\ddot{e}_\psi = \ddot{\psi}_{des} - \frac{1}{J_z} M_z \tag{6.18}$$

These dynamic equations will now be linearized around the equilibrium point $\{v_x = \bar{v}_x,\ v_y = 0,\ \delta = 0,\ \psi = 0,\ \dot{\psi} = 0\}$. The tire forces (5.4) are considered only in their linear part, i.e.:

$$F_{yf} = c_f \alpha_f \tag{6.19}$$

$$F_{yi} = c_r \alpha_i \quad \text{with} \quad i = \{l, r\} \tag{6.20}$$

where c_f, c_r are the front respectively rear tire cornering stiffness and $\alpha_f, \alpha_l, \alpha_r$ are the sideslip angles of the front, rear left and rear right tire respectively as calculated in (5.5). Also, differential motor torques are neglected, i.e. $T_l \approx T_r \; \forall t$. Substituting (6.20) into (6.16) and linearizing, the following system is obtained:

$$\begin{bmatrix} \ddot{e}_{lat} \\ \dot{e}_{lat} \\ \ddot{e}_{\psi} \\ \dot{e}_{\psi} \end{bmatrix} = \mathbf{A} \begin{bmatrix} \dot{e}_{lat} \\ e_{lat} \\ \dot{e}_{\psi} \\ e_{\psi} \end{bmatrix} + \mathbf{B}_1 \delta + \mathbf{B}_2 \begin{bmatrix} \ddot{\psi}_{des} \\ \dot{\psi}_{des} \end{bmatrix} \tag{6.21}$$

$$\mathbf{A} = \begin{bmatrix} -\frac{1}{m}\left(\frac{c_f}{v_x} + c_r S_{v_y}\right) & 0 & -\frac{1}{m}\left(\frac{b_f c_f}{v_x} + c_r S_{\dot{\psi}}\right) & \frac{1}{m}\left(c_f + v_x c_r S_{v_y}\right) \\ 1 & 0 & 0 & 0 \\ \frac{1}{J_z}\left(-\frac{b_f c_f}{v_x} + b_h c_r S_{v_y}\right) & 0 & \frac{1}{J_z}\left(-\frac{b_f^2 c_f}{v_x} + b_r c_r S_{\dot{\psi}}\right) & \frac{1}{J_z}\left(b_f c_f - v_x b_r c_r S_{v_y}\right) \\ 0 & 0 & 1 & 0 \end{bmatrix}$$

$$\mathbf{B}_1 = \begin{bmatrix} -\frac{c_f}{m} \\ 0 \\ -\frac{b_f c_f}{J_z} \\ 0 \end{bmatrix} \qquad \mathbf{B}_2 = \begin{bmatrix} 0 & v_x + \frac{1}{m}\left(\frac{b_f c_f}{v_x} + c_r S_{\dot{\psi}}\right) \\ 0 & 0 \\ 1 & \frac{1}{J_z}\left(\frac{b_f^2 c_f}{v_x} - b_r c_r S_{\dot{\psi}}\right) \\ 0 & 0 \end{bmatrix}$$

$$\begin{aligned} S_{v_y} &= \frac{\partial}{\partial v_y}\left(\frac{v_y - b_r\dot{\psi}}{v_x - a_r\dot{\psi}} + \frac{v_y - b_r\dot{\psi}}{v_x + a_r\dot{\psi}}\right)\Bigg|_{\substack{v_x = \bar{v}_x \\ v_y = 0, \dot{\psi} = 0}} \\ S_{\dot{\psi}} &= \frac{\partial}{\partial \dot{\psi}}\left(\frac{v_y - b_r\dot{\psi}}{v_x - a_r\dot{\psi}} + \frac{v_y - b_r\dot{\psi}}{v_x + a_r\dot{\psi}}\right)\Bigg|_{\substack{v_x = \bar{v}_x \\ v_y = 0, \dot{\psi} = 0}} \end{aligned}$$

The influence of the longitudinal speed v_x in the system dynamics is obvious as it appears in most elements of the system matrices. Note that the quantities S_{v_y} and $S_{\dot{\psi}}$ are also dependent on v_x. Therefore, unlike the longitudinal case, the system must be regarded as a Linear Parameter Varying (LPV) system with $\bar{v}_x$ as parameter.

6.2.2 Design of the lateral controller

A gain-scheduled state feedback controller is proposed to stabilize the system in (6.21). The controller will act on the steering input δ, while $\ddot{\psi}_{des}$ and $\dot{\psi}_{des}$ will be considered as disturbances.

Because of the effect of the inputs $\ddot{\psi}_{des}$ and $\dot{\psi}_{des}$, the steady-state errors would not tend to zero during cornering (i.e. for $\ddot{\psi}_{des}, \dot{\psi}_{des} \neq 0$); integral control is required for this purpose [57]. Therefore, the dynamic system (6.21) is augmented with the additional state $\sigma_{lat} = \int_0^t e_{lat}\, d\tau$ as follows:

$$\dot{\mathbf{e}} = \bar{\mathbf{A}}\mathbf{e} + \bar{\mathbf{B}}_1\delta + \bar{\mathbf{B}}_2 \begin{bmatrix} \ddot{\psi}_{des} \\ \dot{\psi}_{des} \end{bmatrix} \tag{6.22}$$

$$\text{with} \qquad \mathbf{e} = \begin{bmatrix} \dot{e}_{lat} \\ e_{lat} \\ \dot{e}_{\psi} \\ e_{\psi} \\ \sigma_{lat} \end{bmatrix} \qquad \bar{\mathbf{A}}\left(\bar{v}_x\right) = \begin{bmatrix} \mathbf{A}\left(\bar{v}_x\right) & \mathbf{0} \\ \mathbf{a}_{\sigma_{lat}} & 0 \end{bmatrix} \qquad \mathbf{a}_{\sigma_{lat}} = [0 \quad 1 \quad 0 \quad 0]$$

$$\bar{\mathbf{B}}_1\left(\bar{v}_x\right) = \begin{bmatrix} \mathbf{B}_1\left(\bar{v}_x\right) \\ 0 \end{bmatrix} \qquad \bar{\mathbf{B}}_2\left(\bar{v}_x\right) = \begin{bmatrix} \mathbf{B}_2\left(\bar{v}_x\right) \\ \mathbf{0} \end{bmatrix}$$

Using the parameter values for the aircraft in Table 6.1, it can be verified that the controllability matrix $\left[\bar{\mathbf{B}}_1 \ \bar{\mathbf{A}}\bar{\mathbf{B}}_1 \ \bar{\mathbf{A}}^2\bar{\mathbf{B}}_1 \ \ldots \ \bar{\mathbf{A}}^5\bar{\mathbf{B}}_1\right]$ has full row rank of 5 for every $\bar{v}_x \neq 0$. This means that the lateral dynamics is controllable by acting only on the steering input δ as long as the vehicle is moving.

The state feedback law is then defined as:

$$\delta = -\mathbf{K}_{\bar{v}_x}\mathbf{e} \tag{6.23}$$

where $\mathbf{K}_{\bar{v}_x}$ is a vector of coefficients, identified for each given longitudinal speed $\bar{v}_x$, such that the poles of the closed loop system:

$$\dot{\mathbf{e}} = \left(\bar{\mathbf{A}}\left(\bar{v}_x\right) - \bar{\mathbf{B}}_1\left(\bar{v}_x\right)\mathbf{K}_{\bar{v}_x}\right)\mathbf{e} \tag{6.24}$$

lie in desired locations. For this application, a very low overshoot under 1% is desired. For the aircraft described in table 6.1 at MTOW, the poles have been placed heuristically at [-.75+.5i, -.75-.5i, -1.5,-3, -4]. The dominant complex pair of poles have a natural frequency of 0.901 rad/s and a damping coefficient of 0.832, which result in a step response overshoot of 0.90%. The remaining poles have been put further left on the complex plane in order to generate an approximate second-order closed-loop system behavior, although not too far left to avoid too demanding control action. For each longitudinal speed $\bar{v}_x$ in the set:

$$\bar{v}_x \in [-2, -1, -.5, .5, 1, 2, 4, 6, 8, 10, 12, 14, 16]$$

the appropriate set of vectors $\mathbf{K}_{\bar{v}_x}$ is calculated to obtain the required closed-loop poles. The concrete calculation can be performed with an appropriate software such as the Matlab Control System Toolbox [8]. The final gain-scheduled state feedback control law as a continuous function of the momentary longitudinal speed v_x is given by:

$$\delta = -\mathbf{K}\left(v_x\right)\mathbf{e} \tag{6.25}$$

where the controller coefficient vector $\mathbf{K}\left(v_x\right)$ is obtained through piecewise linear interpolation of the set of $\mathbf{K}_{\bar{v}_x}$.

6.2.3 Robustness of lateral controller

The aircraft mass, the moment of inertia around the z-axis and the tire cornering stiffnesses exert a large influence on the lateral dynamics. The robustness of the closed-loop system to those uncertainties is verified in the following.

Robustness to mass and inertia variations

Figure 6.6 shows how the closed-loop poles of the controlled lateral dynamics move on the complex plane at speeds of -1, 1, 8, and 16 m/s as the mass is varied between OEW and MTOW (see Table 6.1) and all other parameters are kept at their nominal value. The moment of inertia was varied linearly proportionally to the mass variation. A displacement of the center of gravity was not taken into account. As is clear from the diagram, all poles remain in the left half of the complex plane, thus the closed-loop lateral dynamics remain stable in spite of mass variation.

Robustness to cornering stiffness variations

For this test, the cornering stiffness of both the nose and the main gear tires was varied simultaneously between 40 and 120% of the nominal value reported in Table 6.1, while all other parameters were kept at their nominal value. Figure 6.7 shows the behavior of the closed-loop poles of the controlled lateral dynamics at speeds of -1, 1, 8, and 16 m/s as the cornering stiffness is varied. The closed-loop lateral dynamics remain stable in the observed range as all poles remain in the left half of the complex plane. However, it can be noted that the dominant poles wander towards the imaginary axis as the cornering stiffness decreases, especially at the higher speeds. This agrees with the expectation that stability will be lost once very slippery ground conditions reduce the cornering stiffness excessively.

6.3 Implementation of Ground Control in Aircraft Model

This section discusses the integration of the controllers designed above into the Modelica aircraft model.

6.3.1 Path-following data reader and feed-forward controller

This part of the controller is illustrated in figure 6.8. It reads the data from the path-following optimization that were prepared in Section 5.6.4 with the current aircraft

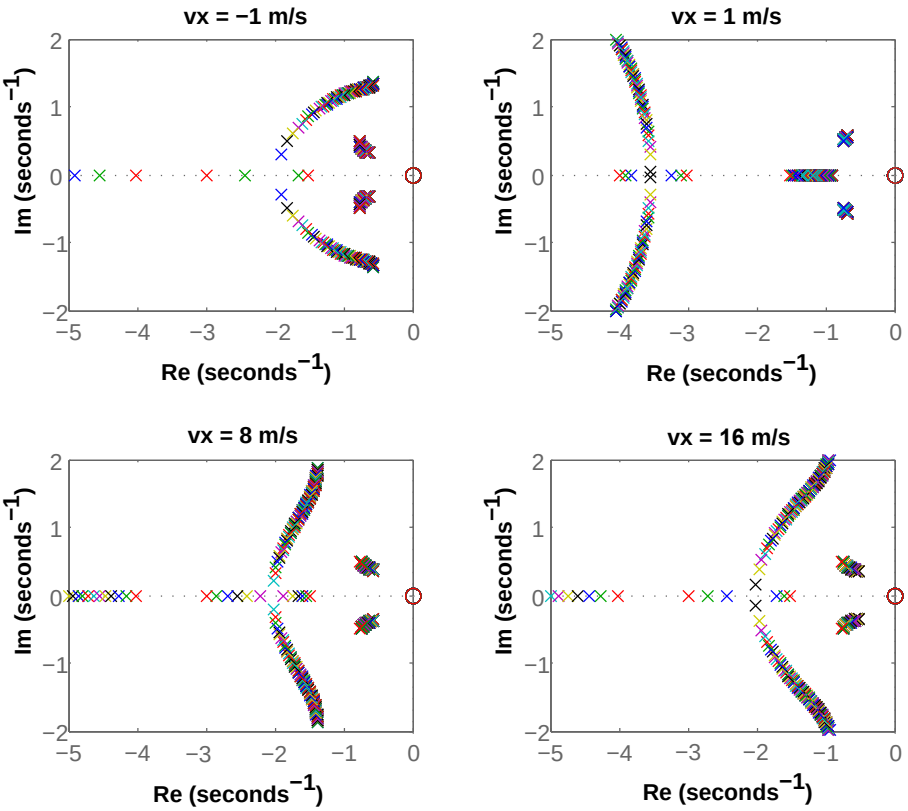

Figure 6.6: **Closed-loop pole-zero maps for lateral control at selected speeds and mass variation between OEW and MTOW. Only the diagram portions for the real range [-5, 0] are shown for clarity.**

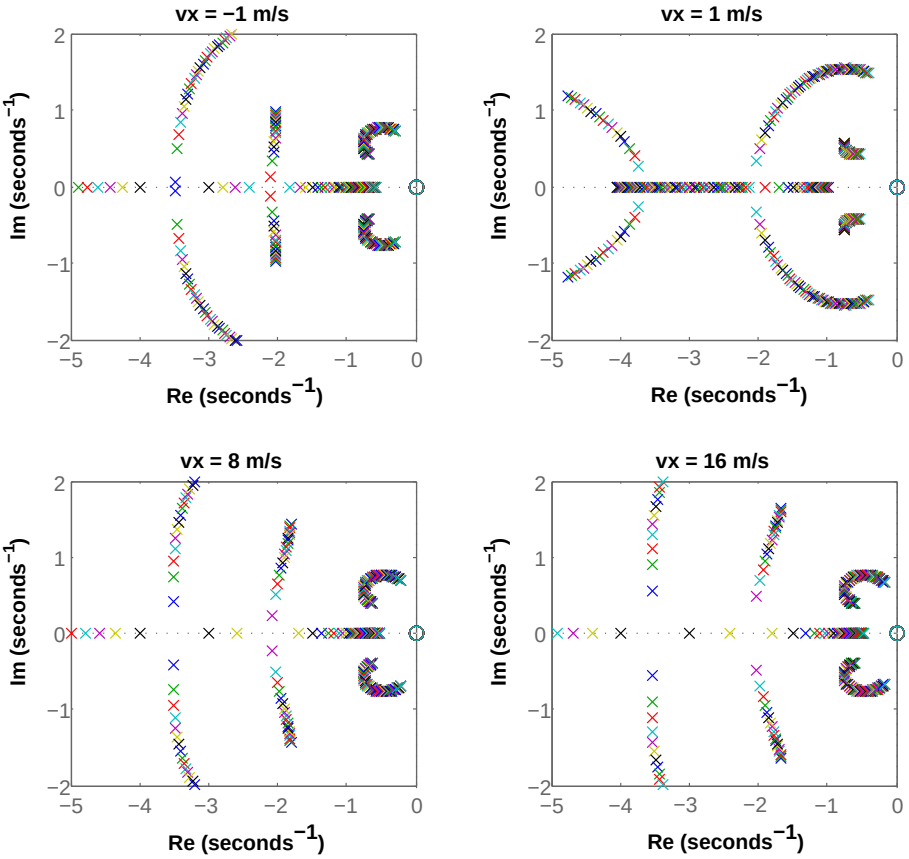

Figure 6.7: **Closed-loop pole-zero maps for lateral control at selected speeds and cornering stiffness variation between 40 and 120% of the nominal value. Only the diagram portions for the real range [-5, 0] are shown for clarity.**

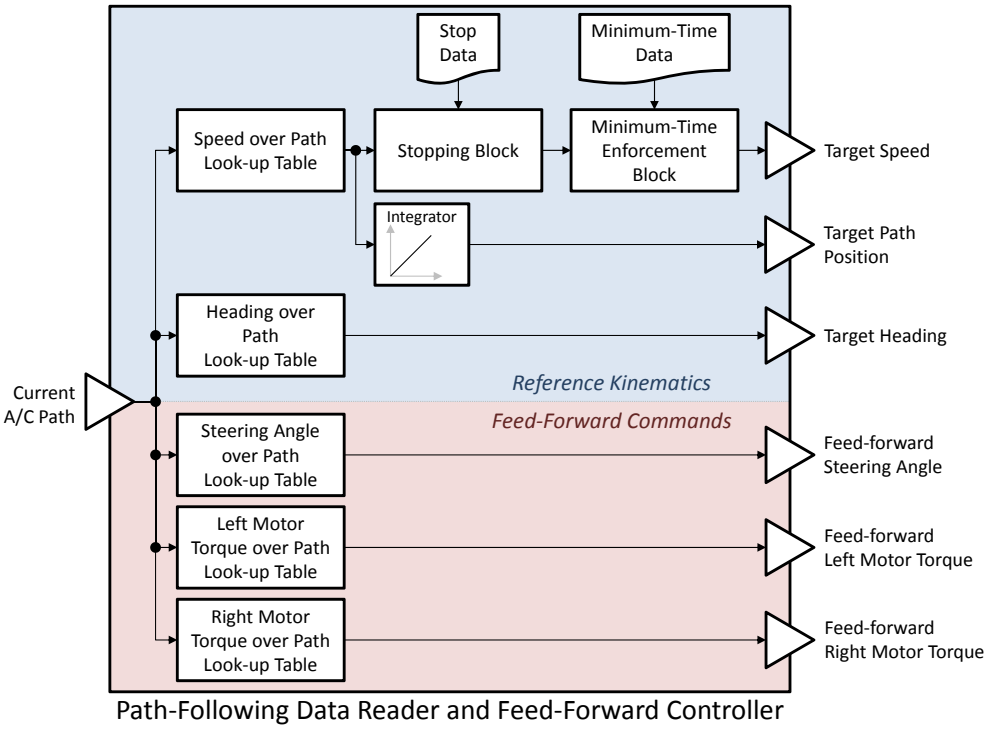

Figure 6.8: **Diagram of the path-following data reader and feed-forward controller block**

path position as input of appropriate look-up tables, interpolates them to continuous signals, and outputs them to the next blocks. More precisely, two basic tasks are performed in parallel. The first task is to assign the actuator commands as calculated in the path-following optimization in feed-forward. The second task is to provide the commanded kinematics, which are needed to compute the position error of the aircraft, in each time instant. The longitudinal speed and the course angle as function of the current path position are already available in the data set saved at the end of the path-following optimization (see Section 5.6.4). Additionally, the desired path position along the trajectory is computed by integrating the desired speed over the simulation time.

An algorithm is needed to handle stops along the trajectory, because position-based signals do not contain any time-based information. As the aircraft is stopped due to a zero speed command, the path position input will remain constant and the data outputs will in turn remain constant too, thus blocking the path-following simulation. The *stopping block* detects the positions and durations of the stops as contained in the path-following optimization data, keeps the commanded speed at zero for the whole duration of the stop, then assigns a small non-zero speed command to start the aircraft

again for a short time before switching back to the path-based commanded speeds.

Another algorithm contained in the *minimum-time enforcing block* ensures that the minimum waypoint passing times (if provided) are respected. For each waypoint, the remaining path distance and remaining time to the allowed passing moment are considered. Below a certain distance threshold and if the passing time has not yet elapsed, the commanded speed is limited to the ratio between remaining path and remaining time, thus slowing down the aircraft if the waypoint cannot yet be cleared. If the remaining distance falls below 10 m, the aircraft is stopped completely until the passing time elapses.

6.3.2 Calculation of position errors

The kinematic errors for the feedback controller are computed in this part of the controller. The longitudinal error e_{long} and course error e_ψ are immediately calculated through (6.1) and (6.13) respectively. For the lateral error, the target position in global coordinates needs to be determined first as follows:

$$X_{des} = \int_0^t \dot{s}_{des} \cos\psi_{des}\, dt = \int_0^t v_{x,des} \cos\psi_{des}\, dt \tag{6.26}$$

$$Y_{des} = \int_0^t \dot{s}_{des} \sin\psi_{des}\, dt = \int_0^t v_{x,des} \sin\psi_{des}\, dt \tag{6.27}$$

where the equality $\dot{s}_{des} = v_{x,des}$ introduced in Section 6.1.1 was used. With reference to Figure 6.9, the lateral error e_{lat} given the actual aircraft position in global coordinates $[X, Y]$ and course ψ is finally determined by:

$$e_{lat} = -(X_{des} - X)\cos\psi + (Y_{des} - Y)\sin\psi \tag{6.28}$$

The diagram of the error calculation block is illustrated in Figure 6.10.

6.3.3 Feedback controller

This part implements the longitudinal and the lateral control laws formulated in sections 6.1 and 6.2.

The lateral controller (Figure 6.11) is a direct implementation of the gain-scheduled state feedback controlled discussed in Section 6.2. Wind-up of the lateral error integrator must be prevented when the aircraft is stopped, i.e. $v_x = 0$, which makes the system (6.22) uncontrollable. This is done by freezing the integration in the vicinity of $v_x = 0$.

The longitudinal controller was instead enhanced with additional features. The diagram of the complete longitudinal controller is shown in figure 6.12. Firstly, an anti-windup scheme based on back-calculation [60] was implemented. Whenever

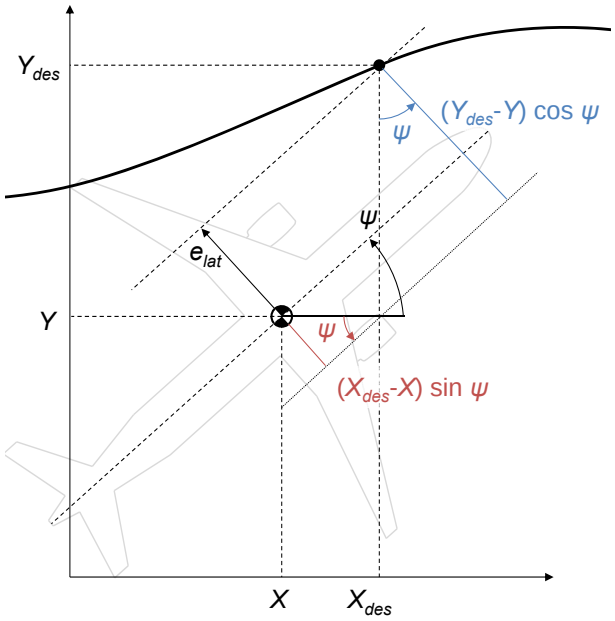

Figure 6.9: **Calculation of the lateral error e_{lat} from desired and actual aircraft position in global coordinates**

the motor torque commanded by the controller exceeds the rated motor torque in absolute value, the difference is weighted by an appropriate gain k_w and fed back to the longitudinal error integrator.

Moreover, the controller is also able to perform conventional taxi with the main engines. To this end, the torque signal is also used as throttle command to the main engines when they are activated, by scaling it by a heuristically determined signal gain k_{eng}.

Finally, the longitudinal controller also commands the landing gear brakes with three different strategies:

- when the electric taxi system is used, the commanded braking torque is the part of the commanded braking moment (i.e. controller signal with opposite sign to the speed) exceeding the rated motor torque, and zero otherwise;
- when the main engines are active and used during taxi, the commanded braking torque is the whole braking moment (i.e. controller signal with opposite sign to the speed), and zero otherwise;
- regardless of the propulsion device used, the brakes are activated with a preset value if the target speed is zero and the actual speed is in the vicinity of zero in

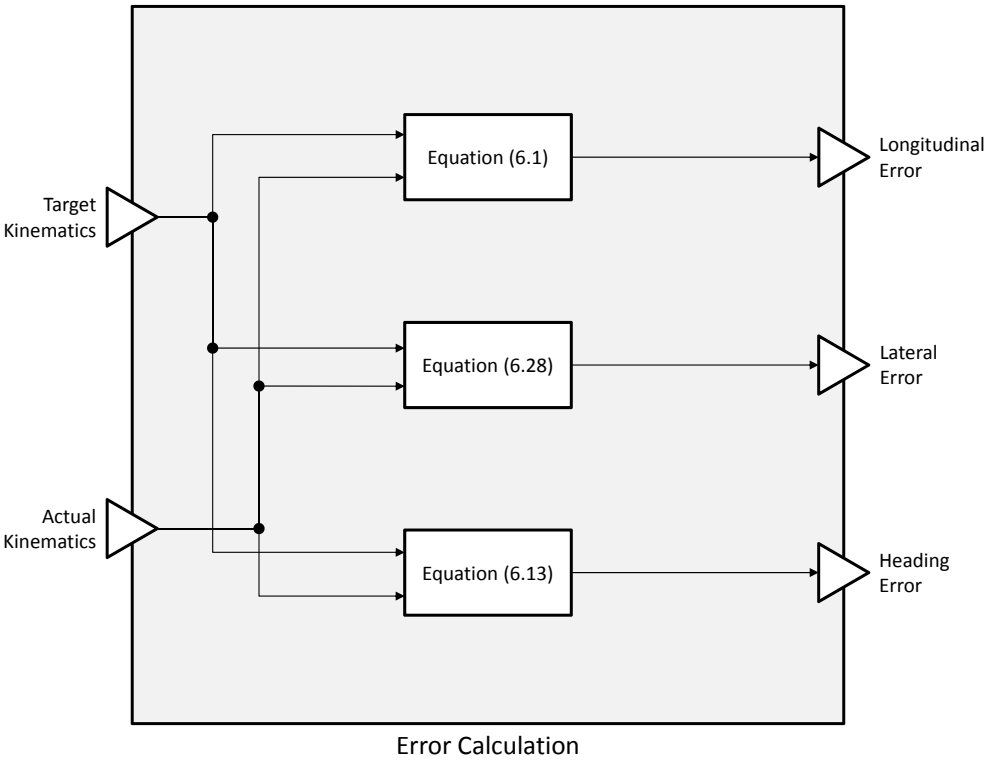

Figure 6.10: **Diagram of the error calculation block**

order to keep the aircraft stopped.

6.3.4 Overall controller

The complete diagram of the controlled plant is shown in figure 6.13. The aircraft model with Electric Taxi System model presented in Chapter 3 is connected to the feed-forward controller and the feed-back error rejection controller. When simulating ground operations, the aerodynamic surfaces of the aircraft model are kept in the neutral position with a zero input vector.

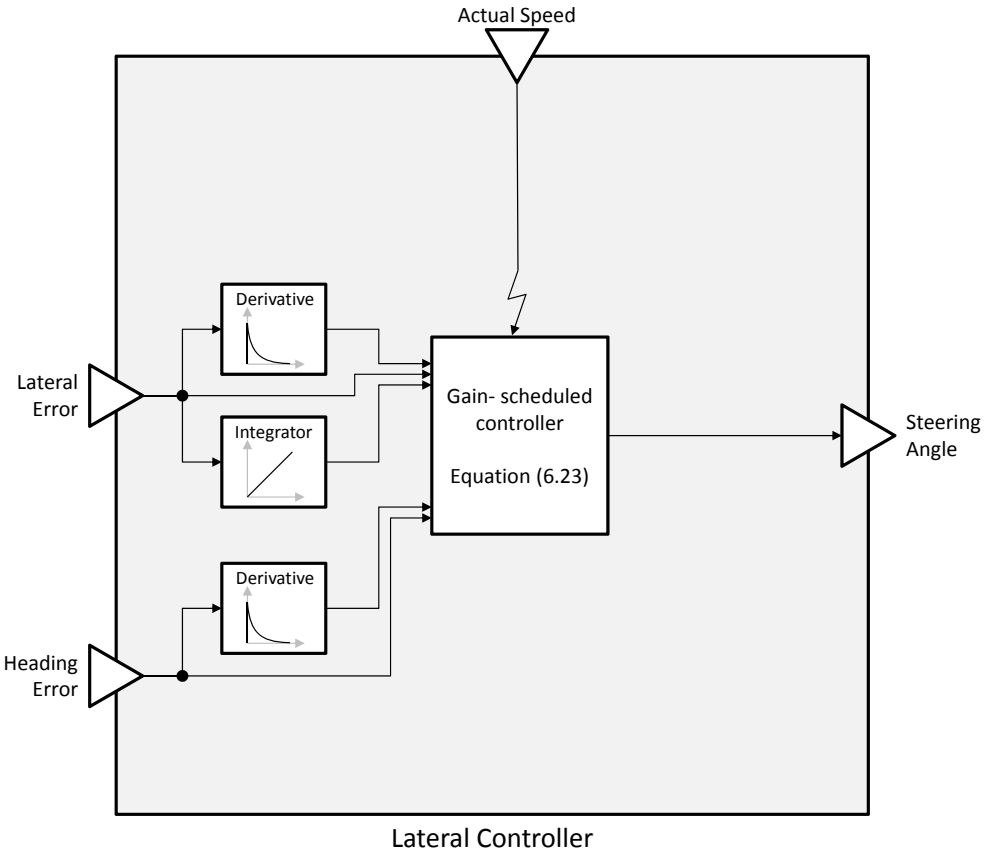

Figure 6.11: **Diagram of the lateral controller block**

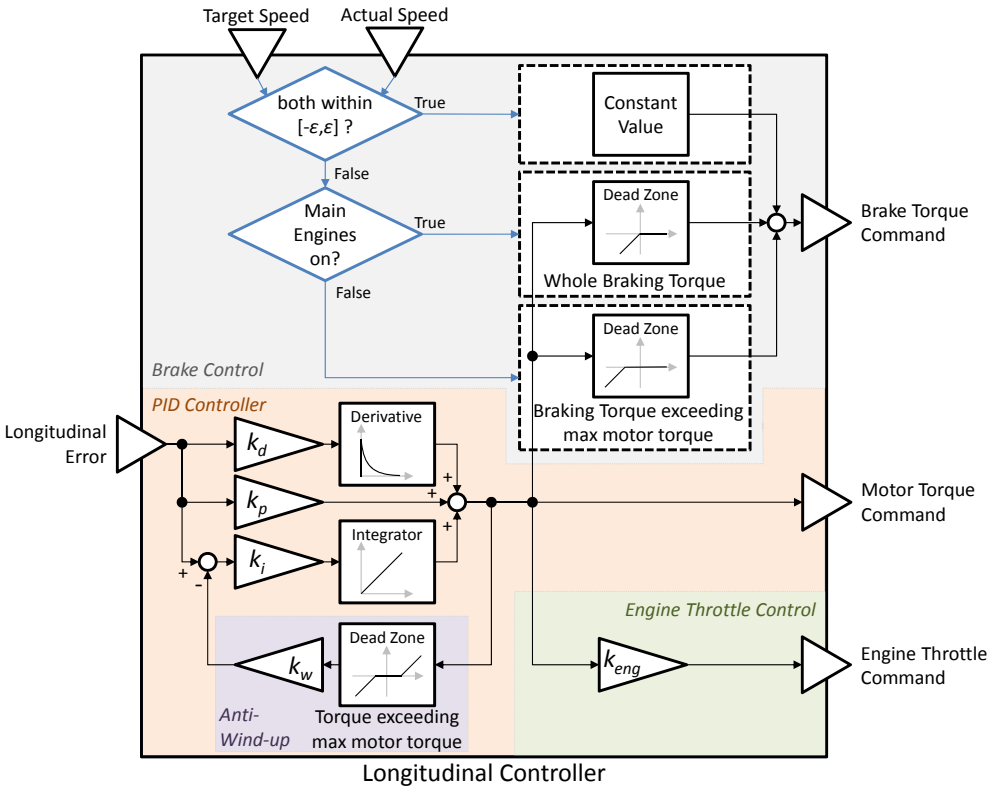

Figure 6.12: **Diagram of the longitudinal controller block**

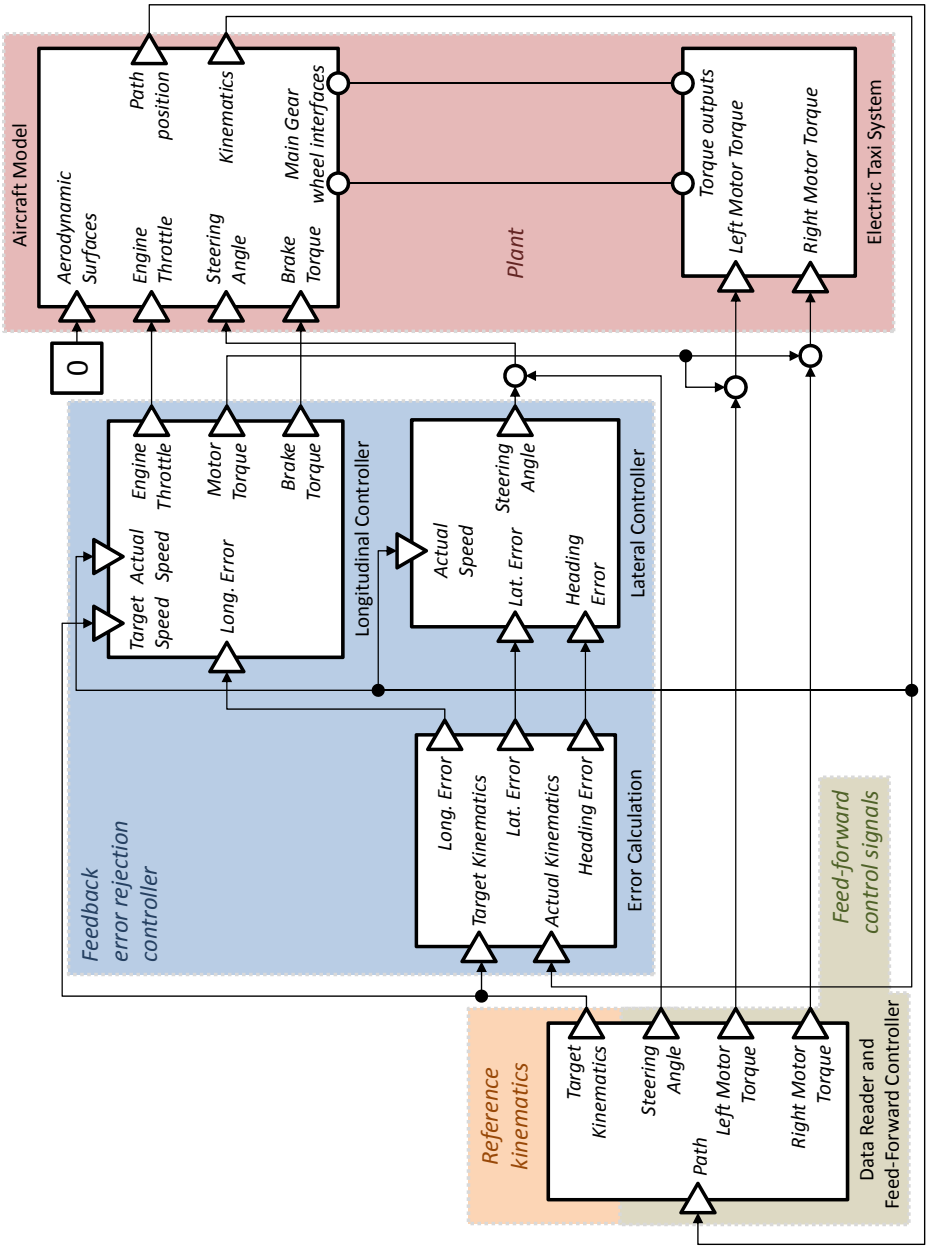

Figure 6.13: **Complete diagram of the controlled plant for simulation of ground operations**

7 Model-Based Performance Assessment of Electric Taxi Systems

This chapter illustrates how the complete methodology developed throughout this work can be used to assess on-board electric taxi systems and what potential it offers. To this end, different demonstrations are carried out. In the first one, generic taxi trajectories are combined with flight profiles of variable length to simulate sets of similar flight missions with different ranges. These simulations are performed for both conventional aircraft and aircraft equipped with ETS with various sizes. The purpose is to identify the sensitivities of performance criteria such as fuel consumption and operating costs in dependence of the flight mission and ETS characteristics.

In the second demonstration, thermal aspects are taken into account. The thermal behavior of the ETS is shown to be critical for practical operations, hence it needs to be considered carefully in the technology selection and early design phase.

In the third demonstration, economic benefits — i.e., operating costs — are considered as opposed to energetic benefits — i.e., fuel saving. A number of items that contribute to the operating costs beyond the fuel costs are affected by the adoption of ETS. Looking at the economic perspective may lead to different outcomes regarding the assessment.

Lastly, two real flight missions are simulated for both conventional and ETS-equipped aircraft and their results compared. The goal is to illustrate concrete advantages of the ETS technology in real-world cases.

7.1 Considered Aircraft

The aircraft model used in this chapter is representative of a narrow-body commercial aircraft such as an Airbus A320 or a Boeing 737. The model is based on the Modelica model described in Chapter 3 and features appropriate data sets for geometries, weights, aerodynamics as well as main engine thrust and emissions. Some key weights of the considered aircraft — mostly derived from the Airbus A320 data — are reported in Table 7.1. Also, ETS systems have been considered with the architecture described in Chapter 4. In particular, ETS with a sizing parameter λ_A in the range [0.85, 1.5]

Table 7.1: **Weights of narrow-body aircraft considered in the model-based ETS performance assessment**

Parameter	Value
Empty Operating Weight (EOW)	41,100 kg
Maximum Take-Off Weight (MTOW)	73,500 kg
Maximum payload	16,500 kg
Maximum fuel capacity	24,000 kg

have been adopted; their weight was determined as discussed in Section 4.8.

7.2 Sensitivity Study of Electric Taxi System Performance

In this first demonstration, the integrated model-based methodology is used to evaluate the benefit of adopting an electric taxi system depending on the mission length. Because the system improves taxi efficiency, but the additional system weight worsens flight efficiency, a relationship between the flight length (especially the ratio between taxi time and flight time) and the fuel saving is expected. For each particular flight mission, there is a *break-even flight length* at which a conventional aircraft will have the same gate-to-gate fuel consumption as an ETS-equipped aircraft. A conventional aircraft will be more efficient above the break-even flight length, while the ETS-equipped aircraft will perform better below it.

Determining the fuel saving involves comparing the simulations of the conventional and the ETS-equipped aircraft for each considered gate-to-gate mission and system. To reduce the computational workload, the following approach was adopted for this demonstration. Firstly, taxi trajectories are defined (Section 7.2.1) as well as a flight trajectory with variable flight length (Section 7.2.2). Afterwards, several flight missions (from start to landing) with different additional weights and flight lengths are simulated and their fuel consumption determined. By interpolating these data, a continuous function of the fuel consumption depending on added weight and flight length is defined (Section 7.2.3). The fuel consumptions for specific missions and aircraft configurations are then obtained quickly through the interpolated function. The taxi phases are simulated separately and their fuel consumption determined; at the same time, flight lengths corresponding to defined fuel consumption increases are found by applying the mission block fuel interpolation function (Section 7.2.4). Finally, the results are presented and discussed (Section 7.2.5).

7.2.1 Taxi-out and taxi-in trajectories

Two pairs of taxi trajectories (taxi-out and taxi-in) have been designed: a standard and a short one. All trajectories are based on real operations at the Frankfurt airport (IATA code: FRA - ICAO code: EDDF) and are shown in figures 7.1 and 7.2. They will also be described verbally below by using the official taxiway and parking position codes.

In the standard taxi-out trajectory, the aircraft starts from position A16, reverses into taxiway N7, then proceeds along N7 and the taxiway N until the holding point at the beginning of runway 18. When stops during taxi are considered in the simulation, one stop and hold is foreseen before the intersection with taxiway P, and two stop-and-go cycles are performed before the end of the taxi trajectory in front of runway 18. The length of the taxi-out trajectory is approximately 3,470 m.

The standard taxi-in trajectory begins on the high-speed turnout M23 after landing on runway 25L. The trajectory continues on taxiways M30, L17 and L, then on taxiway N8 until reaching the position A16 where the trajectory ends. Holding points are defined on M30 before crossing runway 07C/25C and on N8 before entering the apron. The length of the taxi-in trajectory is approximately 3,345 m.

The short taxi trajectories are similar to the standard ones, except for the aircraft parking position V166. In taxi-out, the aircraft reaches the taxiway N via N11 and travels to runway 18 as in the standard trajectory. In taxi-in, after rolling on taxiway L as in the standard case, the aircraft reaches its position via N11. The lengths of the short taxi-out and taxi-in trajectories are approximately 2,095 m and 1,780 m respectively.

7.2.2 Flight trajectory definition and simulation

The generic flight profile used for this demonstration is plotted in Figure 7.3. The flight includes start, climb, cruise, descent and landing. The heading is kept constant throughout the whole flight. A variable flight time and length is obtained by changing the duration of the cruising phase and keeping all other phases equal, as shown in Figure 7.3 for two cases. The flight trajectory is tracked through a generic cascaded PID controller commanding the aerodynamic control surfaces and the engines.

A number of simulations were performed within a matrix of flight lengths (between 528 and 1,133 NM) and additional weights (between 0 and 3,000 kg). The baseline payload was set at 15,000 kg; in connection with the additional weight range mentioned, this results in simulation of a range of payloads between 15,000 and 18,000 kg. The total fuel quantity at start comprises mission block fuel (for the proper flight mission), reserve fuel (for contingencies) and alternate fuel (needed to reach an alternate destination). The mission block fuel quantity was determined iteratively for each mission simulation to match the amount needed for the flight with an error in the range [+1 kg, 0 kg]. Additionally, a reserve fuel of 5% of the mission block fuel and an alternate fuel quantity of 2,300 kg were taken. These values are consistent with the specifications of

(a) **Standard Taxi Out (map data © OpenStreetMap contributors)**

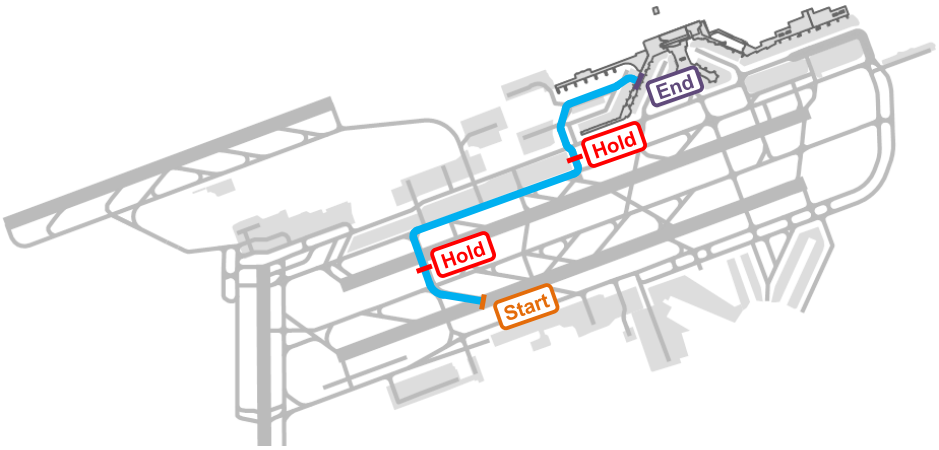

(b) **Standard Taxi In (map data © OpenStreetMap contributors)**

Figure 7.1: **Standard taxi trajectories defined at Frankfurt airport**

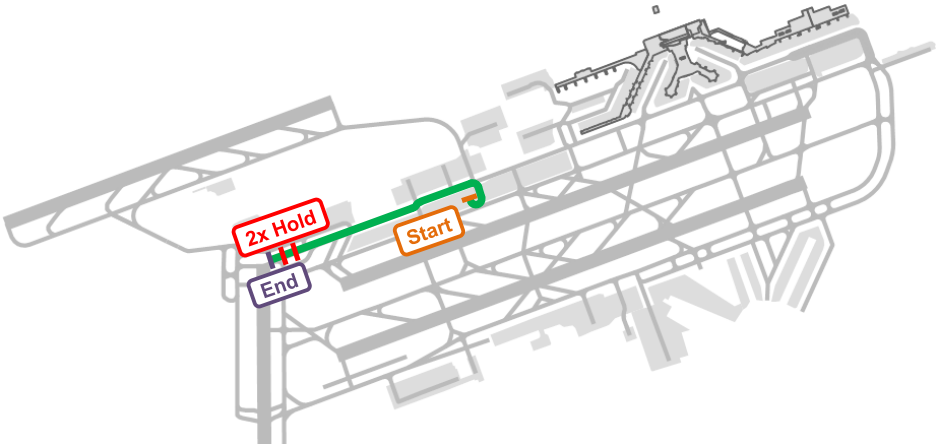

(a) **Short Taxi Out (map data © OpenStreetMap contributors)**

(b) **Short Taxi In (map data © OpenStreetMap contributors)**

Figure 7.2: **Short taxi trajectories defined at Frankfurt airport**

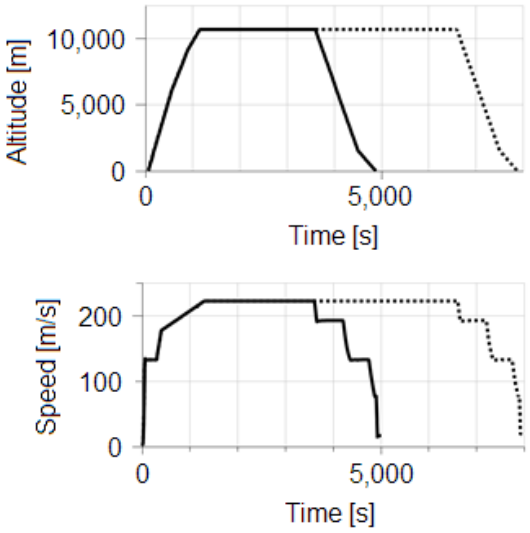

Figure 7.3: **Generic flight profile chosen for consumption sensitivity study. The flight time and length is varied by changing the duration of the cruising phase, as shown for two different missions (solid and dotted line). The heading is kept constant in the entire flight.**

the Association of European Airlines (AEA) prescribing 5% of the mission block fuel as reserve fuel, as well as alternate fuel sufficient for a 200 NM diversion followed by a 30-minute flight in holding configuration at an altitude of 1,500 feet [79, p. 387].

7.2.3 Function fitting for mission block fuel

After the simulation campaign, a function of the following form was fitted to the fuel consumption data in order to obtain approximate block fuel quantities for flights of arbitrary length:

$$\Delta SMF = \sum_{i=1,j=0}^{2} p_{1+3(i-1)+j} AW^i \cdot FL^j \tag{7.1}$$

where ΔSMF is the increase in specific fuel consumption per flight length unit, FL is the flight length, AW is the additional weight, and $p_k,\ k \in [1,6]$ are fitting parameters. For a given flight length FL, it is thus possible to calculate the fuel consumption increase per nautical mile flown due to the added weight AW with reference to the fuel consumption $MF_0(FL)$ of the baseline mission with 15,000 kg payload and no additional weight over the same flight length. $MF_0(FL)$ is determined by interpolation between all simulated flights without additional weight. Figure 7.4 shows the behavior of ΔSMF in dependence of AW and FL. The overall mission

block fuel MF is then given by:

$$MF = MF_0(FL) + FL \cdot \Delta SMF \tag{7.2}$$

7.2.4 Energetic balance for different missions and system size

This task is aimed at finding what benefit is reached in terms of fuel savings as the flight length and the ETS size vary. As mentioned in Section 7.2, the ground and flight phase were treated separately in this demonstration. The four mission scenarios listed in Table 7.2 were simulated for this demonstration. Also, ETS with the following sizing parameters λ_A were considered:

$$\lambda_A \in [0.8, 0.85, 0.9, 1, 1.1, 1.2, 1.3, 1.4, 1.5]$$

For the ground phase, taxi-out and taxi-in simulations were carried out for all the system sizes included in the above set, as well as for an aircraft without ETS taxiing conventionally. Following the approach illustrated in Figure 1.2, a ground phase simulation involves calculating the optimal taxi path following profile for each system and mission with the methodology discussed in Chapter 5, then simulating the taxi phase with the integrated aircraft model governed by the ground controller presented in Chapter 6. The taxi profile optimization used the fuel minimizing cost function without any thermal or time constraints. The integrated mission simulations were subject to the following assumptions.

1. A full payload of 16,500 kg is loaded.
2. To avoid multiple simulation iterations searching for the fuel quantity exactly needed, the fuel quantity for all taxi-out simulations was taken as the mission block fuel calculated with (7.2) considering a 1,133 NM flight length, a full payload of 16,500 kg and the additional weight of the largest ETS with $\lambda_a = 1.5$, plus the prescribed alternate and reserve fuel as well as additional 100 kg for taxi-out consumption. These high fuel quantities add to the conservativeness of the taxi-out simulation results.
3. Likewise, the fuel quantity for all taxi-in simulations was conservatively taken as no mission block fuel, plus the reserve fuel corresponding to the above flight with the largest ETS, alternate fuel as prescribed, and additional 100 kg for taxi-in consumption.
4. An engine warm-up and cool-down time of 3 minutes must be observed on ETS-equipped aircraft. When simulating ETS taxi, the first 3 minutes of taxi-in respectively the last 3 minutes of taxi-out will therefore be performed conventionally with the main engines, and the ETS will be switched off. An assumption is made that the engines may be started up and cut off at any time during

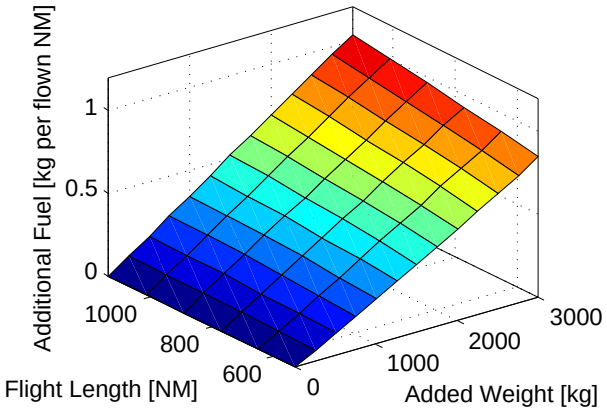

Figure 7.4: **Fuel consumption increase per nautical mile flown as a function of additional weight and flight length with reference to the fuel consumption of the baseline mission without additional weight over the same flight length**

Table 7.2: **Four mission scenarios considered in the first demonstration (sensitivity study of ETS performance)**

	No stopping required at the holding points	Stopping and holding required at the holding points until defined minimum passing times are elapsed
Standard taxi-in and taxi-out profile	*Standard taxi, no stops*	*Standard taxi with stops*
Short taxi-in and taxi-out profile	*Short taxi, no stops*	*Short taxi with stops*

taxi, even in motion. The APU is off whenever the main engines are on, and vice-versa.

5. In the conventional simulation, the main engines are started up during taxi-out as soon as pushback is finished and run until the end of taxi-out, while the APU is running from simulation start until the end of pushback. During the whole taxi-in, the main engines are constantly running while the APU is off.
6. When simulating conventional aircraft, the taxi profile calculated for the aircraft with ETS with λ_A= 1.5 is used as simulation input.
7. For this part of the demonstration, the thermal behavior of the ETS is neglected.

Calculating the fuel consumption difference for both taxi phases between the conventional aircraft and a given ETS-equipped aircraft gives the fuel saving on the ground.

For the flight phase, (7.2) is used simultaneously for both the conventional aircraft and an aircraft equipped with a certain ETS, considering the ETS weight as well as 16,500 kg payload (resulting in an added weight AW of 1,500 kg in (7.2) in addition to the baseline payload of 15,000 kg). Because no geometry data were available, it was assumed that the additional weight does not displace the aircraft center of gravity. Iterations allow to find the flight length corresponding to a defined fuel consumption increase between the two cases. The difference between this increase and the fuel saving on the ground gives the fuel balance over the entire mission.

7.2.5 Discussion of results

By applying the methodology presented above for different ETS sizes and flight lengths and interpolating the results, *fuel balance maps* are plotted in figures 7.5 and 7.6. They express what energetic benefit is achieved for each ETS size and for each given mission length; also, the break-even flight length can be read out for each ETS size. This kind of diagrams can be useful for airlines considering the adoption of the ETS technology: the overall expected benefit for various ETS systems can be determined through the sum of the fuel savings in the different legs of the schedule of a certain aircraft. This data will have a key role among other criteria in the decision process of the technology adoption.

To discuss the results, it is useful to consider the overall taxi times (taxi-out plus taxi-in) elapsed in the simulations. These times depend on the ETS size since the optimal taxi profile is different in general for each ETS system. Table 7.3 shows the minimum and maximum taxi times for the four mission scenarios, corresponding to the smallest and largest ETS considered. Comparing the taxi times with the fuel balance maps, it is easy to notice that the break-even flight lengths are correlated with the taxi times. Also, larger and heavier ETS sizes generally worsen the overall energetic efficiency for each given mission length, which in turn results in shorter

(a) **No stops along the taxi trajectories**

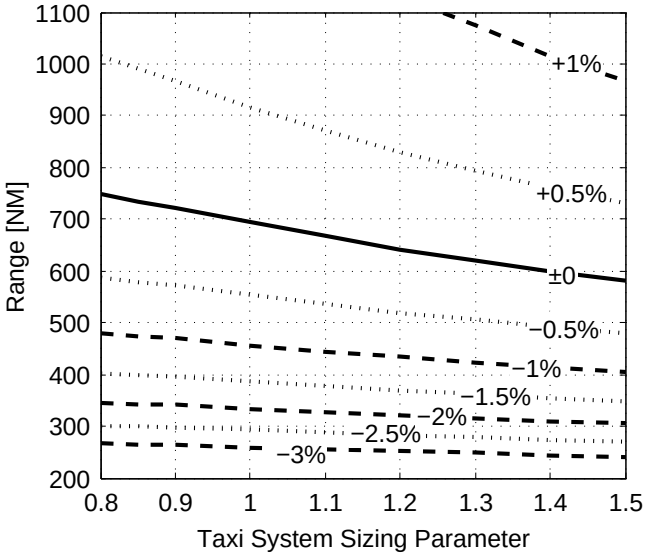

(b) **Stops and holding times along the taxi trajectories**

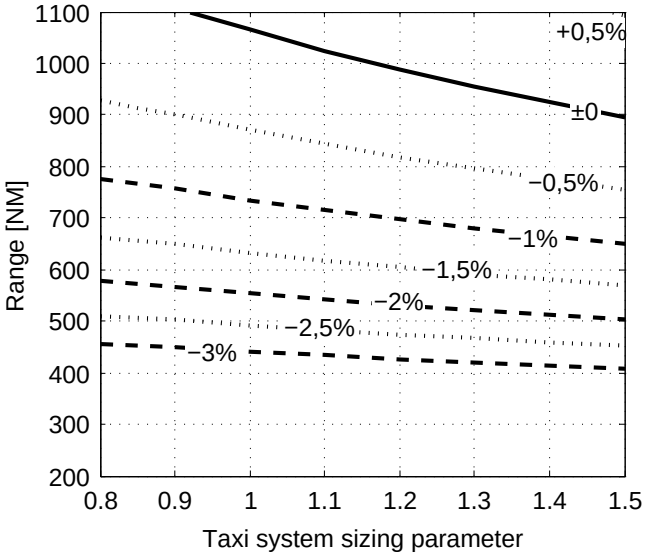

Figure 7.5: **Fuel balance maps for generic flight missions with standard taxi-in and taxi-out profiles. The level curves show the mission block fuel difference compared to the same flight with conventional aircraft taxiing with main engines.**

(a) **No stops along the taxi trajectories**

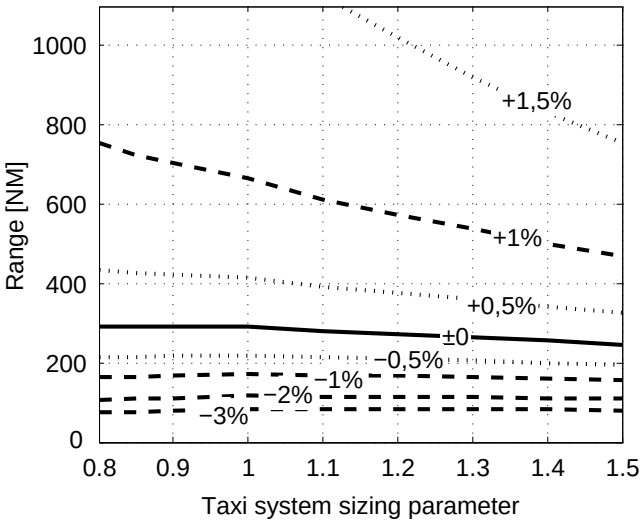

(b) **Stops and holding times along the taxi trajectories**

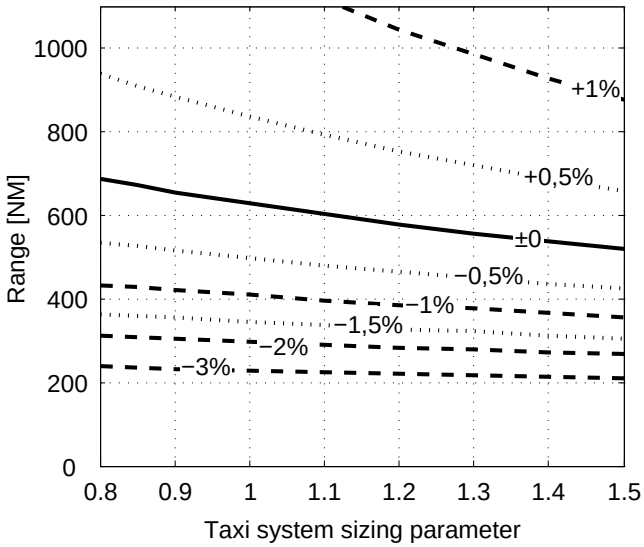

Figure 7.6: **Fuel balance maps for generic flight missions with short taxi-in and taxi-out profiles. The level curves show the mission block fuel difference compared to the same flight with conventional aircraft taxiing with main engines.**

Table 7.3: **Overall taxi times (taxi-out plus taxi-in) for the four different mission scenarios**

Mission scenario	Taxi time	
	λ_A=0.8	λ_A=1.5
Standard taxi, no stops (Fig. 7.5a)	1,246 s	1,220 s
Standard taxi with stops (Fig. 7.5b)	1,733 s	1,727 s
Short taxi, no stops (Fig. 7.6a)	754 s	736 s
Short taxi with stops (Fig. 7.6b)	1,036 s	1,030 s

break-even distances for large ETS. These results hold qualitatively in general and are in line with the expectations.

However, two aspects will be discussed that justify the use of the model-based methodology for ETS assessment. Firstly, in the fuel balance maps for the short taxi scenario without stops (Figure 7.6a) the break-even flight length curve and all curves below (representing shorter flight lengths with a fuel saving benefit) are not monotonically decreasing for larger ETS, but they show a plateau or even a small increase from the smallest ETS up to λ_A= 1 approximately. This counter-intuitive result derives from the fact that using the smallest ETS with worse performance will increase the taxi times. Because the fuel consumption is strongly correlated with the taxi times due to the APU idle fuel consumption (see Section 5.4.3), the ground efficiency shrinks with the smallest ETS such that the smaller weight no longer compensates it during the relatively short flight mission. For such a mission, not only would a larger ETS allow superior ground performances, but it would do so without losing overall efficiency. This kind of effects would not be predictable with common-sense observations or calculations based on average parameters. This makes the case for the thorough model-based assessment methodology presented in this thesis.

The second point pertains to the dependence of the results on the taxi time. The aim was to verify whether the added complexity of the model-based approach is really necessary for a precise benefit assessment. To this regard, a mission scenario was defined with the same flight profile discussed in Section 7.2.2 and perfectly straight taxi-out and taxi-in trajectories, featuring one acceleration to cruising speed, one constant speed phase, and one final deceleration to a stop. The length of the constant speed phase was adjusted so that the total taxi time of these new scenarios would approximately match the taxi times of the four realistic missions for the largest ETS with λ_A= 1.5. Four new missions were therefore generated. Then, the break-even flight lengths were calculated for the new scenarios by comparing the performances of the conventional aircraft and the ETS-equipped aircraft with λ_A= 1.5. The results are plotted in Figure 7.7 along with the the break-even flight lengths of the four missions with realistic taxi trajectories. This diagram shows the behavior of the break-even flight length for increasing taxi times. On the one hand, it is apparent that there is a strong relationship between the taxi time and the break-even flight length, thus suggesting that looking at the taxi time to flight length ratio for a given mission

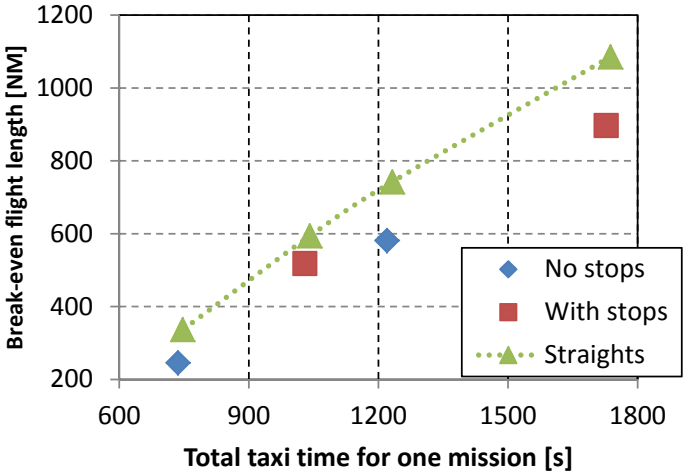

Figure 7.7: **Comparison of break-even flight lengths between the four mission scenarios with realistic taxi profiles and scenarios with straight taxi profiles and similar taxi times**

may be a reasonable quick criterion for a first assessment of energetic benefit for that mission. On the other hand however, there are strong differences in the break-even flight lengths between two missions with similar taxi times, ranging from 15 to 37%. This difference is generally due to the fact that the realistic taxi profiles require more fuel to be burned because of the more frequent accelerations and decelerations; the efficiency of taxiing with ETS is therefore diminished, which shrinks the benefit of ETS over the whole mission with respect to the less dynamic straight profiles. This proves that an assessment based solely on taxi times and average consumption may be misleading; in fact, the ground dynamics have a clear influence on the overall balance and therefore need to be considered carefully for each mission relevant to the case study, as the proposed model-based methodology does.

7.3 Considering Thermal Aspects

In this task, the thermal model of the ETS described in Section 4.5 is considered during the simulation of the ground phases. The standard taxi-out profile was selected for simulation with an ETS with $\lambda_A = 1$. The starting temperature of the ETS was 50 °C. Firstly, the optimal path following profile was determined for taxi-out without stops. In the subsequent simulation though, stops and holding times were imposed. In the vicinity of each holding point, the feed-forward controller will suspend the path following if necessary and will stop the aircraft until the relative passing time has elapsed (see Section 6.3.1). This is intended to represent an aggressive driving style

not anticipating the required stops. This puts a stress on the ETS because brakings and accelerations are relatively harsh. The speed profile along the taxi-out trajectory is shown in Figure 7.8. This taxi profile will be referred to as *standard taxi-out profile with thermal issues* in this section.

A limit of 150 °C on the ETS motor coil temperature is assumed. Figure 7.9 displays the coil temperature over the travel time along the trajectory. Overheating occurs at about half of the trajectory. As a consequence, the ETS architecture and size chosen would not be suitable for this taxi profile.

The overheating problem may be overcome in a number of ways. Three methods have been chosen here for discussion. The first method is to start up the main engines and continue taxi conventionally as soon as the temperature limit is reached. This involves the assumption that the engines may be started at any time and in any state (e.g. aircraft in motion). Note that this assumption was already made regarding the engine warm-up phase towards the end of taxi-out. Figure 7.10 displays the behavior of the motor coil temperatures as well as the motor peak phase currents in order to show that when the temperature limit is reached, the ETS is deactivated and can cool off for the rest of taxi-out. Clearly, partially conventional taxi will result in an efficiency loss compared to full electrical taxi-out, hence the usefulness of ETS is somewhat diminished.

Method 2 consists in using a larger ETS. Having a greater mass, a larger system has a superior thermal capacity. In connection with the fact that the system power is identical for the whole ETS family considered, the limit temperature will then be reached in a longer time. In Figure 7.11, taxi-out was performed with an ETS with $\lambda_A = 1.3$ instead of 1. The motor coil temperatures can be seen to remain in the allowed range as the ETS operates throughout the whole taxi trajectory until engine warm-up begins 180 s before the end of the trajectory. While it is possible to complete the taxi-out profile with the larger ETS, the heavier system will worsen the efficiency in flight.

Method 3 involves more anticipation: a more defensive driving style can help save energy and reduce heat production. This translates into setting appropriate constraints in the optimal path-following profile generation. Two ways can be followed:

a. set *thermal constraints* (see (5.32)), i.e. limit torques so that waste heat is reduced;

b. set *minimum passing times* (see Section 5.5), i.e. limit speeds so that no stops and accelerations are needed at the holding points.

Both methods result in generally lower speeds, as displayed in Figure 7.12. While the temperature limit is respected in both cases, method 3b is more effective in that the temperatures are further lowered to approximately 120 °C.

To compare the four methods, a mission is taken consisting in the taxi-out performed with each respective method for coping with the thermal problem, the generic flight mission described in Section 7.2.2, and the standard taxi-in trajectory with stops performed normally (stops considered in path-following optimization, no thermal

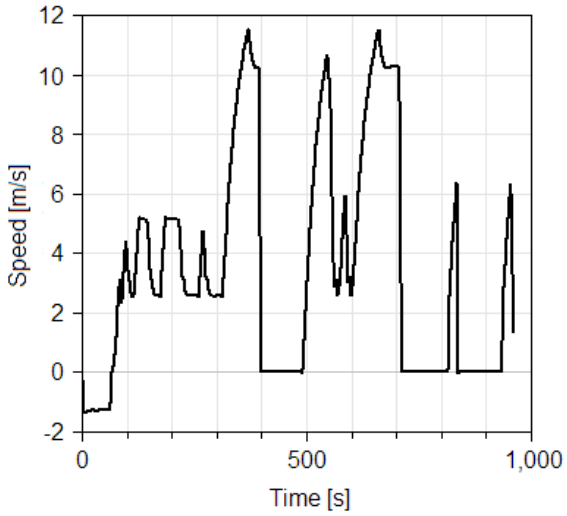

Figure 7.8: **Speed profile on taxi-out trajectory with unexpected stops for thermal behavior study**

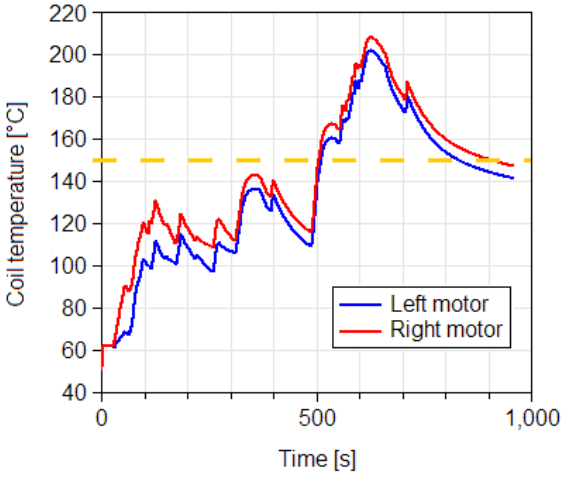

Figure 7.9: **Coil temperatures of the two ETS motors on taxi-out trajectory with unexpected stops for thermal behavior study. The dashed line marks the temperature limit of 150 °C.**

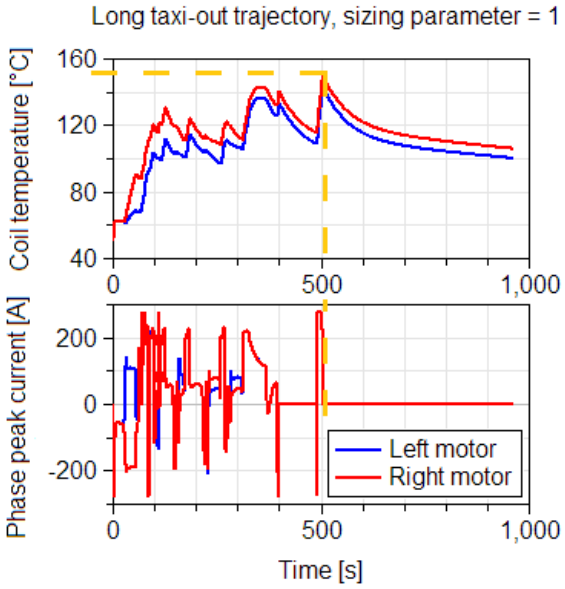

Figure 7.10: **Motor coil temperatures and motor peak phase currents on taxi-out trajectory with adoption of method 1 (continue taxi conventionally) in case of overheating. The dashed line marks the temperature limit of 150 °C.**

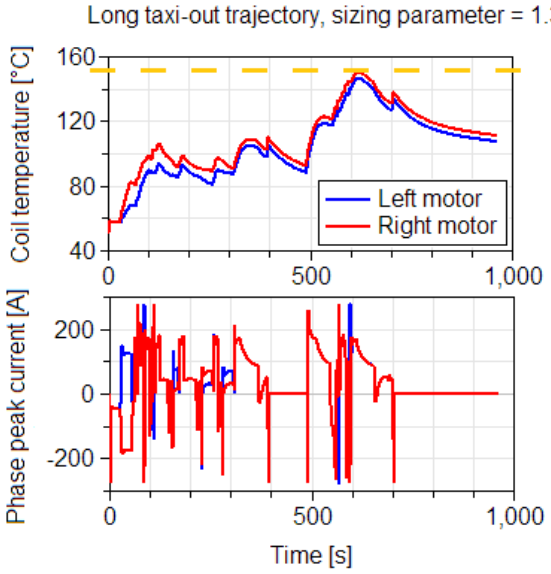

Figure 7.11: **Motor coil temperatures and motor peak phase currents on taxi-out trajectory with adoption of method 2 (use larger ETS). The dashed line marks the temperature limit of 150 °C.**

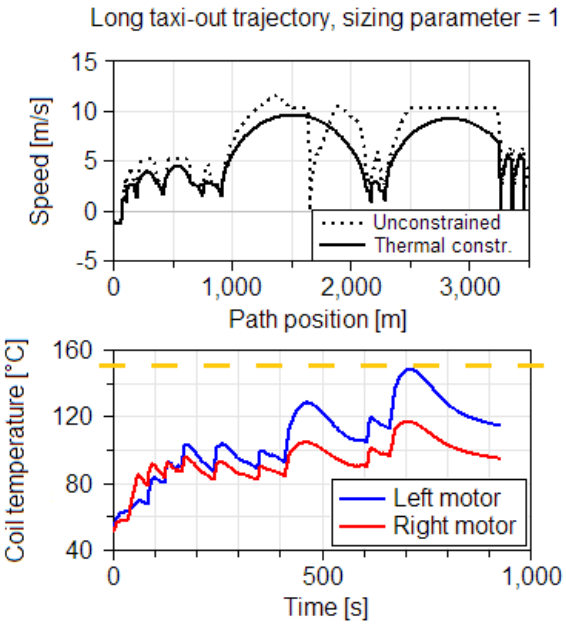

(a) **With thermal constraints**

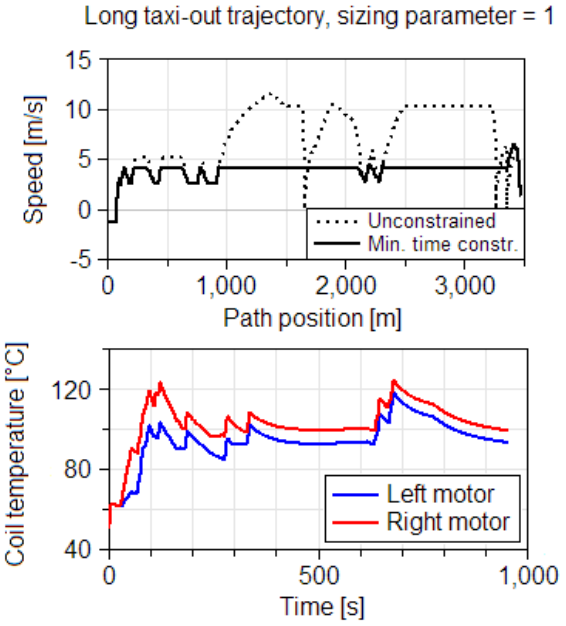

(b) **With minimum passing times**

Figure 7.12: **Aircraft taxi speed and motor coil temperatures on taxi-out trajectory with adoption of method 3 (less aggressive driving). The dashed line marks the temperature limit of 150 °C.**

Table 7.4: **Performance comparison for the four solutions to the thermal limitation in taxi-out**

Method	Fuel saved on ground [kg]	Break-even flight length [NM]
1. Partly conventional	161.4	848.1
2. Larger ETS	216.2	955.4
3a. Thermal constraints	221.8	1083.6
3b. Minimum-time constraints	233.0	1124.5

Table 7.5: **Comparison between method 1 and 2 for a single flight mission**

Method	Fuel difference with conventional [kg]		Balance [kg]
	On ground	In flight	
1. Partly conv.	-161.4	84.8	-76.7
2. Larger ETS	-216.2	97.6	-118.6

Table 7.6: **Comparison between method 1 and 2 for a given daily schedule**

Method	Fuel difference with conventional [kg]			Balance [kg]
	On ground		In all flights	
	Mission with thermal issues	Missions without thermal issues		
1. Partly conv.	-161.4	-502.4	423.8	-240.1
2. Larger ETS	-216.2	-504.7	488.2	-232.8

issues). The results are shown in Table 7.4. The first column gives the fuel saved on both taxi-out and taxi-in referred to conventional taxi, while the second column is the resulting break-even flight length for the considered mission type. Method 3b (setting minimum passing times) turns out to be the most efficient solution, since it features the most fuel saved and allows the longest flight length before the ground saving is evened out.

In real airports, it may be the case that taxiing with slower speeds is not possible or desirable, thus either method 1 or 2 are the only valid options among the considered ones for dealing with over-temperature problems. A 500 NM flight is now assumed with the discussed standard taxi-out profile with thermal issues, a generic flight profile (see section 7.2.2) and the standard taxi-in profile with stops (stops considered in path-following optimization, no thermal issues). If only this flight is considered, method 2 is the better solution over method 1 as it saves more fuel considering the ground benefit and the fuel penalty in flight (see Table 7.5).

However, this result may change if a different mission, or mission mix, is considered. For example, the following daily schedule is taken:

- one 500 NM flight mission with standard taxi-out with thermal issues, generic

flight profile, standard taxi-in with stops;

- afterwards, four 500 NM flight mission with standard taxi-out without stops, generic flight profile, standard taxi-in with stops. This taxi-out profile does not face thermal issues since the simulated motor coil temperatures reach 135 °C for the ETS with λ_A= 1 and 103 °C for the ETS with λ_A= 1.3.

The balance of this schedule is displayed in Table 7.6. In this particular case, method 1 has a better balance over the daily schedule. To put it differently, installing the smaller ETS and resorting to conventional taxi in the only mission of the daily schedule experiencing thermal problems results in superior overall efficiency than using a larger ETS in the daily mission schedule considered. By contrast, method 2 of using the larger ETS is preferable if the schedule only contains the mission with the thermally problematic taxi-out.

From these results, the conclusion can be drawn that thermal aspects should be taken into account in the early design phase and architecture selection of electric taxi systems, as thermal limitations have a strong influence on the system efficiency and functionality. While operational methods can be adopted to limit the thermal stress on the system, the choice of the most efficient ETS strictly depends on the specific aircraft and mission plan. The dynamic simulation and assessment methodology presented in this thesis constitutes a powerful means for dealing with thermal aspects effectively focusing on a given particular case.

7.4 Using Operating Costs as Assessment Criterion

This section deals with the impact of electric taxi systems on the operating costs sustained by the airlines. In the following non-exclusive lists, some operational aspects are mentioned that may be subject to changes as a consequence of the adoption of ETS and can in turn affect the operating costs.

The following aspects have a positive impact:

- The overall fuel balance as discussed in the previous sections is an obvious cost driver. Fuel savings will result in fuel cost reduction.
- A tow tractor is no longer needed for pushback since the on-board ETS is capable of backwards motion. This saves the costs of tow tractor rent from the airport operators.
- Because the torque of the ETS can be controlled easily to follow speed targets and possibly to perform regenerative braking, the use of carbon brakes can be reduced. This is valid in terms of both the number of applications during a taxi cycle — e.g. brake pulses are no longer needed to control the taxi speed and contrast the engine idle thrust — and the braking force needed since one part of the kinetic energy is taken by regenerative braking. This will decrease brake

wear (see Section 2.1.2) and the associated costs.

- Some primary airports such as Frankfurt [34] charge airlines for noise and emissions in the airport area. These fees are calculated on standardized landing-takeoff cycles based on airline fleet databases. An ETS-equipped aircraft abates noise and emissions during ground operations due to its superior efficiency. This circumstance may be acknowledged in the calculation of the noise and emission charges, leading to their reduction.

The following aspects have a negative impact:

- The APU will run for longer time to supply the ETS and the aircraft subsystems, resulting in higher maintenance costs with respect to conventional aircraft.
- As an additional aircraft system, the ETS itself requires periodic maintenance, thus causing an increase in maintenance costs.
- Using an ETS may require the ground speed profiles to adapt to the system characteristics. Airport operators might set financial incentives and disincentives on circumstances impacting airport operations in an effort to increase the airport capacity. This might possibly translate into additional fees for ETS-equipped aircraft if they show lower performance compared to conventional taxi.
- Depending on the aircraft type and configuration, the added weight due to the ETS may possibly require a reduction of the allowed payload in order to comply with aircraft weight limits. In this case, the part of the payload that cannot be transported results in a loss of revenue that should be regarded as an opportunity cost.

The following aspect does not have an obvious outcome:

- The main engines are not running during most of the ground operations, which reduces running hours and, in turn, their maintenance cost. By contrast, the reduced warm-up time on taxi-out has a negative impact on engine wear. This aspect will be discussed in more depth in the next paragraph.

By the very nature of the air transport business, the impact of ETS on operating costs can be a more interesting assessment criterion for airlines. Due to the diverse repercussions of this technology on operating costs, the outcomes of an economic and an energetic assessment (i.e. mission fuel balance) may differ. In the following paragraphs, after giving a brief overview on the effect of electric ground operations on engine maintenance costs, simple economic assessments will be carried out exemplarily for some missions and their results compared with the energetic assessments of Section 7.2.

7.4.1 Impact of ETS and warm-up time on engine maintenance costs

An illustration of the basic concepts on engine wear and maintenance is needed to understand how the introduction of ETS can affect the engine maintenance costs and hence include the last aspect mentioned in the previous paragraph in the economic analysis.

Among the operating parameters of a jet engine, one of the primary ones is the Exhaust Gas Temperature (EGT) [11, 72] which is connected to the amount of fuel burned in the engine to produce thrust. During a flight mission, the *peak EGT* is normally reached during or soon after take-off, where the thrust demand is high. The EGT serves as both a control parameter and a health monitoring parameter. On the one hand, engine wear is proportional to EGT due to deterioration of the component surfaces; also, a temperature limit (*EGT redline*) exists to avoid immediate engine damage. EGT is therefore kept in a safe range by the engine power control. On the other hand, as wear progresses, the engine loses thermodynamic efficiency: less of the combustion energy can be transformed into thrust, which results in higher EGT. *EGT margin* is defined as the difference between the EGT redline and the peak EGT. New or refurbished engines have a relatively large EGT margin, which shrinks with increasing wear until zero is reached, triggering a maintenance event for the engine. The maintenance frequency depends on the operational severity. Notably, reducing the take-off thrust whenever possible — a procedure known as *take-off thrust derate* — results in lower EGT, hence lower wear (see Figure 7.13). Also, an aircraft performing shorter flight missions will experience more engine wear over time than one long-range aircraft due to the more frequent take-offs. Finally, environmental aspects play a role such as dusty, sandy or salty atmospheres which are erosive to the engine parts.

Simple engine maintenance cost calculation models [11, 72] account for all the mentioned effects by using a *severity factor* to adjust the base maintenance cost figure, expressed in currency per flight hour, for a given particular case. Severity factors are a function of the average flight time (given by the ratio between the total flight hours and the number of flight cycles) and other factors such as the environment and the thrust derate percentage.

In a conventional aircraft, the main engines are normally running during the whole taxi-out time, which allows the engines to warm up gradually before take-off. As this is no longer the case when using ETS, a warm-up time needs to be defined at which the engines must be started up and kept running at idle prior to take-off. For all practical purposes, this translates into performing taxi conventionally in the final part of taxi-out. A longer warm-up time therefore reduces the usefulness of the ETS, increases the idle fuel consumption as well as engine running hours — and in turn maintenance costs. By contrast, too short warm-up can generate higher wear during take-off.

In the following, a very rough estimate of the impact of warm-up time on engine

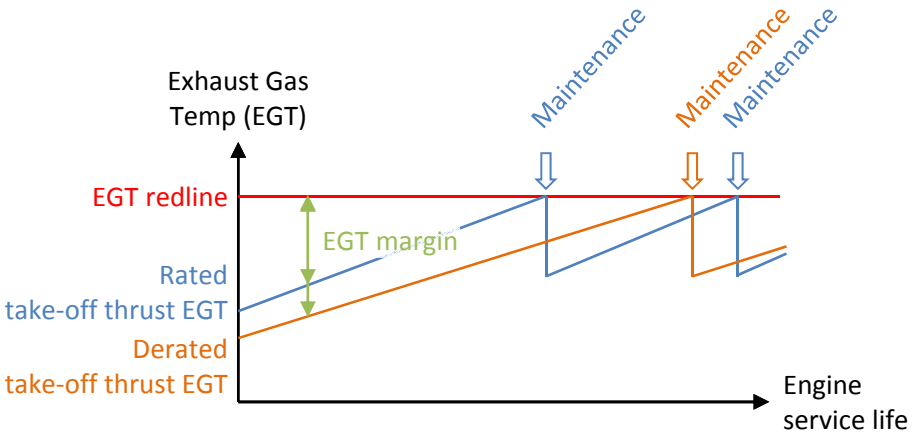

Figure 7.13: **Behavior of the peak EGT during the engine service life. When the EGT margin reaches zero, maintenance must be performed. Thrust derate reduces engine wear, thus widening the maintenance intervals.**

wear is given based on some literature data for illustration purposes. Figure 7.14 shows the takeoff EGT margin increase as a function of the idle time on taxi-out (warm-up time) for a CFM56 engine on a cold start, defined as a start after a shut-down longer than 6 hours. The reference EGT margin is taken at the minimum prescribed warm-up time of 2 minutes. The underlying data are taken from [22]. The data interpolation clearly shows a monotonic behavior, suggesting that a longer warm-up is always beneficial for EGT margin. At the same time according to Boeing [78], a 25% takeoff thrust derate for a Pratt & Whitney PW0456 engine on a Boeing B747-400 results in an EGT reduction of 56 °C, or approximately 7% with regard to the EGT at rated thrust (783 °C); this 7% EGT reduction in turn reduces the maintenance material costs (MMC) by 25%. MMC approximately amount to 65% of the total engine maintenance costs [11, p. 34]. An approximate estimation of the overall cost reduction can then be derived as:

$$\frac{\text{MMC reduction} \cdot \text{MMC quota over total maintenance cost}}{\text{EGT reduction}} = \frac{25\% \cdot 0.65}{56\ ^\circ\text{C}}$$

$$= 0.29\% \frac{\text{maintenance cost reduction}}{1\ ^\circ\text{C EGT reduction}} \tag{7.3}$$

thus expressing the cost reduction as a function of the EGT reduction. By combining this result with the data plotted in Figure 7.14, a function is obtained for the maintenance cost reduction over the warm-up time.

The discussed reduction is counteracted by the increase in engine running hours, which results in a rise in maintenance costs since they are based on engine usage time. Also, the increased idle fuel consumption needs to be taken into account. As an example, the CFM56-5B3, -5B4, and -5B6 engine types are considered. These engine

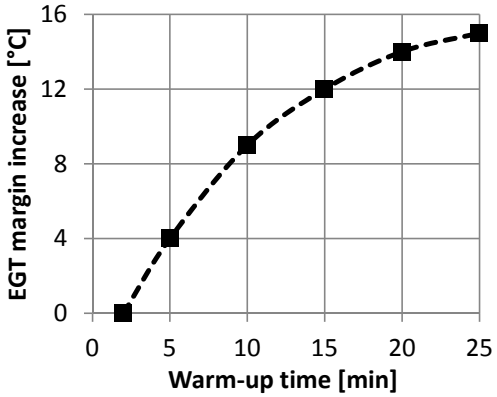

Figure 7.14: **Engine EGT margin increase over warm-up time on taxi-out for a CFM56 engine on a cold start, with respect to the minimum prescribed warm-up time of 2 minutes. The data are taken from [22].**

models are commonly found on the current production Airbus A320 family. The base maintenance cost rate for these engines ranges from 68 to 134 US$ per flight hour [10], while the idle fuel consumption varies between 0.097 and 0.115 kg/s [41]. For the present calculation, average values of 100 US$ as base maintenance cost rate and of 0.105 kg/s as idle fuel consumption were taken.

An illustrative cost comparison of warm-up times was carried out for three missions with different flight times. These have an impact on the adjusted engine maintenance costs through severity factors [11]. The warm-up time of 15 minutes was taken as reference for a conventional aircraft. The plot in Figure 7.15 displays the balance between the fuel cost reduction due to the shorter warm-up and the maintenance cost increase connected to the discussed EGT margin reduction due to shorter warm-up, calculated over the whole flight duration. A jet A fuel price of 2.20 US$ per gallon was considered, which is the average of the market price in the period from November 2013 to November 2015 as calculated from official U.S. Energy Information Administration data [83]. The plot shows that the cost balance was always negative, i.e. a reduced warm-up time always resulted in a cost reduction as the fuel saving outweighed the increased engine wear. This simple analysis suggests that on an ETS-equipped aircraft, the warm-up time on taxi-out should be kept as short as required for technical safety in order to maximize the overall benefit given by the ETS. Note that this balance does not yet include the running hours reduction, which would further decrease costs.

7.4.2 Assessment example with operating cost criterion

The operating cost balance is now calculated as an example for the “short taxi with stops” mission scenario (Table 7.2). Similarly to what has been done for the fuel

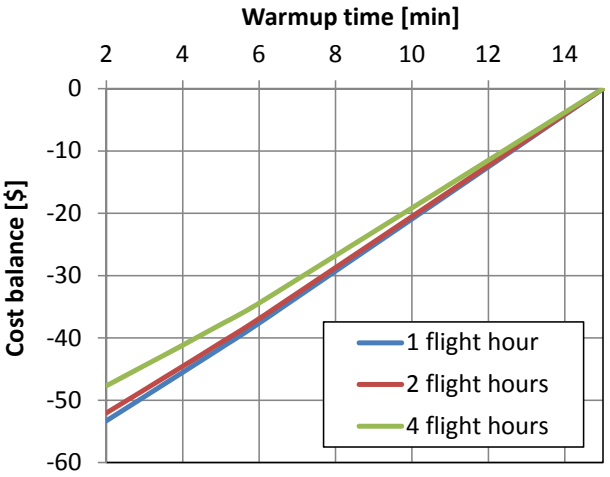

Figure 7.15: **Cost balance over warm-up time for three different flight missions. The warm-up time of 15 minutes was taken as reference for a conventional aircraft.**

consumption assessment, the operating cost balance was calculated in dependence of the ETS size for five missions of the mentioned scenario that only differ in their flight length. This balance compares the following cost items between conventional and ETS-equipped aircraft for each flight mission:

- fuel saved in ground operations;
- block fuel increase due to ETS weight;
- increase in engine maintenance costs due to shorter warm-up prior to start, and concurrent decrease in engine maintenance costs due to less running hours during taxi. Appropriate severity factors from [11] for the respective mission lengths with 10% derate are taken into account when determining the engine maintenance costs;
- increase in APU maintenance costs due to more running hours during taxi;
- tow tractor leasing costs;
- decrease in NO_x-related airport charge due to emission abatement with ETS operation. Only the simulated NO_x emissions, which are available as a simulation result from the aircraft engine and APU models used, are taken for simplicity. In reality, charges are determined upon so-called equivalent NO_x emissions which consider several pollutants emitted by the engines during a standardized landing-takeoff cycle on the basis of their certified values (see for example [34]).

Furthermore, the effect of payload reduction needs to be taken into account. To quantify the revenue loss due to reduced payload, the average passenger yield achieved by the European airlines was taken. This quantity is defined as the revenue per passenger

Table 7.7: **Assumptions for assessment of influence of ETS on operating costs**

Parameter	Value
Jet A fuel cost	2.20 US$/gallon
Pushback tractor cost	180.00 US$/hour
Pushback tractor lease time for conventional aircraft	20 minutes
Engine warm-up/cool-down time on ETS-equipped aircraft	3 minutes
Per-engine base hourly maintenance cost rate	100.00 US$/hour
APU hourly maintenance cost rate	35.00 US$/hour
NO_x-related airport charge	3.50 US$/kg

transported and per kilometer flown; it amounted to 0.114 US$/ (passenger · km) in the year 2013 [15]. Considering the IATA standard passenger weight of 100 kg including baggage [15], the payload yield of 0.00114 US$/ (kg · km) was used for this assessment. Whether payload has to be reduced, and to what extent, strictly depends on the characteristics of each mission. In the following, the two extreme cases are compared: that no payload reduction is necessary, and that a payload reduction of the same amount of the ETS weight is needed.

Finally, due to the lack of data and because the level of detail needed for a reliable analysis would fall outside the scope of this thesis, the following cost items were neglected in this assessment: brake maintenance costs, ETS maintenance costs, and any economic impact of modified ground operations due to the use of ETS. Table 7.7 contains the values of the cost items on which this assessment is based.

Case without payload reduction

In the first analysis, the assumption is made that the additional ETS weight complies with the weight limits of the aircraft and does not induce any payload reduction. Figure 7.16 illustrates the operating cost balances for the five missions considered. It can be seen that adopting an ETS is beneficial in reducing operating costs in most cases. While the benefit decreases in general with larger ETS sizes due to the additional mass and the corresponding block fuel increase, the low performances of too small ETS sizes also negatively affect cost. This phenomenon is similar to what was also observed for the assessment of fuel benefits (see Section 7.2.5). However, large and heavy ETS are no longer convenient in the longest mission. The descending trend of the cost balance over the mission length suggests that ETS would not be beneficial for flights even longer than those considered in this assessment.

A breakdown of the operating cost changes is shown in Figure 7.17 for the 783 NM mission with ETS size $\lambda_A = 1$. The histogram contains the cost item variations between ETS-equipped and conventional aircraft. The largest factors in determining the cost balance are the fuel and the tow tractor rent. The engine maintenance cost

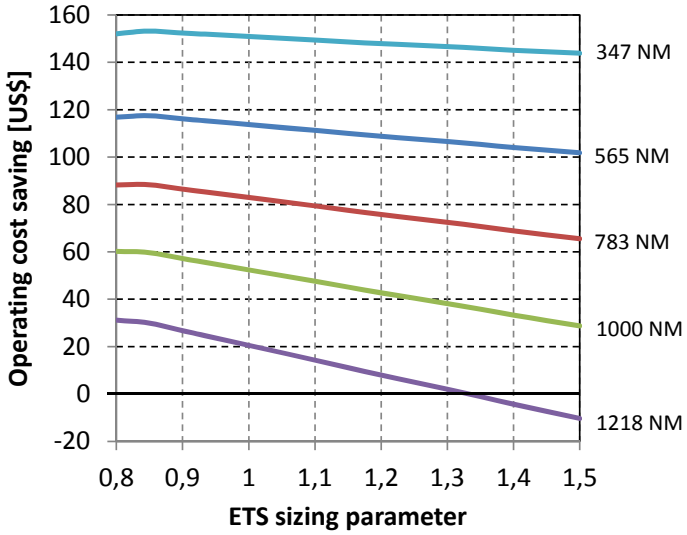

Figure 7.16: **Operating cost balance over ETS size for the "short taxi with stops" mission scenario with five different flight lengths**

advantage resulting from the reduced running hours also has a relevant impact. To this regard, it needs to be noted that the engine wear at idle might be lower than in flight, hence the idle running time might impact on the maintenance cost less than was assumed in this analysis by taking a constant base maintenance rate.

Case with maximum payload reduction

The analysis was repeated, this time by assuming that the conventional aircraft was already at its weight limits; thus the added ETS weight resulted in a payload reduction of the same value. Note that in this case, because the gross aircraft weight remains the same, no additional block fuel is needed for the ETS-equipped aircraft. As is clear from Figure 7.18, all five missions considered suffered an unacceptably large increase in operating costs.

Finally, a comparison between economic and energetic assessment (fuel consumption balance) is given in Figure 7.19 for the whole family of ETS considered in the two cases with and without payload reduction. The energetic break-even is taken over from Figure 7.6b pertaining to the flight mission considered; the economic break-even curves were determined by interpolating and extrapolating the data underlying figures 7.16 and 7.18. The break-even curves mean that flight lengths below the curves are beneficial in the sense of the respective criterion for a given ETS size. It can be seen from the plot that in the case without payload reduction, the economic break-even lies way above the energetic one. In other words, flight lengths contained in the area

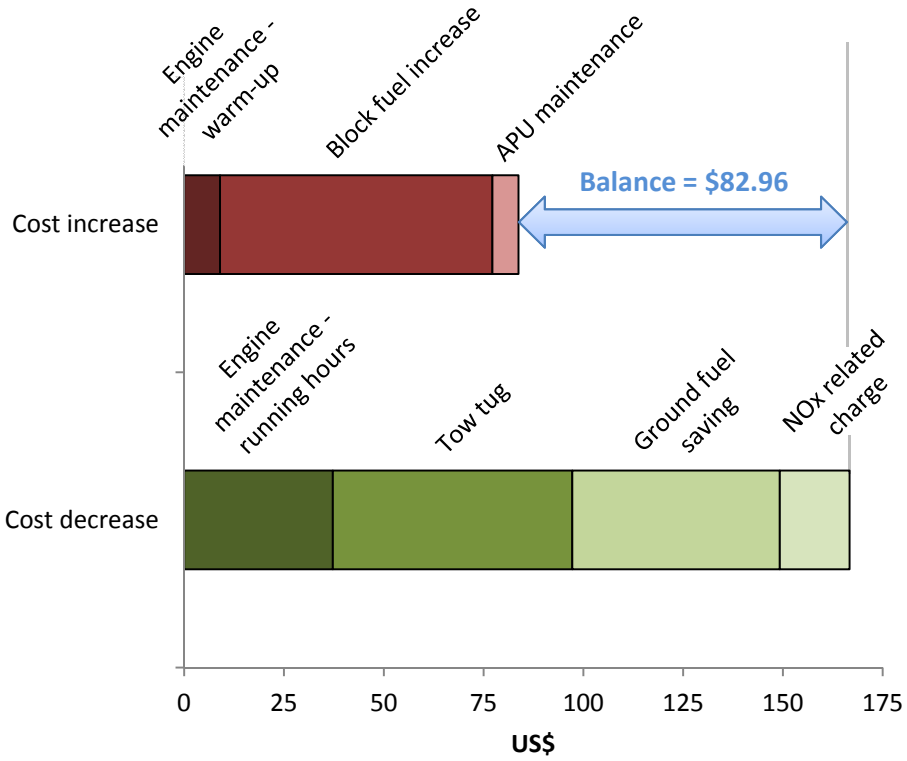

Figure 7.17: **Operating cost variations with respect to conventional aircraft for an ETS-equipped aircraft in the "short taxi with stops" mission scenario with 783 NM flight length, ETS sizing parameter $\lambda_A = 1$**

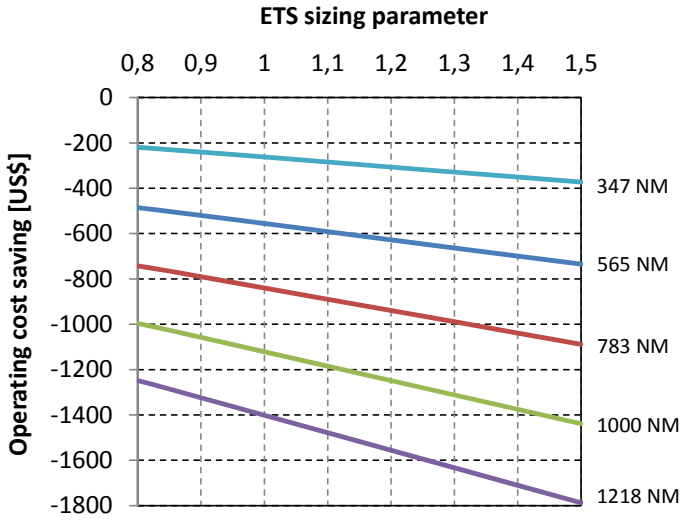

Figure 7.18: **Operating cost balance over ETS size for the "short taxi with stops" mission scenario with five different flight lengths and maximum payload reduction due to the addition of ETS. A negative cost saving means all missions suffer increased operating costs with any ETS size.**

between this curve and the energetic break-even curve are still economically advantageous even though they result in a overall fuel consumption increase. This result shows that — provided the payload capacity is not affected — green taxi systems can be an interesting solution for airlines and stakeholders beyond the environmental aspects. However in the case of maximum payload reduction, the adoption of ETS is economically beneficial only for extremely short flights, which are unrealistic for this aircraft type. This suggests that if payload needs to be reduced as a result of adding ETS, its economic viability will be compromised. Such a large influence on the business results makes a careful case-by-case analysis necessary when considering the adoption of green taxi technology.

7.5 Demonstration of Methodology for Real Flight Missions

The ETS assessment methodology discussed in this thesis has been applied to two real-world flights in order to better show its potential with real flight missions. The first flight chosen for analysis is the Lufthansa LH908 from Frankfurt to London Heathrow, representing a short-range flight with a length of approximately 450 NM (833 km) and a duration of approximately 90 minutes. The second flight is the TuiFly X32259

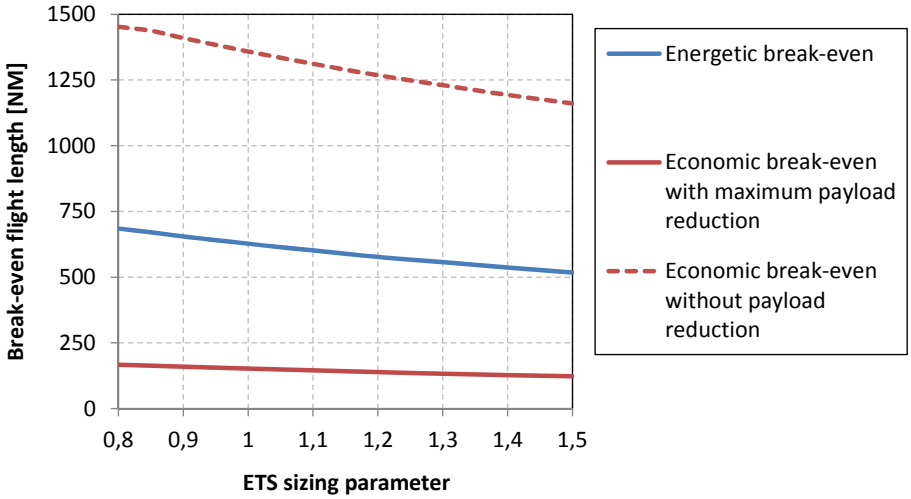

Figure 7.19: **Comparison of break-even flight lengths resulting from energetic criterion (fuel consumption balance) and from economic criterion (cost balance) with maximum payload reduction as well as without payload reduction**

from Las Palmas to Frankfurt, a long-range flight with a length of approximately 2,100 NM (3,889 km) and a duration of approximately 4 hours and 15 minutes. The mission profiles for both flights were taken from the flight data recorded by the Automatic Dependent Surveillance – Broadcast system (ADS-B) [52] on November 20th, 2015. Because tracking data during the taxi phases were only available at the Frankfurt airport, the taxi trajectories at Heathrow and Las Palmas derive from own assumptions based on real traffic patterns at those airports. Also, the ground speed in the X32259 flight data contained too high values, partially in excess of Mach 0.95, which is above the maximum cruise speed for an A320. The reasons for this may be the influence of wind — for which no data were available in order to subtract this effect — or errors in the measurement data. The speed was therefore limited to the optimum cruising speed of Mach 0.78 wherever required.

Four configurations were compared for each flight: conventional aircraft, and three ETS-equipped aircraft with sizing parameters λ_A = 0.8, 1 and 1.3 respectively. The simulations comprised the following phases:

- taxi-out and taxi-in. Optimal taxi profiles were generated first with the optimal ground path following method, using the fuel minimizing cost function without setting any thermal or time constraints. Afterwards, simulations of the taxi profiles were carried out with the integrated aircraft model subject to the assumptions described in Section 7.2.4;
- complete flight from start to landing. The trajectory described by the recorded

data was tracked with the generic cascaded PID controller already used in Section 7.2.2. The fuel quantity needed for each mission and for each configuration was determined iteratively as described in Section 7.2.2.

The taxi and flight profiles are displayed in figures 7.20 and 7.22 for flight LH908, and in figures 7.21 and 7.23 for flight X32259.

Both the energetic balance (fuel saving) and the economic balance were assessed for the three configurations. The former is shown in Table 7.8. In both flights, the ETS meets the expectations in that the fuel consumption is reduced in the ground phases with respect to conventional aircraft. The larger the ETS, the better the efficiency becomes in taxi out. This trend is not as clear for taxi in, in which the figures are very similar between the different ETS sizes. A possible reason for this discrepancy could be that the higher performance of the larger systems has a larger influence on taxi out, in which the aircraft is loaded with block fuel. Modeling approximations resulting in different behaviors of the tracking controller between the scenarios may also not be excluded. Note that taxi out with the smallest ETS on the long flight resulted in overheating; the main engines were started up in advance to carry on the taxi conventionally (method 1 described in Section 7.3).

Conversely, the weight of the ETS increases the fuel consumption in flight proportionally with the ETS size. While the balance over the whole mission is advantageous for flight LH908 with fuel savings in the range of 1 to 2%, the flight X32259 experiences an overall worsened efficiency due to the much longer flight phase, with fuel consumption increases in the range of approximately 0.9 to 1.6%.

The economic assessment in Table 7.9, which used the same assumptions listed in Section 7.4.2, was performed next. Assuming that the payload does not need to be reduced, it is interesting to note that for LH908, operating cost reductions arise in the vicinity of ca. 140 US$ per flight due to the adoption of the ETS; moreover, the economic balance becomes advantageous for flight X32259 with the small and the intermediate ETS, whereas the larger ETS results in a minor operating cost rise. It can be noted for both the economic and the energetic assessment that while passing from λ_A = 1.3 to 1 causes a significant improvement, passing from λ_A = 1 to 0.8 only results in a marginal additional benefit.

However, ETS is no longer economically convenient if payload needs to be reduced to accommodate the ETS into the aircraft. The balance in this case is shown in Table 7.10 using a payload yield of 0.00114 US$/ (kg · km) (see Section 7.4.2) and reminding that the baseline ETS (with $\lambda_A = 1$) used in this work weighs 600 kg (see Table 4.6). It should also be noted that the mission block fuel remains unchanged in all four cases since the total mass at start is constant. It is apparent that the resulting large revenue losses cannot be compensated by any improvement of economic efficiency that may realistically be achieved by adopting ETS. The economic viability of this technology is therefore strictly dependent on the question whether the additional weight can be installed onto the aircraft without affecting the payload capacity.

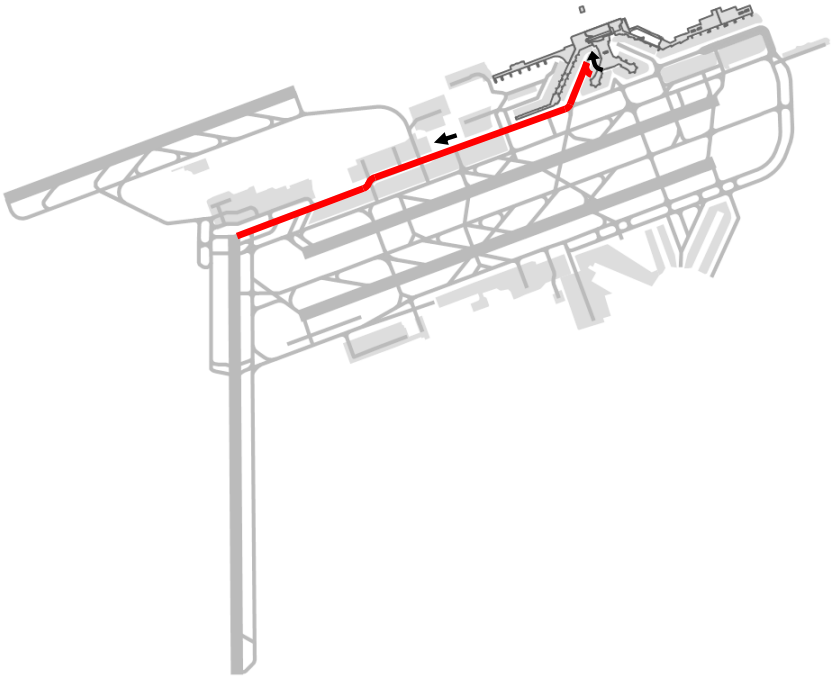

(a) **Taxi out at Frankfurt (map data © OpenStreetMap contributors)**

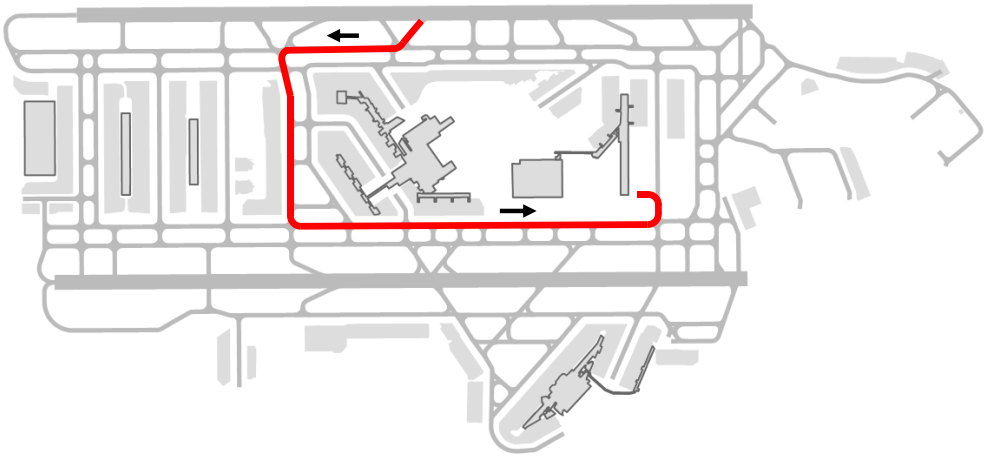

(b) **Taxi in at London Heathrow (map data © OpenStreetMap contributors)**

Figure 7.20: **Taxi routes for flight LH908**

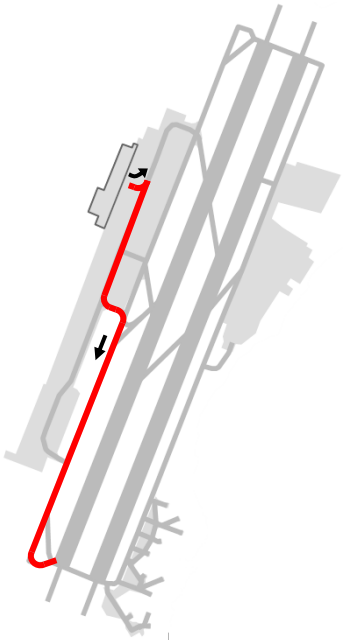

(a) **Taxi out at Las Palmas (map data © OpenStreetMap contributors)**

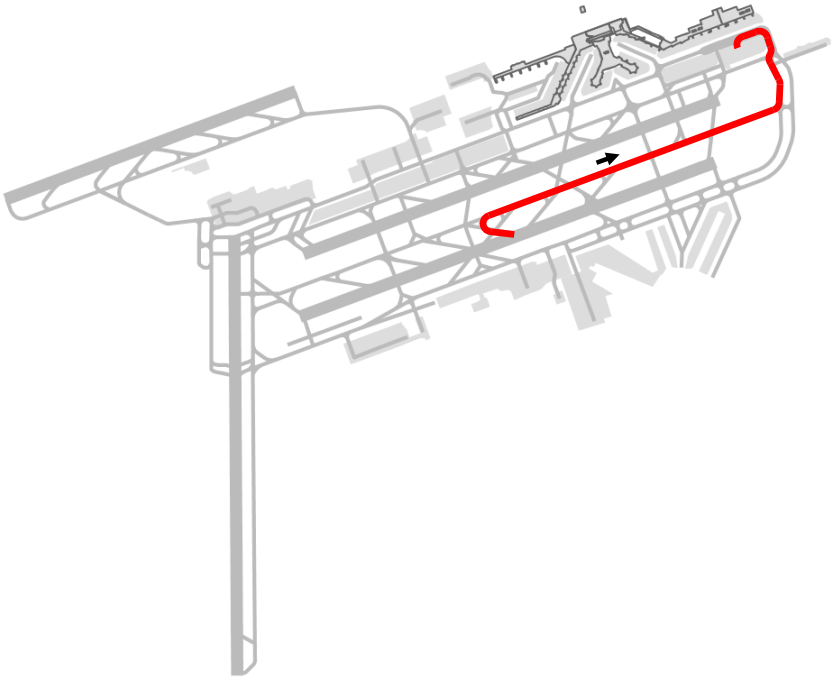

(b) **Taxi in at Frankfurt (map data © OpenStreetMap contributors)**

Figure 7.21: **Taxi routes for flight X32259**

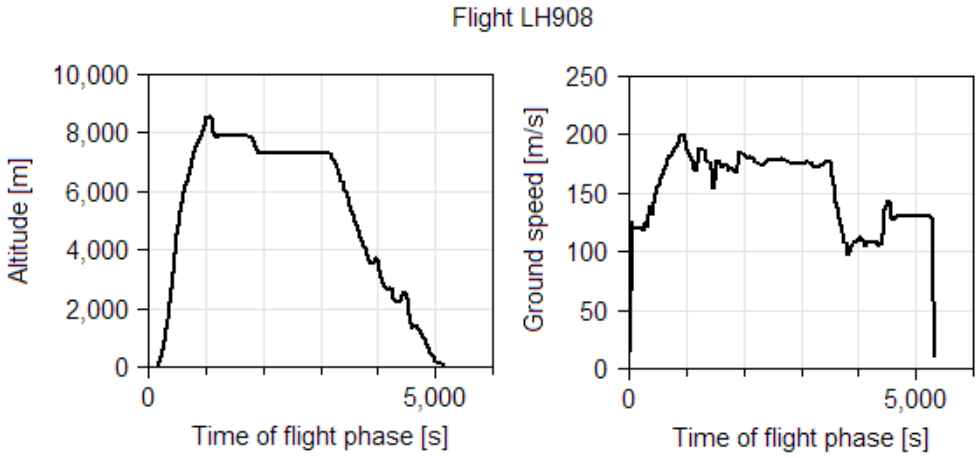

Figure 7.22: **LH908 flight profile**

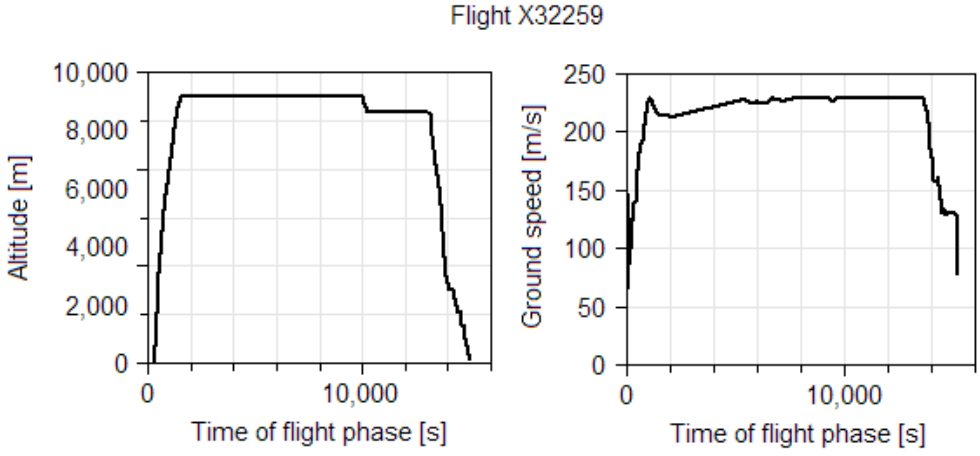

Figure 7.23: **X32259 flight profile**

Table 7.8: **Energetic assessment for real flights with ETS**

Flight no.	Configuration	Fuel consumption [kg]			Difference with conventional
		Taxi out	Flight	Taxi In	
LH 908	conventional	92.0	3,686.1	118.1	
	ETS, $\lambda_A = 0.8$	48.5	3,730.0	48.0	-1.79%
	ETS, $\lambda_A = 1$	47.8	3,737.0	48.1	-1.63%
	ETS, $\lambda_A = 1.3$	46.9	3,750.0	48.5	-1.30%
X3 2259	conventional	79.6	14,038	122.5	
	ETS, $\lambda_A = 0.8$	77.5*	14,242	54.1	+0.91%
	ETS, $\lambda_A = 1$	52.0	14,294	49.9	+1.09%
	ETS, $\lambda_A = 1.3$	49.7	14,372	49.9	+1.63%

* Overheating was avoided by starting the main engines earlier than planned when the ETS temperature limit was reached (method 1 described in Section 7.3)

Table 7.9: **Economic assessment for real flights with ETS without need for payload reduction. All figures, expressed in US$, are differences with the respective conventional flight**

Flight #	Configuration	Fuel	NO_x fee	Maintenance		Tug	Balance
				APU	Engines		
LH 908	ETS, $\lambda_A = 0.8$	-32.6	-15.2	+7.4	-47.1	-60	-147.5
	ETS, $\lambda_A = 1$	-29.6	-15.2	+7.4	-47.1	-60	-144.6
	ETS, $\lambda_A = 1.3$	-23.8	-15.1	+7.3	-47.1	-60	-138.7
X3 2259	ETS, $\lambda_A = 0.8$	+60.5	-9.6	+6.6	-23.9	-60	-26.3
	ETS, $\lambda_A = 1$	+72.9	-12.1	+6.5	-23.9	-60	-16.6
	ETS, $\lambda_A = 1.3$	+108.3	-12.7	+6.5	-23.9	-60	+18.2

Table 7.10: **Economic assessment for real flights with ETS with maximum payload reduction. All figures, expressed in US$, are differences with the respective conventional flight**

Flight #	Configuration	Payload reduction	NO_x fee	Maintenance		Tug	Balance
				APU	Engines		
LH 908	ETS, $\lambda_A = 0.8$	+455.8	-15.2	+7.4	-47.1	-60	+340.9
	ETS, $\lambda_A = 1$	+569.8	-15.2	+7.4	-47.1	-60	+454.9
	ETS, $\lambda_A = 1.3$	+740.7	-15.1	+7.3	-47.1	-60	+625.8
X3 2259	ETS, $\lambda_A = 0.8$	+2,128.1	-9.6	+6.6	-23.9	-60	+2,041.2
	ETS, $\lambda_A = 1$	+2,660.1	-12.1	+6.5	-23.9	-60	+2,570.6
	ETS, $\lambda_A = 1.3$	+3,458.1	-12.7	+6.5	-23.9	-60	+3,367.9

8 Conclusion

The need for improved efficiency and reduced environmental impact of ground operations has recently been recognized and addressed in aeronautic research and development. Particularly, electric taxi operation is being proposed and developed as a means to decrease overall fuel consumption as well as emissions and noise generation in the airport area. However, the question whether this technology causes clear benefits at a global mission level cannot be answered with certainty without considering each specific case. A number of conflicting factors need to be considered already in the early design phase of electric taxi systems as they impact very differently on the overall results of adopting this technology.

This thesis focuses on the issues of design and global-level assessment of Electric Taxi Systems by making methodological contributions to the state of the art. Following the current trend for model-based methods in the conceptual design of aircraft architecture and subsystems, a contribution was made by proposing a **model-based approach for design and assessment of aircraft systems** and applying it as an example to an Electric Taxi System (ETS) in a generic narrow-body commercial aircraft in a number of scenarios. Design based on integrated local and global levels can be superior to conventional design of local systems driven by simple global performance metrics (e.g. *trade factors* [73]) in that the mutual influences between the aircraft, the systems and the operating conditions can be taken into account in the early system design phase. This quickens the design process, improves its efficiency, and ultimately simplifies the task of achieving a globally optimal design. The central element of the model-based design method is represented by an object-oriented, dynamic aircraft model capable of simulating whole missions (Chapter 3). This model was then expanded by integrating a scalable model of ETS (Chapter 4) based on a previously assumed system architecture. Also, a guidance system was modeled (Chapter 6) for the tracking of predefined ground trajectories. The entire modeling activity was based on the Modelica object-oriented modeling language, which is particularly suitable for physical modeling of systems and phenomena and for realizing libraries of modular components. Modelica thus offers the capabilities for developing the aircraft model and the system models separately, and then perform dynamic simulation on the joint global aircraft system after linking the models through appropriate interfaces.

A key contribution was made by developing a **convex optimization algorithm for taxi path following** (Chapter 5). The motivation for this development derives from the fact that an optimal path following profile exists for each given system architecture and variant; a solid performance comparison of different system variants is only

possible if each of them can be operated according to its own optimal profile. By using specific solvers, convex optimization allows to find globally optimal solutions quickly — although they will represent approximate solutions of the real problem due to the simplifications adopted in the convex description of the dynamic system and the problem constraints. The optimization algorithm can take aspects into account such as torque and power limitations, thermal limitations, as well as *maximum-time* and *minimum-time* constraints setting time requirements for passing given trajectory waypoints.

Various missions and scenarios were simulated (Chapter 7), and their assessment enabled to infer a number of conclusions representing empiric contributions of this work to the topic of ETS design.

In Section 7.5, two real flights, LH908 from Frankfurt to Heathrow (450 NM) and X32259 from Las Palmas to Frankfurt (2,100 NM), were simulated in a conventional configuration and with three different ETS sizes. A fuel consumption benefit was only found in the case of LH908, with the largest savings (-1.79% mission block fuel) for the smallest and lightest ETS; the benefit shrinked to -1.30% for the largest ETS. Flight X32259 suffered a block fuel increase between 0.91 and 1.63%, again correlated to the ETS size and mass. This confirms the intuitive expectation that ETS may be beneficial for relatively shorter flights.

More generally, fuel balance maps for generic flight missions with different flight lengths and ETS sizes were plotted (Figure 7.5 and 7.6) after assessing several simulations. These maps, which are specific for the aircraft type and the simulated mission, are useful for a rapid evaluation of the ETS benefits. The results of the generic mission analysis performed in Section 7.2 showed that in specific situations with long taxi times and short flight legs, the choice of a small ETS does not bring an additional benefit with respect to intermediate ETS sizes, because poor performance on the ground results in longer taxi time and APU running time; the related higher APU fuel consumption is no longer counterbalanced by the lower ETS mass in flight. It is inferred from these results that **a small system — which is lighter, but also less powerful — does not necessarily result in an additional improvement of the benefits deriving from the adoption of electric taxi compared to larger, heavier systems**. The best architecture needs to be chosen after careful analysis of the mission schedule flown with a given aircraft, which is made possible by using the proposed model-based approach. Furthermore, it has to be considered that the reduced performance of a smaller ETS may be critical in difficult conditions (e.g. taxiway slopes, heavy aircraft) and results in higher taxi times, thus increasing the APU running time and fuel consumption as well as potentially impacting airport ground traffic negatively.

Depending on its design, ETS may be subject to thermal issues. Overheating jeopardizes the benefits of electric taxi as the ETS must stop operating earlier during the taxi phase. Smaller, low-torque ETS may be particularly affected by thermal problems because high performance is required for a longer time especially in accelerations and decelerations. Therefore, care should be taken when selecting the system size. Section

7.3 discussed how the impact of thermal aspects on the system performance can be investigated in the proposed model-based approach. In particular, it was shown that optimal taxi profiles subject to energy or time constraints generated with the convex optimization algorithm can help mitigate the overheating risks, albeit reducing the average taxi speed.

Considering other methods of coping with overheating, it was demonstrated that choosing the best method for maximizing the benefits is strictly dependent on the system size and the mission schedule flown by the aircraft. It is concluded that **the physical behavior (e.g. thermal) of the system during a given mission is a key factor as it has an immediate impact on the associated benefit. The optimal system architecture specifically depends on the aircraft and the missions, which must be taken into account in the early design phase.** The model-based approach presented in this work enables to simulate critical missions or mission schedules, assess any potential performance limitations, and produce optimized taxi profiles subject to operational constraints, thus representing an important design tool.

While the economic assessment performed in this work had to neglect a number of operating cost items, the results suggest that **the prevailing interest of airlines for the ETS technology may be an economic one rather than an environmental one**, as electric taxi can be economically viable even in case of increased mission block fuel. However, the installation of ETS must not result in a reduction of payload capacity due to the additional system weight, otherwise the economic balance will be clearly negative. Moreover, even in cases in which ETS is disadvantageous both economically and energetically at mission level, noise and emissions are always reduced on ground. Therefore, stakeholders may nevertheless consider or even mandate the adoption of ETS for environmental and public health reasons even though this translates into additional costs for the airlines. Model-based assessment helps the parties involved in that it allows to quantify benefits and costs precisely by taking into account the specific features of the considered aircraft and missions.

Because the models used are only representative of real types of narrow-body commercial aircraft, the results illustrated in this thesis are meant to identify qualitative trends caused by the adoption of ETS and show the potential of the proposed approach on this and other aircraft systems. The results should not be intended as directly applicable to real aircraft types equipped with ETS. More precise, validated dynamic aircraft models, especially including aerodynamics, engines, and control systems, are needed for specific assessment of a real case. The needed precision deriving from the sensitivity of the results to the aircraft and system parameters requires a level of detail normally regarded as confidential by manufacturers. Also, more detailed ETS models, particularly regarding the thermal behavior, are needed for a well-founded analysis of a real system.

Interesting future developments of the present work can be carried out especially in two directions. On the one hand, better optimization at global level should be pursued. The model-based approach permits the insertion of different systems into a global

aircraft platform; integrated simulation is then possible with the aim of optimizing the system parameters at aircraft level. Moreover, the concurrent operation of systems supplied by the APU can be analyzed. As the APU has a limited amount of power, energy management strategies might be needed to coordinate the power requests of the ETS and other large loads such as the Environmental Control System (ECS). In a further step, the APU itself may be subject to optimized re-design in view of higher power requests and longer running times during electric taxi.

The second field of research is the more efficient management of operational aspects. The impact of electric taxi in present-day airports and in scenarios with mixed conventional and ETS-equipped aircraft needs better understanding. As the performances of ETS may be lower than conventional taxi, the effect on the surrounding traffic as well as on the taxi times — and related metrics such as punctuality — needs to be assessed. By contrast, tasks such as the connection and disconnection of tow tugs would not be necessary with ETS, reducing the risk of delays. Eligible methods for those investigations include fast-time simulation of the ground traffic at airport level [85] and economic approaches such as the Value Operations Methodology [27]. Studies are being carried out on this topic. For example, minimum performances for avoiding unacceptable taxi delays at Amsterdam Schipol were determined using the Value Operations Methodology [66]. Finally, more research on advanced taxi control methods and algorithms may be carried out. In a more distant future, autonomous taxi may be introduced, exploiting interconnections among aircraft on ground to find globally optimal control strategies and reduce the environmental impact in airport areas.

Bibliography

[1] Non-Skid Braking - The Maxaret Automatic Unit: What It Is and What It Does. *Flight*, pages 587–588, 30th Oct 1953.

[2] DLR Airbus A320 ATRA Taxis Using Fuel-Cell-Powered Nose Wheel for the First Time, 6th July, 2011. Retrieved November 2016. URL: `http://www.dlr.de/en/desktopdefault.aspx/tabid-6840/86_read-31408/`.

[3] CVX: Matlab software for disciplined convex programming. Version 2.0 beta, CVX Research, Inc., 2012.

[4] Aircraft APU Emissions at Zurich Airport. Technical report, Unique (Flughafen Zürich AG), January 2005.

[5] Dassaults Systemes' Dymola website, retrieved August 2010 URL: `http://www.3ds.com/products/catia/portfolio/dymola`.

[6] Cleansky Joint Technology Initiative Homepage, Retrieved November 2016. URL: `http://www.cleansky.eu/`.

[7] Wheeltug Homepage, Retrieved November 2016. URL: `http://www.wheeltug.gi/index.php`.

[8] MATLAB Control System Toolbox Release 2012a, The MathWorks, Inc., Natick, Mass., United States, 2012.

[9] MATLAB Release 2012a, The MathWorks, Inc., Natick, Mass., United States, 2012.

[10] S. Ackert. Elements of Aircraft Maintenance Reserve Development. In *IATA Maintenance Cost Conference, Abu Dhabi, United Arab Emirates*, October 20th, 2010.

[11] S. Ackert. Engine Maintenance Concepts for Financiers - Elements of Turbofan Shop Maintenance Costs. *Aircraft Monitor*, September 2011. Second edition.

[12] Airbus. *Airbus A320 Training Simulator Flight Crew Operating Manual - Electrical System*.

[13] Airbus. Taxibot set to usher in a new era of airport taxiing, 15th February, 2012. Retrieved November 2016. URL: `http://www.airbus.com/newsevents/news-events-single/detail/taxibot-set-to-usher-in-a-new-era-of-airport-taxiing/`.

[14] Airbus Customer Services. *Flight Operations Support & Line Assistance: Getting to Grips with Fuel Economy*, July 2004.

[15] Association of European Airlines (AEA). Summary of Traffic and Airline Results, July 2014.

[16] A. Boglietti, A. Cavagnino, and D. Staton. Determination of Critical Parameters in Electrical Machine Thermal Models. *IEEE Transactions on Industry Applications*, 44(4):1150–1159, July-August 2008.

[17] A. Boglietti, A. Cavagnino, D. Staton, M. Shanel, M. Mueller, and C. Mejuto. Evolution and Modern Approaches for Thermal Analysis of Electrical Machines. *IEEE Transactions on Industrial Electronics*, 56(3):871–882, 2009.

[18] S. Boyd and L. Vandenberghe. *Convex Optimization*. Cambridge University Press, 2004. ISBN 978-0-521-83378-3.

[19] R. Braier. TaxiBot Taxiing System. In *IATA Aircraft Taxiing Systems Conference*, Coral Gables, Fla., USA, 3-4 February, 2015.

[20] J. Brombach, T. Schröter, A. Lücken, and D. Schulz. Optimized Cabin Power Supply with a 270 V DC Grid on a Modern Aircraft. In *2011 7th International Conference-Workshop on Compatibility and Power Electronics (CPE), Tallinn, Estonia*, 1-3 June 2011.

[21] CAST/ICAO Common Taxonomy Team. *Phase of Flight Definitions and Usage Notes*, February 2006.

[22] CFM. CFM56 Flight Operations Support, Semptember 10th, 2005.

[23] S. T. Chai and W. H. Mason. Landing Gear Integration in Aircraft Conceptual Design. Technical report, MAD Center, Virginia Tech, Blacksburg, Va., USA, 1996.

[24] J. Chiasson. *Modeling and High Performance Control of Electric Machines*. Wiley-IEEE Press, 2005. ISBN 978-0-471-68449-7.

[25] CleanSky Joint Technology Initiative. TaxiBot, Cleansky "Dispatch Towing Vehicle (DTV)", December 2011. Retrieved May 2012. URL: `http://www.cleansky.eu/content/interview/taxibot-clean-sky-dispatch-towing-vehicle-dtv`.

[26] S. Consortium. SESAR Definition Phase - Deliverable D1 - Air Transport Framework: The Current Situation, July 2006.

[27] R. Curran, T. Abu-Kias, M. Repco, Y. Sprengers, P. van der Zwet, and W. Beelearts. A Value Operations Methodology for Value Driven Design: Medium Range Passenger Airliner Validation. In *48th AIAA Aerospace Sciences Meeting Including the New Horizons Forum and Aerospace Exposition*, Orlando, Fla., USA, 4-7 January 2010.

[28] R. de Castro, M. Tanelli, R. Araujo, and S. Savaresi. Minimum-time Path Following in Highly Redundant Electric Vehicles. In *19th World Congress of the International Federation of Automatic Control*, Cape Town, South Africa, August 24-29, 2014.

[29] I. Deonandan and H. Balakrishnan. Evaluation of Strategies for Reducing Taxi-out Emissions at Airports. In *Proceedings of the AIAA Aviation Technology, Integration, and Operations (ATIO) Conference*, September 2010.

[30] N. Dzikus, J. Fuchte, A. Lau, and V. Gollnick. Potential for Fuel Reduction through Electric Taxiing. In *Proceedings of the 11th AIAA Aviation Technology, Integration, and Operations Conference*, 2011.

[31] EGTS Team. EGTS Taxiing System. In *IATA Aircraft Taxiing Systems Conference*, Coral Gables, Fla., USA, 3-4 February, 2015.

[32] Federal Aviation Administration (FAA). Advisory Circular No. 120-74A - Flight Crew Procedures During Taxi Operations, March 26th, 2013.

[33] Federal Aviation Administration (FAA). Focus on Hotspots - Prevent Runway Incursions, Retrieved November 2016. URL: `https://www.faa.gov/airports/runway_safety/publications/media/Focus%20on%20Hot%20Spots%20Brochure.pdf`.

[34] Fraport AG - Frankfurt Airport. Airport Charges according to Art. 19b Air Traffic Act (LuftVG) - Charges for Central Ground Handling Infrastructure, October 30th, 2014.

[35] P. Fritzson and P. Bunus. Modelica–A General Object-Oriented Language for Continuous and Discrete-Event System Modeling and Simulation. In *Proceedings of the 35th Annual Simulation Symposium*, San Diego, California, April 14-18, 2002.

[36] J. F. Gieras and M. Wing. *Permanent Magnet Motor Technology: Design and Applications*. CRC Press, 2nd edition, 2002. ISBN 0-82474-394-6.

[37] A. Graham. *Managing Airports: an International Perspective*. Butterworth-Heinemann, 2008. ISBN 978-0-7506-8613-6.

[38] M. Grant, S. Boyd, and Y. Ye. Disciplined Convex Programming. In L. Liberti and N. Maculan, editors, *Global Optimization: From Theory to Implementation*, pages 155–210. Springer, 2006.

[39] Honeywell Aerospace GmbH. 131-9(A) APU Acceptance Test Data Sheet, October 2011.

[40] International Civil Aviation Organization (ICAO). *Annex 14 to the Convention on International Civil Aviation - Aerodromes - Volume I: Aerodromes Design and Operations*, fifth edition, July 2009.

[41] International Civil Aviation Organization (ICAO). ICAO Aircraft Engine Emissions Databank, Retrieved 5th January, 2016. URL: `https://easa.europa.eu/document-library/icao-aircraft-engine-emissions-databank`.

[42] T. Kier, M. J. Verveld, and C. W. Burkett. Integrated Flexible Dynamic Loads Models Based on Aerodynamic Influence Coefficients of a 3D Panel Method. In

International Forum on Aeroelasticity and Structural Dynamics, St. Petersburg, Russian Federation, 28 June - 02 July 2015.

[43] R. Krishnan. *Permanent Magnet Synchronous and Brushless DC Motor Drives*. CRC Press, 2009. ISBN 978-1-4200-1423-5.

[44] J. Lienig and H. Brümmer. *Elektronische Gerätetechnik*. Springer, 2014. ISBN 978-3-642-40962-2.

[45] S. Liscouët-Hanke. *A Model-Based Methodology for Integrated Preliminary Sizing and Analysis of Aircraft Power System Architectures*. PhD thesis, Université de Toulouse, 2008.

[46] G. Looye. The New DLR Flight Dynamics Library. In B. Bachmann, editor, *Proceedings of the 6th International Modelica Conference*, volume 1, pages 193–202, Bielefeld, Germany, 2008. The Modelica Association.

[47] G. Looye, M. Thümmel, M. Kurze, M. Otter, and J. Bals. Nonlinear Inverse Models for Control. In *Proceedings of the 4th International Modelica Conference*, pages 267–279, Hamburg, Germany, 7-8 March 2005.

[48] Lufthansa Technik. Joint demonstration of new electric taxi system, 8th December, 2011. Retrieved November 2016. URL: `https://www.lufthansa-technik.com/documents/100446/101447/etaxi_08122011_e.pdf/a4326697-065e-4b92-b833-e8ae1838ddbb`.

[49] Lufthansa Technik. LEOS tests TaxiBot under real conditions, May 2011. Retrieved May 2012. URL: `http://www.lufthansa-technik.com/applications/portal/lhtportal/lhtportal.portal?requestednode=395&_pageLabel=Template7_8&_nfpb=true&webcacheURL=TV_I/Media-Relations-new/Press-Releases/LEOS_TaxiBot_Erprobung_US.xml`.

[50] Z. Mihailovic. Modeling and Control Design of Vsi-Fed Pmsm Drive Systems With Active Load. Master's thesis, Virginia Tech, Blacksburg, Va., USA, June 1998.

[51] I. Moir and A. Seabridge. *Aircraft Systems: Mechanical, electrical, and avionics subsystems integration*. John Wiley & Sons, 3rd edition, 2008. ISBN 978-0-470-05996-8.

[52] A. Mozdzanowska, R. Weibel, E. Lester, and R. J. Hansman. The Dynamics of Air Transportation System Transition. In *7th USA/Europe ATM 2007 R&D Seminar*, Barcelona, Spain, July 2007.

[53] U. of Aachen. Roads2HyCom Hydrogen and Fuel Cell Wiki - Case Study: Aircraft APU, Retrieved November 2016. URL: `http://www.ika.rwth-aachen.de/r2h/index.php/Case_Study:_Aircraft_APU.html`.

[54] M. Otter, H. Elmqvist, and S. E. Mattson. The New Modelica MultiBody Library. In *3rd International Modelica Conference*, 2003.

[55] H. B. Pacejka. *Tyre and Vehicle Dynamics*. Butterworth-Heinemann, second edition, 2006.

[56] M. J. Provost. The More Electric Aero-engine: a general overview from an engine manufacturer. In *International Conference on Power Electronics, Machines and Drives*, 4-7 June, 2002.

[57] R. Rajamani. *Vehicle Dynamics and Control*. Springer, 2006. ISBN 0-387-26396-9.

[58] K. Rajashekara, J. Grieve, and D. Daggett. Hybrid fuel cell power in aircraft. *IEEE Industry Applications Magazine*, 14:54–60, July-August 2008.

[59] T. Raminosoa, T. Hamiti, M. Galea, and C. Gerada. Feasibility and Electromagnetic Design of Direct Drive Wheel Actuator for Green Taxiing. In *IEEE Energy Conversion Congress and Exposition*, 2011.

[60] K. J. Åström and T. Hägglund. *PID Controllers: Theory, Design, and Tuning*. ISA: The Instrumentation, Systems, and Automation Society, 2nd edition, 1995. ISBN 1-55617-516-7.

[61] F. Re. Viability and State of the Art of Environmentally Friendly Aircraft Taxiing Systems. In *2012 Electrical Systems for Aircraft, Railway and Ship Propulsion Conference (ESARS)*, Bologna, Italy, 16-18 October, 2012.

[62] F. Re. An Object-oriented Model for Development and Assessment of Green Taxiing Systems. In *Greener Aviation: Cleansky breakthroughs and worldwide status*, Brussels, Belgium, 12-14 March 2014.

[63] F. Re. A Convex Methodology for Optimal Path Following with Electric Aircraft Taxi Systems Under Performance and Passing Time Constraints. *IEEE Transactions on Control Systems Technology*, submitted for publication, 20th September, 2016.

[64] F. Re and R. de Castro. Energetically Optimal Path Following for Electric Aircraft Taxi Systems Based on Convex Optimization. In *2014 IEEE International Electric Vehicle Conference*, Florence, Italy, 17-19 December 2014.

[65] G. Riebe and L. Corio. Aircraft taxi speed control system and method, Oct. 12 2006. US Patent App. 11/143,183.

[66] P. C. Roling, P. Sillekens, and R. Curran. The Effects of Electric Taxi Systems on Airport Surface Congestion. In *15th AIAA Aviation Technology, Integration, and Operations Conference*, 2010.

[67] Safran. Messier-Bugatti's Green Taxing Solutions for Smarter Ground Operations, July 2010. Retrieved May 2012. URL: `http://www.safranmbd.com/actualites/actu-et-communiques-de-presse/article/messier-bugatti-s-green-taxiing?lang=en`.

[68] M. Schier, F. Rinderknecht, and H. Hellstern. Electric Wheel Hub Motor for Aircraft Application. *International Journal Of Renewable Energy Research*, 1(4):298–305, 2011.

[69] D. Schlabe. *Modellbasierte Entwicklung von Energiemanagement-Methoden für Flugzeug-Energiesysteme*. PhD thesis, Technische Universität Dresden, 2015. Dr. Hut-Verlag, ISBN 978-3-8439-0504-6.

[70] D. Schlabe, M. Sielemann, C. Schallert, D. Zimmer, M. Kuhn, Y. Ji, and J. Bals. Towards a Model-based Energy System Design Process. In *2012 SAE Power Systems Conference*, Phoenix, Ariz., USA, October 30 - November 1, 2012.

[71] G. Schuermann, K. Schäfer, C. Jahn, H. Hoffmann, M. Bauerfeind, E. Fleuti, and B. Rappenglück. The impact of NOx, CO and VOC emissions on the air quality of Zurich airport. *Atmospheric Environment*, 41:103–118, 2007.

[72] R. Seemann, S. Langhans, T. Schilling, and V. Gollnick. Modeling the Life Cycle Cost of Jet Engine Maintenance. In *60. Deutscher Luft- und Raumfahrtkongress (DLRK), Bremen, Germany*, 27-29 September, 2011.

[73] M. Sielemann. *Device-Oriented Modeling and Simulation in Aircraft Energy Systems Design*. PhD thesis, Technische Universität Hamburg-Harburg, 2012. Dr. Hut-Verlag, ISBN 978-3-8439-0504-6.

[74] D. Staton and A. Cavagnino. Convection Heat Transfer and Flow Calculations Suitable for Electric Machines Thermal Models. *IEEE Transactions on Industrial Electronics*, 55(10):3509–3516, October 2008.

[75] S. Stipetic, D. Zarko, and M. Popescu. Scaling Laws for Synchronous Permanent Magnet Machines. In *2015 Tenth International Conference on Ecological Vehicles and Renewable Energies (EVER)*, March 2015.

[76] M. Tari, K. Yoshida, and S. Sekito. A High Voltage Insulating System with Increased Thermal Conductivity for Turbo Generators. In *Coil Winding, Insulation and Electrical Manufacturing Conference*, Berlin 2001.

[77] The Boeing Company. Flight Operations Review: Taxiing with Carbon Brakes, August 1st, 1990.

[78] The Boeing Company. Flight Operations Engineering: Reduced and Derated Thrust, Semptember 2009.

[79] E. Torenbeek. *Advanced Aircraft Design: Conceptual Design, Analysis, and Optimization of Subsonic Civil Airplanes*. John Wiley and Sons, 2013. ISBN 978-1-118-56811-8.

[80] Transport Canada - Air Navigation System Requirements Branch. *Aerodome Standards and Recommend Practices*, 4th edition, March 1993. (revised 03/2005).

[81] R. H. Tutuncu, K. C. Toh, , and M. J. Todd. Solving Semidefinite-quadratic-linear Programs using SDPT3. *Mathematical Programming*, 95(2):189–217, 2003.

[82] U.S. Department of Transportation Research and Innovative Technology Administration. Bureau of Transportation Statistics Special Report - Sitting on the Runway: Current Aircraft Taxi Times Now Exceed Pre-9/11 Experience. Technical report, May 2008.

[83] U.S. Energy Information Administration. Spot Prices: Petroleum & Other Liquids, Retrieved January 5th, 2016. URL: `http://www.eia.gov/dnav/pet/pet_pri_spt_s1_m.htm`.

[84] D. Verscheure, B. Demeulenaere, J. Swevers, J. D. Schutter, and M. Diehl. Time-optimal Path Tracking for Robots: a Convex Optimization Approach. In *IEEE Transactions on Automatic Control*, volume 54, pages 2318–2327, 2009.

[85] R. Wollenheit and T. Mühlhausen. Operational and Environmental Assessment of Electric Taxi Based on Fast-Time Simulation. *Transportation Research Record: Journal of the Transportation Research Board*, (2336):36–42, 2013.

[86] D. Zimmer and M. Otter. Real-time models for wheels and tyres in an object-oriented modelling framework. *Vehicle System Dynamics*, 48(2):189–216, 2010.